PREPRINT UCRL- 79894

CONF-770954--2

Lawrence Livermore Laboratory

DIAGNOSTICS OF INERTIAL CONFINEMENT FUSION EXPERIMENTS

Harlow G. Ahlstrom

August 1977

This Paper was Prepared for Submission to the 11 Conference on Hot Plasma Diagnostics, Kharkov, USSR, September 22-27, 1977.

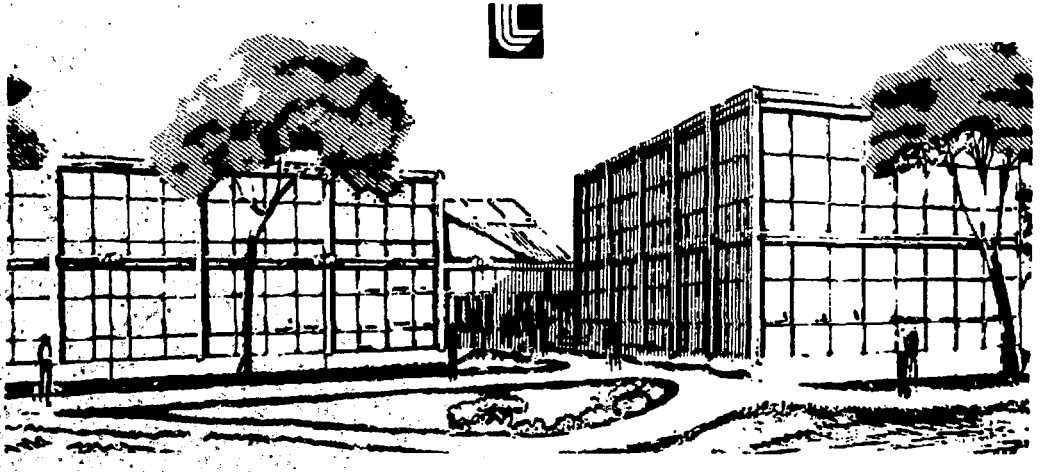

DIAGNOSTICS OF INERTIAL CONFINEMENT FUSION EXPERIMENTS*

Harlow G. Ahlstrom

University of California
Lawrence Livermore Laboratory
Livermore, CA. 94550

ABSTRACT

The requirements of plasma temperature and particle energies are effectively the same for inertial confinement fusion, ICF, and magnetic containment fusion, MCF. The $n\tau$ product must also be similar, however, in ICF we increase the density to achieve efficient fuel burn up. Reactor gain pellets are expected to require densities of up to 10^4 x liquid density of DT. This corresponds to $n \sim 10^{26}$ cm^{-3}. The dimensions of the compressed core are of the order of microns. Thus, the diagnostics problems in ICF is to measure plasmas at $\sim 10^8$ K, n 10^{26} cm^{-3}, on scale lengths of microns with time scales of picoseconds. In this paper we discuss the extensive diagnostics which we have developed to measure the performance of our laser irradiated targets.

*Work performed under the auspices of the U.S. ERDA Contract W-7405-ENG-48

I. INTRODUCTION

Science is advanced both by experiment and theory and the most rapid advances occur when the two are closely coupled together. In Maxwell's famous treatist on electricity and magnetism[1] he points out that the experiments and observations made by Michael Faraday were so complete and well organized that his task was simply to generate the mathematical formalism which summarized his observations. In our Program at Livermore we have a closely coupled system of theory, calculations and experiments. A typical sequence of events is first a statement of the physics objectives, next preliminary code calculations to determine the most appropriate experimental conditions, a determination of the required diagnostics to measure observables in the experiments, target fabrications, execution of the experiments with the laser system, reduction of the experimental data, analysis of the data and comparison with code calculations of the actual experiments performed and finally an analysis of the physics results. A key feature in the sequence is the utilization of a large number of unique diagnostics which are required to make progress in the science of laser fusion.

It is now well established in the inertial confinement fusion community that densities of 1000 to 10,000 x that of liquid density of DT will be required using driver energies of interest to generate efficient burn up of the fusion fuel and net energy production.[2,3,4,5] Input energies of the order of a megajoule will be required and gains of the order of 100 will be necessary for commercial application for inertial confinement fusion. The reactor pellets will be compressed to diameters of the order of 10 microns and will have reaction times of the order of

10 picoseconds. This extreme new region of parameter space in physics places new requirements on the experimentalist to properly diagnose inertial confinement fusion experiments. Listed below in Table I are the range of parameters which must be measured to properly understand experiments in ICF.

In this paper we will discuss our present capabilities in terms of the parameters which can presently be measured. We will also present the general diagnostic configurations of our present system, a six terawatt laser, Argus, and the diagnostic configuration for the system which we are now completing, the 25 terawatt, 20 beam laser, Shiva. Because of the unique state-of-the-art nature of the laser drivers which we use in our experiments we will present a short description of some of the unique diagnostics of the laser systems. The diagnostics of the output of the laser driver are the first crucial step in understanding the results of a given experiment. Since these devices are state-of-the-art and developmental, a few simple measurements are not sufficient to characterize their output and therefore determine the initial conditions for the targets experiments. The second most important diagnostic measurement is to determine the coupling of the laser energy to the pellet which is being irradiated. Part of the laser energy is refracted and scattered by the plasma which it creates, thus, the simple concept of energy balance is vital to the understanding of the experments. In addition, much can be inferred about the laser interaction by measuring the distribution and polarization of the scattered light and also by measuring the distribution of the energy coupled into the target in the form of plasma and photon emission.

The plasma temperatures of interest in inertial confinement fusion range from approximately 100 eV up to the order of 50 keV. Thus, the photon emission will be primarily in the soft x-ray regime. Because

collective processes in the plasma generate very high energy electrons, in addition to the thermal distribution we have a suprathermal x-ray emission from the plasma and thus x-ray emission into even the MeV region of the spectrum is of interest. We have developed a large number of instruments to measure the spectral, spacial and temporal distribution of these x-rays. The reaction products themselves provide very significant data on the performance of the implosion experiments and of the fusion reactions. We will discuss measurements of the fusion yield, and techniques for utilizing the reaction products to determine quantities such as the temperature of the fuel, compression of the fuel and the final density radius product, ρr, of the pusher. In Table II below we list our present capabilities in terms of temporal and spacial resolution and our capability in measuring the distribution of x-rays. We also list our ability to measure density distribution by the use of holographic interferometry. We continue to maintain an aggressive program in the development of new diagnostics to extend our coverage with the goal being complete coverage of the ranges listed in Table I.

II. FACILITIES

The Laser Fusion Program at LLL has concentrated primarily on the neodymium glass laser for the proof of principle and development of laser fusion to the point of scientific feasibility. The first neodymium glass laser was the Long Path Laser. It operated in the multipass configuration, utilizing 16 circular disks in an amplifier head. The disk amplifier was multipassed either 5 or 9 times producing an elliptical output beam. The maximum power cability of this system was

50 gigawatts. The second system developed at Livermore was the Cyclops laser system which was the first system to employ modern concepts in the design of the disk amplifiers and to take into account nonlinear optics which dominate the propagation characteristics of high power systems. Cyclops was built as a prototype system to develop the amplifier hardware for future target irradiation facilities. When amplifiers had been developed with an output aperture of 8.5 cm the Janus two beam target irradiation facility was constructed. This system had a maximum output power capability of 0.4 terawatts. Janus was used to produce the first successful implosion and fusion burn experiments at Livermore.[6,7] It also generated the milestone for inertial confinement fusion of the demonstration of "thermonuclear" burn in a laser compressed pellet.[8] Janus and Cyclops provided the necessary confirmation of laser propagation theories and provided the developmental experience in the fabrication of high power amplifiers. The Argus system shown in Figure 1 is the first large glass laser system which has implemented sequencial spacial filtering to the remove the deleterious and disastrous effects of the small scale self focusing instability.[9] The success of this system is demonstrated in that it first operated as a single beam system in June 1976 and as a two beam system in July 1976 at the design goal of 2 terawatts from the laser. Further improvements in the theory and understanding of high power beam propagation have allowed us to improve the output of the Argus system to 6 terawatts in a 30 picosecond pulse.[10] In a 1 nanosecond gaussian pulse the system is capable of delivering 3 kilojoules. The final amplifiers on the Argus system have an aperture of 20 cm.

The Argus target chamber is shown in Figure 2. The two beams from the system enter the target chamber from opposing directions and are focused onto the target using aspheric f/1 lenses. The quality of the lenses is better than $\lambda/7$. The lenses are positioned remotely under vacuum to within an accuracy of better than 1 um. The Argus target chamber is a very stable optical system which matches the stability of the Argus laser. The overall stability for durations of the order of an hour is better than 10 micro radians. The target chamber is perforated with a large number of ports for the mounting of diagnostics to view the laser driven implosion. Microscopes are used to accurately position each target at the point in space where the two focused beams arrive simultaneously. A large number of diagnostics are also mounted inside the target chamber. Examples of these kinds of diagnostics are shown in Figure 3 which is an interior view of the Cyclops target chamber. Examples of diagnostics which are shown are silicon pin diodes which are used to view the scattered light distribution from the target, x-ray pinhole cameras, plasma calorimeters and x-ray calorimeters. These diagnostics are typically arrayed to view the scattered light or the plasma energy distribution in the plane of polarization and perpendicular to the plane of polarization of the incident light. They are also arrayed at a constant polar angle with sequencial spacing in azimuth to view the complete azimuthal distribution at a given polar angle. As can be seen from these past two figures, there are indeed a large number of diagnostics instruments which are used in the target experiments. Shown in Table III is a listing of the typical diagnostic measurements, the diagnostic instruments and the recording medium for a typical Argus experiment.

In some experimental programs it is relatively easy to repeat a given experiment many times with a rapid repetition rate while maintaining the same input parameters. In laser fusion we have found that it is more appropriate to do a smaller number of experiments with a large number of diagnostics measurements made on each experiments. The present state-of-the-art in target fabrication makes the cost and availability of targets a strong factor in this decision. In addition, making the laser capable of high repetition rate is much more expensive than allowing for experimental frequencies of the order of I to 3 hours. In fact, with the large amount of information which we generate with each experiment more than 3 to 4 experiments per day cannot be properly analyzed. Because of our extensive diagnostics we are implementing the use of small computers wherever possible to reduce the amount of effort required in the reduction of the diagnostic data from the experiments.

The system which we are now constructing is the 20 beam Shiva laser system. It will also utilize 20 cm output amplifiers. The beams are arrayed into bundles of 10 and enter the target chamber from opposing directions. The beams are focused by f/6 aspheric lenses and each beam has a opposing beam direction. An artistic view of a model of the Shiva system is shown in Figure 4. This system is expected to operate with the 14 cm output amplifiers and a output power of 12 to 15 terawatts in December 1977. The 20 cm aperture amplifiers will be added in the Spring of 1978 and full system operation at full system power of 25 to 30 terawatts is expected in the Summer of 1978. A drawing of the Shiva target chamber is shown in Figure 5. Because of the expected use of cryogenic targets in the Shiva system and the concommitant higher vacuum

requirements for the target chamber; we have chosen to mount the focusing lenses and the diagnostics external to the target chamber. The Argus target chamber typically operates in the 10^{-4} to 10^{-5} Torr pressure range whereas the Shiva target chamber will have a capability in the 10^{-6} to 10^{-7} Torr vacuum regime. The spherical portion of the target chamber contains 190 diagnostic ports. The ports are arranged in constant increments of polar and azimuthal angles to allow systematic measurement of target properties which are directional in nature. Because of the large fusion yields which are expected with the use of this system, the neutron diagnostic station is located 100 meters from the target chamber. The first target experiments are planned for December 1977. At this time we will have arrayed a large number of diagnostics on the target chamber. Figure 6 shows a map of the target chamber and the colors of the diagnostic ports indicate the diagnostic instruments which will be in operation.

III. LASER DIAGNOSTICS

In the Argus laser system the control and diagnostics of the laser are all manual and hardwired except for the laser calorimeters which are read using a HP 98-30 computer. The Shiva system is far too complex to operate in the same manner. We have, therefore, adopted a philosophy of microprocessors for local control and data acquisition and minicomputers for centralized control and data acquisition.[11] Through a competitive bid we established a standardized computer system for Shiva. The

microprocessors and the minicomputers are manufactured by Digital Equipment Corporation. The Shiva computer system is shown in Figure 7 The microprocessors provide local control of the complete laser system independent of the four PDP 11/34's and the one PDP 11/70. The PDP 11 34's provide remote and centralized control and data acquisition in the four separate functional areas. The first of these is the power control and the timing of the full firing sequence. The power control system utilizes a 50 volt wire data bus in the control of the power supplies and the firing circuits. This system controls the charging of the capacitor banks and the firing of the laser system. It is isolated from the control room with a 50 kilovolt optical isolator. The second function is the alignment of the complete laser system onto the target. LSI 11 microprocessors are utilized for local control of the oscillator alignment, the chain input pointing, CHIP, the spacial filter pinhole controls, the turning mirror controls, the lens positioning adjustment and the target positioning adjustment. A third block in the laser control and data acquisition is in the beam quality area. In this system we gather data on the output from the oscillator, the energy of the beam as it progresses through the laser chain, the final output of the laser and the energy which is back reflected and forward transmitted through the f/6 focusing lenses. The final block is the target diagnostic area which utilizes a fiber optics CAMAC serial highway and CAMAC modules for the data acquisition.

In Figure 8 we see examples of electrical diagnostics which are recorded in the power control system. The voltage of each section of the capacitor bank is set and recorded using this system. In addition, the

current wave form in each flashlamp circuit is recorded and is available for analysis on each experiments. A typical laser chain diagnostic schematic for Shiva is shown in Figure 9. This system records the energy output of the oscillator and of the rod preamplifier system before it is injected into the multiple splitter array. In addition, we record the laser pulse shape at this point. A 10 picosecond resolution streak camera is used with an electrical data recording system which is a series of 1,024 miniature photodiodes.[12] This device is manufactured by Reticon Corporation. Energy measurements are made at six points along each one of the twenty laser chains of amplifiers. At four stations in each chain a small amount of laser energy is scattered from the output polarizer in the polarizer Faraday rotator or Pockels' cell packages. This energy is focused with a Fresnel lens onto an integrating photo diode. Integrating photodiodes also monitor the laser energy at the CHIP beam splitters and at the output of the $\beta - \gamma$ spatial filters. Thus the development of the laser energy in the laser amplifier chain ca. be monitored and provides information about the quality of the laser amplifiers in a particular chain.

At the output of the laser we take 2% of the output energy through the final turning mirror and direct it to a diagnostic package which is called the incident beam diagnostics or IBD. A schematic of this essential diagnostic package is shown in Figure 10. Diffraction limited optics are used in this package to provide foci which are equivalent to the target lens focus and an IR TV camera monitors the quality of the incident cw alignment laser beam. It is also used to observe the position of the beam in the vacuum spacial filters with respect to the

pinholes and provide observation for proper alignment. We also utilize two laser calorimeters, one observes all the laser energy the other is focused through a pinhole to eliminate any filamentation and observe only the laser energy which is incident on the laser target. Also included is a fast photo diode for temporal measurements and a multiple array camera which provides a series of images of varying distances from the best focus.

A beam is also provided which can be directed to an output streak camera on selected beams. There will be at least two output streak cameras to monitor the temporal distribution of the laser intensity on the target. The Livermore developed streak camera which is utilized for these measurements is shown in Figure 11. Two of these cameras are in current use with the Janus laser system, four of them are in use on Argus and at least five will be utilized simultaneously in the Shiva system. The use of these cameras is essential to determine the temporal and spacial distribution of the laser energy and of the subnanosecond output structure. Typical target experiments have pulses from 30 picoseconds to several nanoseconds. It is not sufficient to measure the laser temporal behavior at the input because of saturation effects and small scale self focusing effects in the propagation of the laser beam through the amplifier chain. Shown in Figure 12 is an example of typical data which is obtained when using the Argus incident beam diagnostic package. This system is identical in concept to the Shiva IBD except that it produces a near field image of the output beam as well. By using an etalon in front of the streak camera, images displaced a known spacing in time are produced and thus provide a self calibration of the streak speed. The film calibration is obtained by exposing the film with a step wedge.

The multiple array camera produces equivalent plane profile energy distributions and these images are self calibrating since the vertical columns of images have known intensity ratios. The multiple array camera images and the streak camera images are computer processed[13] to produce output information shown in Figure 13. One of the images from the multiple array camera is set to correspond to the equivalent target plane in the target chamber. This data is reduced to energy density and then typically is presented as an equivalent axisymmetric distribution. The data is presented in this way for comparison with LASNEX calculations since LASNEX is an axisymmetric two dimensional code. The streak record is also computer processed to produce the spatially averaged power distribution. As shown in Figure 13 the FWHM of this particular pulse was 39 picoseconds. The structure near the peak intensity of the pulse is due to the small scale self focusing produced in the propagation of the laser pulse through the amplifier chain.

The return beam diagnostics or RBD are coupled to the automatic focusing system which is called the PFC module, Shown in Figure 14. The PFC module automatically focuses all 20 beams onto a spherical surrogate target and provides a known reference point of each of the foci with respect to the surrogate target. The lenses are then driven to their desired position with respect to the target to produce the desired target illumination. This system views the target through the final turning mirror. Thus, the beam returning from the target or forwarded transmitted from one of the other beams is collected and diagnosed with the RBD package. Contained in the RBD are a 2.5 cm laser calorimeter to

measure the energy coming back through the focusing lens and a multiple image camera which displays the distribution of the laser energy reflected by the target. A diagnostic beam is also directed to a streak camera for selected modules.

An example of one of our laser calorimeters is shown in Figure 15. These calorimeters are calibrated insitu in conjunction with a full beam calorimeter. These calorimeters utilize BG 18 glass as a volume absorber and also feature a second balanced sensing element as a reference. They also contain electric heaters to provide a known amount of heat input to the system for insitu calibration checks on a regular basis.

IV. ABSORPTION AND SCATTERING OF LASER AND PLASMA ENERGY

The first most critical measurement of the performance of a laser fusion target is the amount of the incident laser energy which is absorbed by the target and converted into plasma energy to drive the implosion. It is relatively straightforward to measure the energy from the laser using incident beam calorimeters and it is also relatively straightforward to use the same type of calorimetry to measure the 1.06 m light which is reflected back through the focusing lens. The difficult problem is to accurately measure the remainder of the scattered and refracted laser energy. One can sample a number of points in space with various elements to determine the scattered and refracted light, however, since the distribution may have lobes or nonuniformities, it is difficult to utilize a sufficiently large number of discrete diagnostic points to arrive at the total scattered light number . To solve this problem we have developed what we call the box calorimeter which is

sensitive only to the 1.06 μm light. The calorimeter completely encloses the laser fusion target except for holes allowing the entrance of the focusing laser beams and a small hole to allow the target to be positioned inside the box. A version of this instrument used with f/1 lenses is shown in Figure 16. Figure 17 shows the details of the construction of this calorimeter. An absorbing element, BG 18 glass, is backed with a copper plate to smooth the temperature distribution and then the temperature rise is measured with thermo electric modules. To prevent the plasma and the x-ray energy from being absorbed by the BG 18 glass we shield the absorber with pyrex glass which is transparent to the 1.06 μm light. A very small fraction of the scattered or refracted laser light can escape by the edge of the BG 18 glass and miss the f/1 focusing lens; however, this represents only a few percent of the total solid angle surrounding the target. When an accurate measurement of the total absorbed energy is required the box calorimeter is used.

For routine operation where we have previously established the absorption characteristics of the target, we utilize a number of discrete sampling points in the target chamber to determine the light scattered outside the cones of the focusing lens. The instruments which we use for these measurements are an active silicon pin diode with a 1.06 μm bandpass filter. The diode package shown in Figure 18 also includes an x-ray absorbing glass to reduce the signal collected by the silicon pin diode due to the high energy x-rays emitted from the target. This is a convenient device to measure the scattered light distribution since the output is integrated and a single word of information is then collected

by our data acquisition computer for each discrete spatial sampling point. However, in some cases the x-ray background is sufficiently large that the corrections are unexceptable. For these cases we have utilized miniature 1.06 μm calorimeters. These are very similar to our laser calorimeters. An example of one of these calorimeters and the instrument housing is shown in Figure 19. The signal in these devices, due to high energy x-rays, is negligble and therefore represents an accurate measurement of the scattered light in a background of high energy x-rays. The disadvantage is that one must measure the time distribution of the voltage from the calorimeter and then extract the energy from the wave form thus requiring a more complex data acquisition module.

The majority of the absorbed laser energy is converted into ions and into thermal x-rays. We have developed another version of our calorimeters to measure the plasma energy distribution. The use of these devices is shown in Figure 20. Here we utilize two balanced recording regions, one which sees the plasma energy and the scattered laser energy, the other which sees only the scattered laser energy. The difference between the signals from these two sensing elements is then the plasma energy for that region of solid angle from the target. These devices have been used to measure the angular distribution of the plasma energy and with this information we are also able to extrapolate the fraction of the laser energy which is converted into plasma energy. In some cases it is also of interest to measure separately the distribution of the x-ray energy from the laser target. For this purpose we have utilized x-ray calorimeters developed by Lockheed Missile and Space Corporation. One of these calorimeter assemblies is shown in Figure 21. The absorber is a

tantalum disk which has been overcoated with 1000 Å of gold to reduce its sensitivity of scattered light. A magnet at the front of the tungsten barrel shield sweeps electrons and ions away from the sensitive element. In addition, in many cases, a carbon filter is used in front of the tantalum gold absorbing surface to cut out the effect of uv and very soft x-rays. The use of these devices then allows us to determine the fraction of the laser energy absorbed by the target and also to make measurements of the distribution of scattered light, the plasma energy distribution and the x-ray energy distribution in space.

V. PLASMA PHOTON EMISSION

Because the temperatures of interest for laser fusion range from 100 eV to of the order of 50 keV the primary photon emission from the plasma will be in the soft to hard x-ray regime. We have thus developed a wide range of instruments to provide us with spectral information on the x-ray, spacial distribution and temporal distribution. The ideal situation, of course, would be to obtain all three of these distributions simultaneously. In most cases it is only possible to obtain one of these distributions with a given instrument. The first example is the broadband spectral distribution from the target. Here, because of the short duration of our laser pulses, in most cases, we have not been able to time resolve the broadband spectrum. The technique used to obtain the broadband spectrum is to utilize K-edge filters in cojunction with the spectral response of the recording medium to provide reasonably well defined energy channels which thereby define the broadband spectrum. This technique is illustrated in Figure 22 where we show the use of

silicon pin diodes and fluor photo multipliers as the detection instruments. The K-edge filter together with a decreasing spectral response of the detector and a falling spectrum with increasing energy allow one to define reasonable response functions for the channels in the spectrograph. These data are recorded as time integrated numbers and collected by our computer data acquisition system, since the temporal response of the detectors is of the order of nanoseconds and most of our experiments have been done with subnanosecond pulses. Higher resolution spectral data can be obtained by utilizing crystals to disperse the spectrum. An instrument which is being used in the Argus experiments is shown in Figure 23. Here we utilize three separate crystals to obtain a broadrange of coverage of energy with the crystal spectrographs. A large variety of crystals have been used for x-ray spectroscopy. In Figure 24 we summarize the x-ray parameters of those with which we are familiar. In general the recording medium has been film, however, we have also implemented a windowless reticon array as the recording device. The response of the reticon array to x-rays is approximately the same as that of Kodak type M film.[16]

An example of a time integrated x-ray spectrum from a glass microshell exploding pusher target is shown in Figure 25. Data from four separate instruments has been recorded here and shows that we can resolve the x-ray spectrum from 200 eV out to 100 keV. The crystal spectragraphs resolve the oxygen lines in the subkilovolt and the silicon and calcium lines in the above 1 keV regime. The time integrated line emission from the silicon in a glass microshell is shown in Figure 26. When data like this can be both temporally and spacially resolved, it will provide

significant information on the temperature and density distribution in the laser fusion pellets. Figure 27 shows another composite x-ray spectrum taken with four separate instruments. The use of the different instruments is necessary to obtain the desired spectral resolution and coverage. In Figure 28 we shown an example of where we have spacially isolated a spectral line in the fusion fuel and thus can use it to determine density of the compressed fuel. In this case neon as well as deuterium tritium gas was difused into the glass microshell target. The neon reaches its maximum emission rate at the time of peak compression. The Stark broadening of the line is then a measure of the density of the fuel at the time of peak compression and heating. A series of these experiments have been done and provided data on the line width of the hydrogen like Ne^{+9} 1s-2p transition. The densities achieved were not as high as desired because of the performance of the laser and therefore the Stark broadening was not as significant as was desired. However, we have shown that one can implement a spectragraph with sufficient resolution to resolve the Stark broadening and we have also demonstrated that the high Z lines from an additive in the fuel can be resolved to determine fuel density.

We have utilized four different techniques to image the x-rays from our laser fusion experiments thus determining the spacial distribution of the x-ray emission. The most best known of these is the pinhole imaging. It is the simplest of the four approaches and requires the least amount of interpretation and calibration. The second technique which we will discuss in this section is the use of grazing incidence reflection of the soft x-rays from polished surfaces to form an image.

The first realization of this approach is our simple four channel x-ray microscope which is shown conceptually in Figure 29. In this case we use two crossed cylindrical mirrors, each of which forms a line image from the emission of the x-rays. The x-rays which reflect from the first mirror and also reflect from the second mirror then produce a real image of the laser fusion x-ray emission. Typically we use this type of microscope in a four channel configuration.[17] The concept is that by using different material for the reflectors in each one of the channels and different K-edge filters we are able to obtain four reasonably well defined x-ray spectral channels. Therefore each instrument provides four x-ray images with different energy spectral bands. Figure 30 shows the reflection efficiency of four of the mirror materials we have used in our experiments for angles which are also typical of microscopes utilized in Argus experiments. The important feature is that there is a sharp high energy cut off as a function of photon energy which in conjunction with a K-edge filter produces the desired spectral channels as shown in Figure 31. The response functions shown here have been obtained using an x-ray calibration facility and thus represent the real response and not the calculated response of the channels of the simple microscope.

One of the disadvantages of the x-ray microscope as compared to the pinhole camera is that greater care must be exercised in the pointing and focusing of the system. However, one of the major advantages is that good resolution of the order of three microns can be obtained with large object distances of the order of 30 cm whereas for pinhole cameras typically the pinhole will be 1 to 2 cm from the target and produce a resolution greater than 5 μm. For high energy laser fusion experiments

these small object distances results in the destruction of the pinhole and filter material on each shot. For very high laser powers one may also have the problem of ionization and closing of the pinhole during the target experiments. Our typical mounting, focusing and alignment fixture for our x-ray microscopes is shown in Figure 32. Figure 33 shows typical data from two channels of the simple microscope for two separate experiments. The Janus experiment at 0.4 TW shows considerable structure in the heating and implosion of the glass microshell. The Argus experiment at 2 TW shows that the higher target specific energy produced a more uniform heating of the glass shell and a more spherical implosion.

The simple four channel x-ray microscopes utilizing cylindrical reflectors has provided very useful data in time integrated images. Its two drawbacks are a very small aperture of the order of 10^{-7} steradians and it is limited in resolution to $\sim 3 - 5\ \mu m$. A microscope concept was proposed by Wolter[18] in 1952 which overcomes both of these disadvantages. Shown in Figure 34 is a Wolter Type I microscope schematic. The microscope still utilizes grazing incidence reflection from x-ray reflecting surfaces; however, the surfaces are now a hyperboloid and an ellipsoid. The laser fusion target is located at F2 of the hyperboloid and the image is located at F2 of the ellipsoid. F1 of the hyperboloid and ellipsoid are common points and are the virtual image of the target. We have designed microscopes of this type with an object distance of 30 cm and magnifications of 9, 22 and 50. Ray trace calculations[19] have shown that we can obtain a resolution of better than 1 μm over a field of view at the target of 0.5 mm. The attainment of this resolution is governed by the manufacturing tolerances of the

reflecting surfaces. To attain this resolution requires that the surface figure along the optical direction have an accuracy of ~250 Å. This is the most stringent tolerance, however, the other tolerances such as centering and roundness are also stringent. We have fabricated a number of these Wolter type microscopes[19,20] utilizing the single point diamond turning technique. Shown in Figure 35 is the ideal contour for one of the hyperboloid reflectors. Notice that the horizontal scale is in milimeters, whereas the vertical scale is in units of 1000 Å. The middle curve shows one of the contours produced in the diamond turning process. By measuring this contour we were then able to correct the tape for the numerically controlled machine, remachine the surface and produce the bottom contour which is the corrected contour. This contour has the required accuracy of 250 Å. To achieve the theoretical reflection efficiency curves in the 3 - 4 keV spectral regime[21] we require a surface smoothness on the order of 50 Å. Thus, we are not able to utilize the diamond turned mirrors directly, we must hand polish the surface and attempt to retain the diamond turned figure while producing the require smoothness. In Figure 36 on the left we show an example of a mirror in which significant figure contour error was introduced in the polishing process and the resultant 8 μm resolution of an x-ray micrograph showning a stainless steel wire grid. A subsequent attempt at polishing one of the microscope mirror pairs is shown on the right and there is an obvious improvement over the microscope on the left. However, again, additional errors were introduced in the polishing process and the resolution achieved in the x-ray micrograph is 4 μm. Figure 37 shows one of the diamond turned microscope mirror pairs after the polishing process. We have also overcoated the Ni surface with 1000 Å of Au.

Another technique which we have utilized to measure the spatial distribution of the x-rays is the Fresnel zone plate coded imaging.[22] In Figure 38 we show a schematic of the principle of this concept. A freestanding Fresnel zone plate is fabricated using gold in thicknesses from 1.5 to 5 μm. A source point then casts a shadowgraph of the zone plate onto a recording film. In this application we are utilizing the zone plate in the coded imaging mode rather than in the defraction mode and therefore the x-rays must be short enough in wavelength that defraction is not important in the narrowest zone. The recorded shadowgraph is then developed and irradiated using a coherent light source. The coherent light source then produces a Fresnel defraction pattern which produces the reconstructed image of the source points. As can be seen in Figure 38 this technique has not only planar resolution but also tomographic resolution. In Figure 39 we compare the characteristics of x-ray microscopy with zone plate camera imaging. The planar resolution limit for the microscope is $\sim$ 1 μm whereas the zone plate is limited to $\sim$ 5 μm by defraction. The collection solid angle of the microscope is $\sim 5 \times 10^{-4}$ steradians whereas the zone plate has $\sim$ 1 steradian collection efficiency. However, it should be remembered that the zone plate will be close to the target $\sim$ 1 to 2 cm object distance, and therefore for high intensity radiations the zone plate will most likely be destroyed on every target shot. The microscope has no tomographic resolution. It appears that we will be able to achieve tomographic resolutions of $\sim$ 10 μm with the zone plate coded imaging.

The microscope is limited to the soft x-ray regime less than 6 keV. The zone plate camera is particularly useful for the high energy x-rays above 7 keV and thus is useful for imaging the suprathermal x-rays.[23] In fact we have utilized a zone plate to make this measurement. The thickness of the zone plate was ~ 5 μm of gold. It had 100 zones with the narrowest zone being 3.4 μm. Shown on the right in Figure 40 is the spectral response of the zone plate imaging system and on the left is a reconstructed x-ray image from a Hyperion glass shell target. The initial diameter was 90 μm and we see that the faint outer image is equal to the initial diameter of the target. The central more strongly emitting region is undoubtedly due to the compressed core where the thermonuclear reactions are taking place. The bright spot near the top of the corona region is the emission from the stalk which supported the glass shell. The reason that it extends down into the corona is that we are observing the target from an angle of 45° below the horizontal and thus we are viewing the stalk through the target. The images of the thermal x-rays from the imploded shell and fuel have always been confusing to interpret with respect to determining the final compression. This is due to the strong contribution of the emission from the high Z pusher. The imagining of the suprathermal x-rays may provide a means of viewing the implosion core without this confusing radiation from the pusher. However, the data presented in this figure is still preliminary and subject to a further analysis.

Another concept for determining the size of the emission region is to place a high Z additive inside the pusher along with the fuel. One

can then look at emission specifically from the high Z additive and image it. An implementation of this concept is shown in Figure 41. Here we have arranged the crystal close to the target and the film plane close to the crystal. For a small emission region it can be seen that the width of the emission lines in the film plane are representative of the size of the emission regime in the target. We have built such a spectrograph to look at the Ar lines or the Ca lines. Ar would have to be difussed in through the glass microshell, Ca already exists as a trace element in our glass microshells. We have calibrated this spectragraph using a 8 μm pinhole and a soft x-ray machine and demonstrated the required resolution.

The temporal behavior of the heating of the ablation front and the pusher fuel implosion dynamics are sufficient reasons to devote significant effort to providing temporal resolution of the x-rays. We have converted our optical streak tube technology to a streak camera which is sensitive to x-rays in the 1 - 30 keV spectral regime. As shown in Figure 42, we have replaced the optical photocathode with a x-ray photocathode. This consists of a 125 μm by 1 cm slit which is covered with a Be window. On the back side the Be window is coated with a 1000 Å of gold. We have measured the spectral distribution of the photo electrons emitted from a gold cathode and from this information and the streak tube characteristics we have inferred a temporal resolution of 15 ps. The temporal resolution is demonstrated in Figure 43 where we have irradiated a glass microshell target 87 μm in diameter at 0.4 TW with a 70 picosecond pulse.[24] K-edge filter strips were placed along the slit of the streak camera thus providing a number of energy recording channels.

On the left, three temporal records are shown for x-ray spectral bands centered at 2.6, 4 and 5.3 keV. The rapid rise of the beginning of the pulse appears to be limited by the temporal resolution of the streak camera which we have previously quoted as 15 picoseconds. This data can also be used to infer a temporal behavior of the "temperature" emitted of the glass microshell. Replotting the three curves as x-ray spectra at four times during the experiment we get the figure on the right. As one would expect from a thermal distribution the curves are exponentials and indicate that "temperatures" between 500 - 600 eV are produced. The time integrated spectrum from this same target produced a thermal slope of 630 eV. The two peak temporal distribution of the higher energy x-rays is typical of an exploding pusher target x-ray emission when the pulse is reasonably matched to the implosion velocity and diameter of the target. Additional x-ray vs time signatures are shown in Figure 44. The upper two curves are for experiments which are nearly identical showing the repeatability of the temporal distribution of the x-rays. These both show the two maxima behavior of the temporal distribution of the x-rays from a glass microshell target. The third target, number 517, had a much lower energy and power pulse incident on the target resulting in a factor of 7 - 9 decrease in the neutron yield and the second maxima in the x-rays is significantly reduced due to the lower implosion velocity.

A Au disk target was irradiated[25] with the one beam of the Argus laser with an intensity of $\sim 10^{15}$ W/cm^2. The time history of the x-ray emission was recorded using the x-ray streak camera and nine K-edge filters. Their thicknesses are indicated in figure 45 where we shown film record. Thus we obtained nine spectral channels of data from this

x-ray streak record. The data from Figure 45 is then converted into relative x-ray intensity for five of e channels as a function of time. This data is shown in Figure 46. We can again turn this data into x-ray spectra for various times to show the variation of the "thermal" and suprathermal temperatures. These curves are shown on the right of Figure 46 and each of the curves clearly demonstrates the thermal and suprathermal of the x-ray spectrum. The thermal temperature, Θ_c, is the implied exponential slope from the broadband response of the filters and streak camera. The electron, temperature, T_e, of the Au plasma is 300-400 eV and a considerable fraction of the "thermal" x-ray emission recorded is line emission. A second more complete example of this data is shown in Figure 47. In Figure 48 we then are able to then plot the thermal temperature and suprathermal temperature as a function of time. The thermal temperature appears to peak slightly ahead of the suprathermal and the suprathermal temperature appears to decrease slightly slower than the thermal temperature. However, the ratio of the two temperatures appears to be approximately constant between 4 and 5.

As we have indicated, the x-ray streak camera in its present configuration is limited to measuring x-rays above 1 keV. This is because of the Be window on the front of the streak tube. Work is continuing to develop photocathodes which transmit at lower energies and also to develop windowless versions of the x-ray streak camera. In the meantime we have implemented another technique to measure the temporal behavior of the x-ray spectrum from 100 eV up to 1 keV. We have developed fast windowless x-ray diodes which have a temporal rise time of 60 to 70 picoseconds.[26] If we can couple these x-ray diodes together with appropriate spectrum discrimination and the use of recently

developed fast oscilloscopes, then we expect to be able to provide temporal resolution of the order of 100 to 300 picoseconds. For high density implosions the shape of the laser pulse generally begins with a low intensity portion and then builds up to the end to high intensity.[2,3,4,5] The low intensities on target naturally produce lower temperatures and thus the subkilovolt region of the x-ray spectrum is of more concern. It is also generally true that this portion of the pulse has a longer characteristic time, generally on the order of 0.5 nanosecond or longer and thus the above technique of using the windowless x-ray diodes and fast oscilloscopes is appropriate to measuring the temporal behavior of the subkilovolt portion of the x-ray spectrum. We have basically used the same concept for spectral discrimination that we utilize in the x-ray microscopes. A filter provides the low energy cutoff and grazing incidence reflection from a polished flat mirror surface provides the high energy cutoff. The implementation of a three channel version of this time resolved spectragraph which we can Dante is shown in Figure 49. Three channels have been provided by the utilization of two nickel mirrors, one silicon mirror and filters of varying thickness of nickel. In Figure 50 we shown the spectral response functions of these three channels. For some spectra of interest three channels are not sufficient to provide proper definition and therefore we are continuing to develop this concept and add additional channels to the Dante detection system.

We have the option with the x-ray streak camera of utilizing the spatial recording dimension of the streak camera to provide spatial distribution of x-rays rather than spectral distribution as we have

previously discussed. We have implemented this option by coupling the x-ray streak camera to a dichroic pinhole camera.[27] The goal was to image the x-rays from an imploding glass microshell target and follow the temporal distribution of x-rays from the implosion. The particular problem presented by this requirement is the very precise alignment of the diocroic pinhole with the slit of the streak camera such that the slit of the streak camera is views the equatorial plane of the glass microshell. Typical target sizes were 60 to 70 μm and therefore the aiming of the pinhole camera had to be accurate within < 6 μm to properly image the equatorial region of the imploding glass microshell. The diocroic pinhole was formed by drilling a 6 μm hole in tungsten glass to provide the x-ray pinhole. The tungsten glass was then backed with a concentric piece of gold with 125 μm diameter pinhole in it. The alignment system shown in Figure 51, then utilized a helium neon laser to view through the optical pinhole of 125 μm. This eliminated the diffraction problem of properly, optically aligning the the pinhole camera with both the target sphere and the slit of the x-ray streak camera. Targets were irradiated using the Janus laser system at ∿ 0.2 TW per beam and using the spherical illumination[28] system to provide nearly spherically implosions. In Figure 52 we show the color isodensity contours of the pinhole streak camera records for a two sided irradiation and a single sided irradiation of nominal 70 μm diameter microshells. The trajectories shown dotted on the figure are the peak x-ray emission at a given time. From LASNEX calculations it appears that these trajectories locate the position of the pusher gas interface during the implosion. The single sided irradiation shows that if one collapses a hemisphere that part of the matter will jet through and part of it will return back towards the side from which it was irradiated. In Figure 53

we show comparisons of two time resolved pinhole pictures with the x-ray microscope pictures which are time integrated. In the experiment on the right the target and the pulse width were not well matched and the x-rays continued to increase in intensity throughout the implosion and stagnation of the pusher. This characteristic is shown both in the time resolved picture and in the x-ray microscope picture. The implosion shown on the left is for a target which is actually larger than the optimum for the pulse length. In this case, the target was irradiated with the two foci coincident with the center of the target sphere. It appears, however, that the beam coming from the right had slightly more energy and produced an off center implosion. The off center nature of the implosion is clear in both the time integrated and the time resolved emission pictures in which there is a central minimum of x-ray emission in the core region at 56 μm from the initial position of the right side of the sphere.

Significant information relevant to the dynamics of the implosion and to the dynamics of the laser are obtained with our fast time resolution streak cameras. However, it would also be very useful to be able to obtain a full frame or two dimensional image of these types of emissions. We have, therefore, developed a ultra fast framing camera which we will utilize both with optical and x-ray photocathodes.[29] The operation of this streak camera is shown in Figure 54. A time varying image is formed on the photocathode which produces an image of electrons which are then accelerated and swept in time. This continuous image of the event is then swept across slits in the disector plane. The disector plane then converts this two dimensional image into spatial information

in one direction and spatial information in time for the other direction. These images which now have one of their spatial dimensions in time are reconstructed with restorer deflectors which reconvert time back to a vertical dimension, thus framed restored images are recorded on a phosphor screen and reconverted to photons for recording with photographic film. A prototype of this framing camera has been constructed and utilizing electrons through a shadowmask we have demonstrated the ability to produce images with a frame exposure time of 200 picoseconds. This system will ultimately have a capability of a frame time of less than 100 picoseconds. We have presently ordered a prototype version of this framing tube with an x-ray photocathode.

VI. PLASMA DENSITY DISTRIBUTION - NEAR FIELD AND FAR FIELD

Interferometry has been a time honored method for determining the distribution of fluid and plasma densities for cases in which the distributions were two dimensional. With the advent of lasers, in many cases, it became more convenient to develop holographic interferometry because of its reduced requirements on the quality of some of the optics in the system. Also since all of the phase information is recorded the focusing of the interferometer is not so crucial and can be examined in detail in the reconstruction process. The two central problems in utilizing holographic interferometry for density distributions in laser fusion pellets is to provide a short enough wave length pulse so that the high densities near the critical density of the laser radiation can be probed and also to provide pulses which are short enough in time to freeze the motion of the plasma during the exposure of the hologram.

We have implemented a holographic interferometry setup on the Janus target irradiation facility.[30] We split off 50% of the oscillator pulse and send it through a YAG amplifier in the double pass configuration and through a spatial filter. After apodizing the beam we frequency double it with a KDP crystal keeping the frequency conversion efficiency at 10%. By operating in the low conversion regime we obtain pulse shortening. The pulse then is propagated into a ADP crystal where again we have frequency doubled with a conversion efficiency of 10%. The output pulse is then at a wave length of 2660 Å and has been reduced 50% in pulse width from that of the oscillator. This system is shown in Figure 55. A moveable prism set is included to allow for path length adjustment for synchronization with the target irradiation pulse. The pulse from the oscillator for these experiments was typically a 30 picosecond Gaussian pulse and at the target chamber it produced between 0.5 to 5 joules for target irradiation. The pulse for the holographic interferometry was typically 15 picoseconds in duration and about 3 microjoules of energy. The probe beam and the reference beam are then directed into the target chamber through a lens and a 10x microscope objective was used to provide high resolution observation of the fringes at the target. The lens used to irradiate the targets was either an f/1 or f/10 lens depending upon the experiment. A schematic of the Janus holographic interferometry set up is shown in Figure 56. Glass microshells 40 μm in diameter provided the shortest lateral plasma path length so that we could probe deepest into the density distribution. Flat disks were also irradiated to determine plasma density distributions associated with a series of flat disks irradiated at various angles in p and s polarization for a resonance absorption study.[31] Holograms of

the typical 40 m diameter glass microshell target are shown in Figure 57. The advantage of this technique in being able to adjust the focus of the reconstruction system is clearly shown here. Typically the stalk supporting the glass stalk was located along a radial line from the center of the sphere and thus if we wish to probe through the plasma we should bring the glass stalk into sharp focus. A properly focused hologram is shown in the center image and an improperly focused hologram is shown in the image on the right. Many more fringes are observed in this latter image and would lead to significant errors in the interpretation of the density distribution.

A typical holographic interferogram is shown in Figure 58 where the target was irradiated at $\sim 10^{14}$ W/cm^2 with an f/10 lens. The interferometer fringes have been Abel inverted to produce the electron density distribution as a function of radial position along the axis of the laser beam on the right. The curve starts at a density above critical density and proceeds smoothly down to approximately critical density. Then there is a steepening of the following portion of the density distribution to a point which corresponds to the radiation pressure balancing of the thermal density and then the density distribution smooths out again. This is the first direct demonstration of the profile steepening due to radiation pressure from the incident laser pulse.

We continue to develop new techniques to measure the distribution of plasma in the pellet and its corona. This is the most fruitful area

to continue developments because measurements made in the pellet and corona reveal directly information associated with the interaction and implosion processes. As is already evident, this is a very topical area for the development of diagnostics. In some cases, interesting information can be obtained by observing phenomena far from the pellet itself. One example is the determination of the polarization state of light reflected and scattered by the laser plasma interaction. By locating an ellipsometer appropriately with respect to the angle of the incident beam and the expected specular reflection from a laser irradiated target one can deduce parameters such as the scale length in the region of the critical density. This, of course, is related to the question of the radiation pressure leading to the steepening of the density distribution. A complete measure of the polarization state of the refracted and scattered light can also lead to information about other plasma processes such as resonance absorption, rippling of the critical density surface and Brillouin scattering.

We have implemented an ellipsometer on some experiments which measures six quantities which are then sufficient to determine the four Stokes parameters which define the polarization state of the light entering the ellipsometer. Figure 59 shows the optical assembly and the photodiode detectors which are used to measure the six beams produced by the three prism elements in the ellipsometer. An example of the utilization of this data is shown in Figure 60 where we show the measured degree of phase retardation of the refracted and scattered light beam as a function of the angle of incidence, the scale height and the density jump at the radiation pressure modified density profile. Measurements

have been made on a variety of targets, both planar and spherical[30] which are consistent with density scale heights of less than 2 μm and in some cases as small as a 0.10 μm.

For high intensity target irradiations, suprathermal electrons are produced by the collective processes of the absorption of the laser energy. As a result one may expect that electrons will escape from the quasi neutral distribution of the plasma corona and can be detected by an electron spectrometer at large distances from the target. Figure 61 shows our magnetic electron spectrometer which deflects the electrons through 90 degrees onto silicon PIN diode detectors. This system has been used with a large number of target experiments and has provided data on the number of electrons and their energy distribution. However, it must be cautioned that the distribution of the electrons which are detected by the spectrometer are complicated by the target mass and the connection to the target chamber and the target chamber surroundings.

Asymptotic plasma energy distribution in the form of the plasma ions has been a subject of considerable discussion in the literature. Because of their simple nature and ease of fabrication most of the measurements have been made utilizing Faraday cup detectors. As a general nonquantitative survey instrument these Faraday cups serve a general useful purpose. However, if one wishes to know the distribution of high energy ions from the laser target at a large distance other techniques must be employed. The basic problem with the Faraday cup method of detection is the emission of secondary electrons from the detecting surface and the concommitant charge buildup in the region of

the detector. There have been a number of more quantitative plasma ion detectors fabricated. Two examples are the Thompson parabala which utilizes parallel electric and magnetic fields to separate charge state and energy. Another is the double focusing magnetic spectrometer utilizing cellulose nitrate as the detecting medium. A third example is shown in Figure 62 in which we utilize a magnet to deflect constant values of mE/q^2 onto different detector planes. As shown in Figure 63 we also determine the mass to charge ratio by the time of arrival of various peaks in each one of the detectors. In some earlier experiments a number of investigators mistakenly determined that a very large fraction, up to 80% of the absorbed laser energy was appearing in what they turned a "fast ion" component. Subsequently we among others have shown that the interpretation of these measurements was in error. A significant portion of that signal known as "fast ions" was in fact hydrogen ions. Since their charge to mass ratio is one the faction of energy contained in these high velocity ions was not as significant as previously believed. More importantly, with respect to the observation of the asymptotic plasma energy distribution the comment should be made that the observation of a physical phenomena where the distance of the point of observation is very large compared to the target diameter, $L/D \rightarrow \infty$, and the time of observation is much greater than the implosion time, $t/\tau_{imp} \rightarrow \infty$, then it is very difficult to interpret the results with respect to the phenomena occuring in the interaction regime and in the implosion of the target itself. Thus, although these asymptotic plasma instruments are of interest and contribute some information to the overall plasma processes we should continue to focus the major portion of our attention on the plasma distribution in scale lengths and time scales associated with the interaction and implosion of the laser fusion pellet.

VII. REACTION PRODUCTS

Because the goal in laser fusion is to produce net power and convert the reaction products to electric power, clearly one of the most important measurements is the total thermonuclear energy produced for either the DD reaction or the DT reaction. This measurement is relatively straightforward because the neutrons produced have high energies, 2.45 and 14.1 MeV and therefore will penetrate even large amounts of steel or lead. Therefore, the detectors may be placed at large distances from the target without concern for a clear penetration into the target chamber. The most versatile detector of neutron yield is the time of flight detector which utilizes a NE 111 fluor and a fast photomultiplier. The neutrons interact with the fluor to produce photons which are measured with the fast photomultiplier. The systems which we use also contain a pulsed light source for routine calibration checks. The response of this system to a delta function impulse is shown along with the detector in Figure 64 and we see that it produces a 4 nanosecond FWHM voltage pulse which we typically record on a fast oscilloscope. The sensitivity of this system is also shown in the figure. In typical laser fusion experiments there is an x-ray and gamma flash which occurs at the time of the laser implosion. These x-rays and gamma rays typically also penetrate the fluor detector and produce a signal which can be confused with the neutrons. However, because of the difference in the transit times we are able to separate the x-ray and the neutron signals. These

detectors are most versatile because they can be placed in almost any position with respect to the laser irradited target. For very low yield experiments we have been able to detect as few as 200 reactions generated in a laser imploded target.

It is difficult to calibrate the time of flight neutron detectors in terms of absolute yield.[33] To circumvent this problem we have employed an activation counter in which a copper disk is utilized.[34] The copper disk is placed in close proximity to the laser irradiated pellet. The 14 MeV neutrons from the DT reaction then produce n,2n reactions in the copper changing the stable ^{63}Cu isotope into ^{62}Cu . The activated disk is then placed in a coincidence counter with two NaI crystals on either side of the disk. The ^{62}Cu decays to ^{62}Ni and a positron with a half life of 9.8 minutes. The positron is then annihilated with an electron to produce two gamma rays in opposite directions of 0.511 MeV. The reaction threshold for the n,2n reaction in the ^{63}Cu is 10.9 MeV thereby providing good discrimination against low energy scattered neutrons. The cross section for the reaction is 0.5 barns and the positron decay of the ^{62}Cu represents 97% of the decay processes. We are utilizing this counter system with present Argus experiments where the disks size is 76 mm diameter by 9.5 mm thick the source to target distance was 41 cm. The present detectability is 10^8 neutrons. The system is shown in cartoon in Figure 65. The copper disk activation system was calibrated using a high energy deuterium beam irradiating a tritiated target. The calibration accuracy of this system is $\sim$ 10%. With high yield Argus experiments above 10^8 neutrons we have utilized the copper activation as the standard to recalibrate the time of flight detectors.

The reaction products are not only a measure of the total reaction energy, they also provide significant information as to the reaction processes and the density and temperatures at which these processes occur. For example, the energy distribution of the reaction products is an indicator of the energy distribution of the reactants, thus it can be used to determine whether the reactions are of a beam-beam, beam target or a true "thermonuclear" condition. Early laser fusion targets have operated in what has been termed the exploding pusher mode where the pusher explosively decompresses inward and outward to provide compression and heating of the fuel. The final ρr produced in the fuel and the pusher are generally quite small of the order of 10^{-3} to 10^{-4} gm/cm^2. Since the range of the alpha particles for typical thermonuclear temperatures is $\sim$ 0.1 gm/cm^2 it is clear that the alpha particles leave the reaction region and pass through the pusher with only small modification to their energy distribution and their average energy. Thus, if we measure the energy distribution of the alpha particles we can make a determination of the nature of the reactions. Further the energy of the reacting particles or their temperature in a Boltzmann distribution is determined by the FWHM broadening of the energy of these reaction products. In Figure 66 we show a alpha time of flight spectrometer which was used in experiments on Janus in May 1975 to demonstrate the thermonuclear nature of the reactions and to measure the 1 - 2 keV temperature of the DT ions in the compressed core.[8] This system uses a collimating tube assembly which contains baffles to reduce scattered particles reaching the detector, a defining collimator and a

deflection magnetic to deflect the alpha particles onto a bare NE 111 fluor coupled to fast photomultiplier. Because the alpha particles from the DT reaction have 1/4 the energy and 1/4 velocity of the 14 MeV neutrons produced in the same reaction it is possible to place the alpha time of flight detector a factor of 16 times closer to the target chamber than a neutron time of flight detector with the same energy resolution. Note that the energy resolution of a ToF detector is given by $\Delta E = 2Ev\ \Delta t/L$. A factor of 16 in distance and an increase in the affective size of the detector which can be used with the alpha particles leads to a detectability for the alpha time of flight system of 5×10^5 reactions.

For neutrons we built a time of flight detector for Argus[35] which is shown in Figure 67. This system has been placed at a distance of 45 meters from the target chamber and can produce useable time of flight signals for energy distributions at yield levels of 3×10^8. This spectrometer as configured for Argus utilizes collimators a short distance from the target chamber and two water shield tanks, one located just outside the building and the other located just in front of the detector station to reduce the sensitivity of the time of flight detectors to scattered neutrons. Data from these two systems for an Argus experiment is shown in Figure 68. The upper trace is the neutron time of flight signal which shows the energy of the neutrons as being the expected 14 MeV, the broadening was 423 keV, and since $\Delta E_{FWHM} = 177 \sqrt{T_i} \sim$ keV we calculate an ion temperture of 5.7 keV. The lower trace shows the alpha particle signal and in this case we measure a larger spread of the energy of the alpha particles. We also observe a down shifting of the average energy of the alpha particles. This is to

be expected since the alpha particles must pass through the fuel and the pusher to arrive at the detector thus we expect an average decrease in the energy of the alpha particles of 200 - 300 keV. The inferred temperature has not been corrected for broadening due to passage through the fuel and the pusher and thus the 6.7 keV ion temperature which we infer is consistent with the 5.7 keV ion temperature measured by the neutron time of flight system. The reduction of the time of flight data to energy distribution is shown in Figure 69. Because of the small number of neutrons interacting with the detector even at these high yields of 7×10^8 the error bars on the broadening of the distribution can still be significant. The energy broadening error is linear in t but then since the ion temperature squares the errors of the energy measurement, errors of 15-20% are typical in determining the ion temperature from the neutron time of flight.

Another technique which can be used to measure the temperature of the reacting products is to utilize the ratio of the number of reaction products from two different reactions. This ratio is only a function of the initial concentrations and the ratio of the Maxwell average crossections of the two reactions. For the DD reaction in the D^3He reaction the ratio of the cross sections varies by three orders of magnitude over the temperature range from 1 - 10 keV. Thus, by measuring the ratio of the number of 14.7 MeV protons produced in the D^3He reaction to the number of 3 MeV protons produced in the DD reaction we have a very sensitive thermometer for the fuel reaction temperature. On Argus experiments with exploding pusher targets this method has produced results which are in agreement with neutron and TOF experiments.[36]

The size and the distribution of the compressed core can be measured by imaging the reaction products. This measurement has been made for an inertially confined DT reaction which produced of the order of 10^{12} neutrons.[37] In this case, a pinhole camera was used to image the 14 MeV neutrons and the recording medium were plates activated by the 14 MeV neutrons. This technique will become useful in high yield experiments. However, at present the yields are in the 10^8 to 10^9 range. Again recognizing that the targets produce low values of r in the fuel and the pusher we can image the alpha particles instead of the neutrons. One significant advantage is that the alpha particles are easily stopped with 10 m thickness of gold and thus small pinhole or other imaging devices can be generated and placed at very small object distances with respect to the pellet implosion. We have implemented both pinhole[38] and zone plate coded imaging[39] cameras to image the alpha particles from our exploding pusher targets. The recording technique is illustrated in Figure 70 in which we shown the emissions and their energies from the laser irradiated pellet. The high energy ions from the pusher are stopped in the filter which also serves to attenuate the x-rays which can cause significant bulk damage in the cellulose nitrate recording film. The alpha particles leave damage sites in the cellulose nitrate which are converted into pinhole tracks by etching the cellulose nitrate disk in a sodium hydroxide solution. Other high energy particles are either stopped in the filter or produce distinctly different tracks than those produced by the alpha particles. The x-rays which penetrate the filter produce bulk damage in the cellulose nitrate and do not produce pinhole tracks. Figure 71 shows an example of alpha particle

pinhole tracks in cellulose nitrate produced with a zone plate camera. The implementation of the alpha pinhole imaging system on Argus is shown in Figure 72. The pinhole camera is shown on the right together with the tantalum filter and the cellulose nitrate detector. Data from a 3 TW irradiated glass microshell of $\sim$ 90 μm diameter is shown on the left. The distribution of the pinholes recorded in the cellulose at the time of the reaction occupied a space inside the initial target sphere $\sim$ 1/3 the initial diameter. This data indicates that compression of the fuel was greater than 30. It must be remarked, however, that the diameter of the pinhole used for these experiments was 25 μm thus the resolution of the camera is $\sim$ 30 μm for the magnification used. Higher yield shots for the projected 6 TW capability of the Argus system and the 30 TW capability of the Shiva system will allow the utilization of much smaller pinholes and concommitant increase in the resolution of the imaging system.

The implementation of the zone plate camera for alpha imaging is shown in Figure 73. The 2.5 mm diameter zone plate is shown on the right. The thickness of the zone plate was 5 μm with the total numbers of the zones being 100 and the r of the narrowest outer zone was 5.3 μm. The planar resolution of this zone plate imaging system was 10 m. The reduced zone plate image from the same experiment shown in Figure 72 is shown on the left. The isoemission contours are shown along with vertical and horizontal distributions through the image. A slight ellipticity of the distribution is evident, however, since the extent of image in the vertical direction is 28 μm and 26 μm in the horizontal direction we should be careful not to infer too much from this spatial

distribution where the resolution is only 10 m. Again, with higher yields and further improvements in the fabrication capability of high accuracy high resolution zone plate we expect higher resolution images to be produced in the future.

Another use that can be made of the reaction products is to utilize the high energy neutron to produce activation of the pusher material.[40] The activation of the pusher material will be proportional to the density radius product and thus be a measure of the density distribution at burn time. An example of the use of this concept is shown Figure 74. The DT reaction produces the 3.5 MeV alpha particle and the 14 MeV neutron. The 14 MeV neutron in present experiments passes through the ^{28}Si in a glass microshell pusher. The ^{28}Si is converted to ^{28}Al by an n,p reaction. Now if one can collect the target debris one can then measure the decay of ^{28}Al back to ^{28}Si by beta decay with the coincident emission of a gamma ray. This nuclear process has a half life of 2.24 minutes. The energy of the gamma ray is 1.78 MeV and the beta ray has an energy of 2.86 MeV. Thus, the time scale of the half life is convenient for the removal of captured target debris and the rapid counting of the debris to determine the activated fraction. The high energy of the gamma ray and the beta ray make coincidence counting of the captured debris relatively simple. Figure 75 shows the relationship for the r of the pusher as a function of the neutron yield and the number of activations in the target. The experimental procedure is shown schematically in Figure 76. A cylindrical plastic collector is utilized so that the laser beams can enter through the open faces of the cylinder to irradiate the target and then a large fraction of the target

mass is collected by the cylindrical collector. The present measurements indicate that the counting efficiency will allow as few as 75 - 100 ^{28}Al atoms to be observed. For f/1 focusing lenses on Argus the fraction of the mass which is not collected is expected to be 12%. We have devised a technique for verifying the target fraction collected.

VII. SUMMARY AND CONCLUSIONS

The Laser Fusion Program at the Livermore Laboratory began a significant experimental program in 1971 and at that time it was concluded that large numbers of new diagnostics instruments and techniques would have to be developed to adequately diagnose the laser implosion experiments. Since that time we have developed a large number of new instruments and adapted a large number of well known techniques to our peculiar requirements in laser fusion. We have made significant advances in the development of imaging and the temporal resolution of our diagnostics. We will continue to commit significant resources to continuing developments in the diagnostics capability. The rationale is simply that we recognize that the rapid rate of progress in our program is due to our theoretical capabilities, our calculational capabilities, the ability to develop well characterized target irradiation facilities, our ability to fabricate the necessary high precision targets and our ability to make quantitative high resolution diagnostic measurements of the target experiments. An example of how these diagnostics are used and compare with the target design calculations is shown in Table IV. These data represent the efforts of over 100 man years of effort in the development, characterization, implementation and operation of our diagnostics on target experiments.

REFERENCES

1. J. C. Maxwell, A Treatise on Electricity and Magnetism, Vol. 1, third Edition, pp viii - x, Dover Publications, N.Y., 1954.

2. J. Nuckolls, L. Wood, A. Thiessen, G. Zimmerman, Nature 239, 139 (1972).

3. J. L. Emmett, J. Nuckolls, L. Wood, Sci. Am. 230, 24 (1974).

4. J. D. Lindl, "Effect of a Superthermal Electron Tail on the Yield Ratio Obtained from DT Targets Illuminated with a Shaped Laser Pulse," Nuclear Fusion 14, pp. 511 - 515, (1974).

5. Lawrence Livermore Laboratory Energy and Technology Review, UCRL 52,000-77-8, August 1977.

6. Lawrence Livermore Laboratory 1974 Laser Program Annual Report, UCRL 50021-74, Neutron Production, pp. 441-443

7. J. F. Holzrichter, et. al., "Implosion Experiments with an Asymmetrically Irradiated Laser Fusion Target," Plasma Physics, Vol. 18, pp. 675-680, February 1976.

8. V. W. Slivinsky, et. al., "Measurement of the Ion Temperature in Laser Driven Fusion," Phys. Rev. Letts., Vol. 35, No. 16, pp. 1083-1085, October 1975.

9. W. W. Simmons, "In Pursuit of Fusion; Argus Laser System at Livermore," LLL UCRL 78634, October 1976.

10. J. Hunt, P. A. Renard, and W. W. Simmons, Applied Optics, Vol. 16, No. 4, pp. 779-782.

11. James R. Greenwood, et. al., "Shiva Laser System Controlled by Computer Network," submitted for publication to the Industrial Research Magazine for consideration in its Noveember 1977 issue.

12. Lawrence Livermore Laboratory 1975 Laser Program Annual Report, UCRL 50021-75, Reticon - Streak Camera, pp. 399-401.

13. David R. MacQuigg, Lawrence Livermore Laboratory 1976 Laser Program Annual Report, UCRL 50021-76, Section T-208, to be published.

14. S. Gunn, Lawrence Livermore Laboratory 1974 Laser Program Annual Report, UCRL 50021-74, Laser Calorimetry, pp. 290-291.

S. Gunn, Lawrence Livermore Laboratory 1975 Laser Program Annual Report, UCRL 50021-75, Argus Laser Calorimeter Design, pp. 398.

15. Stuart Gunn, Viviane Rupert, John Ho' 'chter, Lawrence Livermore Laboratory 1975 Laser Program Annual Repor., Scattered Light Calorimeter, pp. 404-405.

16. Louis N. Koppel, "An Active-Recording X-Ray Crystal Spectrometer for Laser-Induced Plasmas," Rev. Sci. Instrum., Vol. 47, No. 9, September 1976.

17. F. Seaward, et. al., "Calibrated "Four Color" X-Ray Microscope for Laser Plasma Diagnostics," Rev. Sci. Instrum., Vol. 47, No. 4, April 1976.

18. H. Wolter, 1952a, Ann. Physik 10, 94.

H. Wolter, 1952b, Ann. Physik 10 286.

19. Michael J. Boyle and Harlow G. Ahlstrom, "Imaging Characteristics of an Axisymmetric, Grazing Incident X-Ray Microscope Designed for Laser Fusion Research," to be submitted to Rev. Scie. Instrum. for publication. August 1977.

20. P. C. Baker, et. al., "Diamond Polishing a Diamond Turned X-Ray Microscope," submitted to the San Francisco Area Workshop on Optical Fabrication and Testing, San Mateo, CA., February 27-28, 1976.

21. R. Giacconi, et. al., "Grazing Incidence Telescopes for X-Ray Astronomy," Space Science Reviews 9, pp. 3-57, 1969.

22. N. M. Ceglio, et. al., "Zone Plate Coded Imaging of Laser Produced Plasmas," Applied Physics Letters, Vol. 48, No. 4, April 1977.

23. N. M. Ceglio, et. al., "Zone Plate Coded Imaging (ZPCI) of Laser Compressed Targets," Bull. Am. Phys. Soc., Vol. 21, No. 9, pp 1078, October 1976.

24. D. T. Attwood, et. al., "Time Resolved X-Ray Spectral Studies of Laser Compressed Targets," Phys. Rev. Letts., Vol. 37, No. 9, pp. 499-502, August 1976.

25. P. H. Y. Lee, et. al., "Time Resolved X-Ray Spectral of Laser Irradiated High Z Targets," prepared for submission to Phys. Rev. Letts.

26. V. Slivinsky and H. Kornblum, "In Line Stacked and Windowless X-Ray Diode," Lawrence Livermore Laboratory 1974 Laser Program Annual Report, pp. 312-314.

27. D. T. Attwood, et. al., "Space Time Implosion Characteristics of Laser Irradited Fusion Targets," Phys. Rev. Letts., Vol. 38, No. 6, February 1977.

28. J. E. Swain, et. al., "Realities of the Janus 4 Illumination System," being prepared for submission to Applied Optics.

29. Ralph Kalibjian, "Optical X-Ray Framing Camera Tube," prepared for the 12th International Congress on High Speed Photography, Toronto, Canada, August 1-7, 1976.

30. Dave Attwood, "Holography," LLL UCRL 80132 Rev I., Submitted to Phys Rev. Letts.

31. K. R. Manes, et. al., "Polarization and Angular Dependence of 1.06 um Laser Light Absorption by Planar Plasmas," Phys. Rev. Lett., Vol. 39, No. 5, p. 281, August 1977.

32. D. W. Phillion, et. al., "Evidence for Profile Steepening of Laser Irradiated Plasmas," accepted for publication by the Phys. Fluids.

33. R. A. Lerche, Lawrence Livermore Laboratory, Laser Program Internal Memorandum on Calibration of Fluor-PM Neutron Detectors, DDG-76-273, 1976.

34. R. A. Lerche, Lawrence Livermore Laboratory, Laser Program Internal Memorandum on Calibration of Cu Disks, DDG-76-326, 1976.

35. R. A. Lerche, et. al., "Laser Fusion Ion Temperatures Determined by Neutron Time of Flight Techniques," LLL UCRL 79375, accepted for publication in Appl. Phys. Letts.

36. V. W. Slivinsky, et. al., "Implosion Experiments with D^3He Filled Microspheres," submitted to Journal of Applied Physics.

37. R. W. Bauer and R. C. Weingart, "A Time Resolved Fast Neutron Pinhole Camera for Studying Thermonuclear Plasmas," UCRL 77527, Conference on Diagnostics of High Temperature Plasmas, January 1976, Oakridge, Tennessee.

38. V. W. Slivinsky, et. al., "Pinhole Imaging of Laser Produced Thermonuclear Alpha Particles," Applied Phys. Letts., Vol. 30, No. 11, pp. 555-556, June 1977.

39. N. M. Ceglio and L. W. Coleman, "Spatially Resolved Alpha Emission from Laser Fusion Targets," Phys. Rev. Letts., Vol.39, No. 1, pp 20-24, 1977.

40. F. J. Mayer and W. B. Rensel, "Plastic Bubbles and Tamper R Measurements for Laser-Driven Fusion Experiments," Journal of Applied Physics, Vol. 47, No. 4, April 1976.

ACKNOWLEDGMENTS

This paper is a compilation of the diagnostic instrumentation developments of the experimental program in laser fusion at the Lawrence Livermore Laboratory. The groups which have contributed vital efforts towards these results are the Fusion Experimenta Program which includes the Laser Plasma Interaction Group under the direction of Erik Storm and the Diagnostics Development Group under the direction of Lamar Coleman. The Targets Program which is directed by John Nuckolls has groups which are responsible for Target Design, Plasma Theory under the direction of Bill Kruer, Code Development under the direction of George Zimmerman and Target Fabrication under the direction of Chuck Hendricks. The Solid State Lasers which we use for our experiments have been developed by the Solid State Laser Program which is directed by John Holzrichter and consists of a number of groups. In addition we acknowledge the farsighted direction by Carl Haussmann in the period of 1972 and 1975 in the direction of the laser program at Livermore and the direction of John Emmett and his staff during the period of 1972 to the present. Without the support of all of these groups our diagnostic instruments and their use in our experiments would not have been possible nor would they have achieved the level of accuracy and relevance to the National Laser Fusion objectives that we expect of our Program. Shirley Sanford, Gail Anderson, Ollie Parker, Doris Hine and the LLL Art Department are specially acknowledged for their work in the preparation of this paper.

DIAGNOSTICS REQUIREMENTS

$10^{16}\ cm^{-3} \leqslant n \leqslant 10^{26}\ cm^{-3}$

$1\ eV \leqslant T \leqslant 50\ keV$

$1\ eV \leqslant E \leqslant 14\ MeV$

$1\ \mu m \leqslant \Delta x \leqslant 1\ cm$

$1\ psec \leqslant \Delta t \leqslant 100\ nsec$

Data obtained on a single shot basis compatible with computer aided data acquisition

Table I

CURRENT STATUS OF LASER FUSION DIAGNOSTICS

Δt = 6 psec (infra-red)
= 15 psec (x-ray)
Δx = 1 μm (infra-red, visible, ultra violet; time integrated)
$\simeq$ 3 μm (x-ray; time integrated)
= 6 μm (x-ray; 15 psec time resolution)
= 50 μm (120 psec, full frame)
= 10 μm (α particles, ions)

$100\ \text{eV} \leqslant h\nu \leqslant 100\ \text{keV}$ (time integrated)
$1\ \text{keV} \leqslant h\nu \leqslant 20\ \text{keV}$ (15 psec time resolution)
$10^{16}\ \text{cm}^{-3} \leqslant n_e \leqslant 10^{21}\ \text{cm}^{-3}$ ($\approx$15 psec exposures)
$\Delta(h\nu) = 1\ \text{eV}$ at 1 keV
$\Delta E \simeq 100\ \text{keV}$ for 14 meV neutrons, 3.5 meV alphas

40-90-0377-1733 8/77

Table II

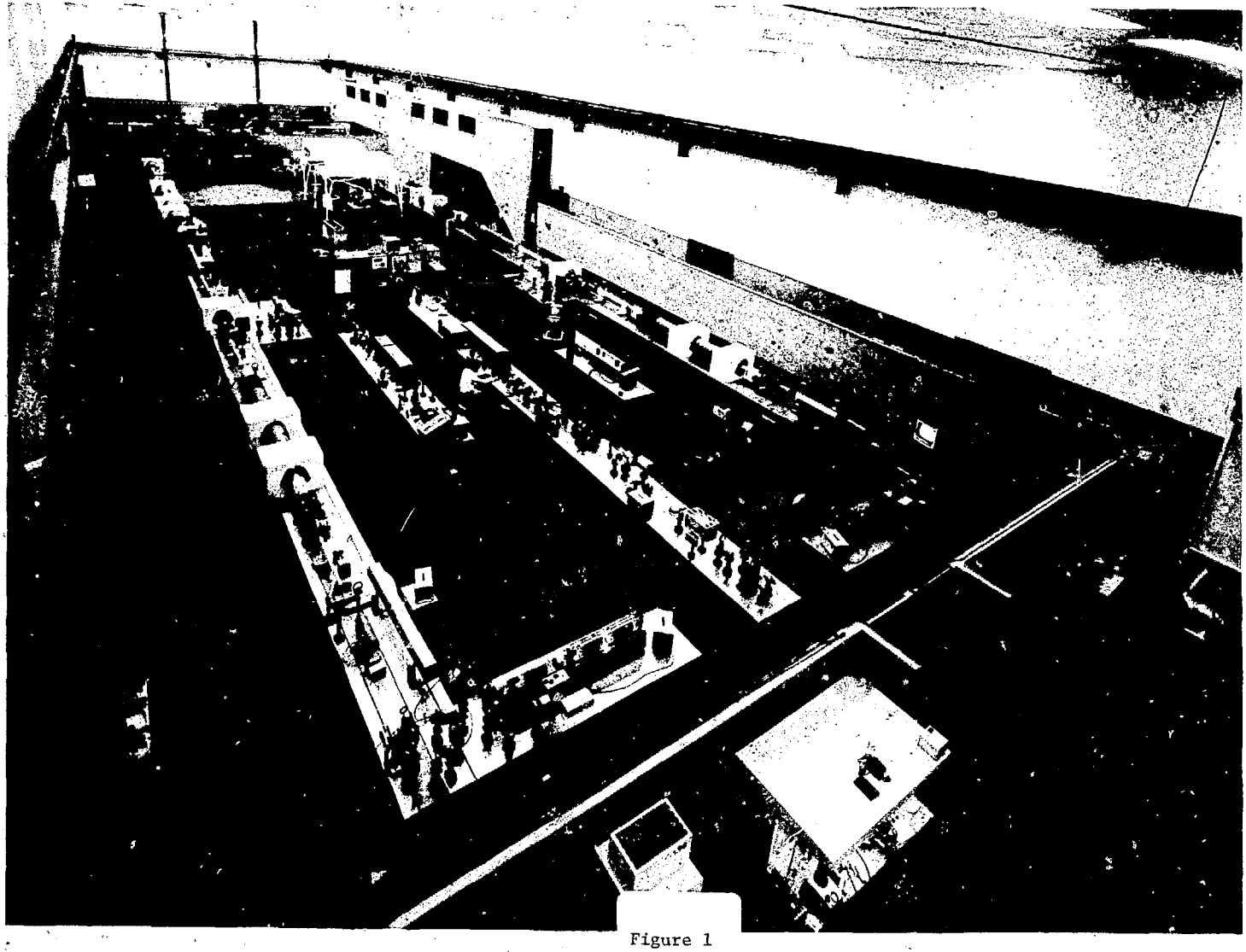

Figure 1

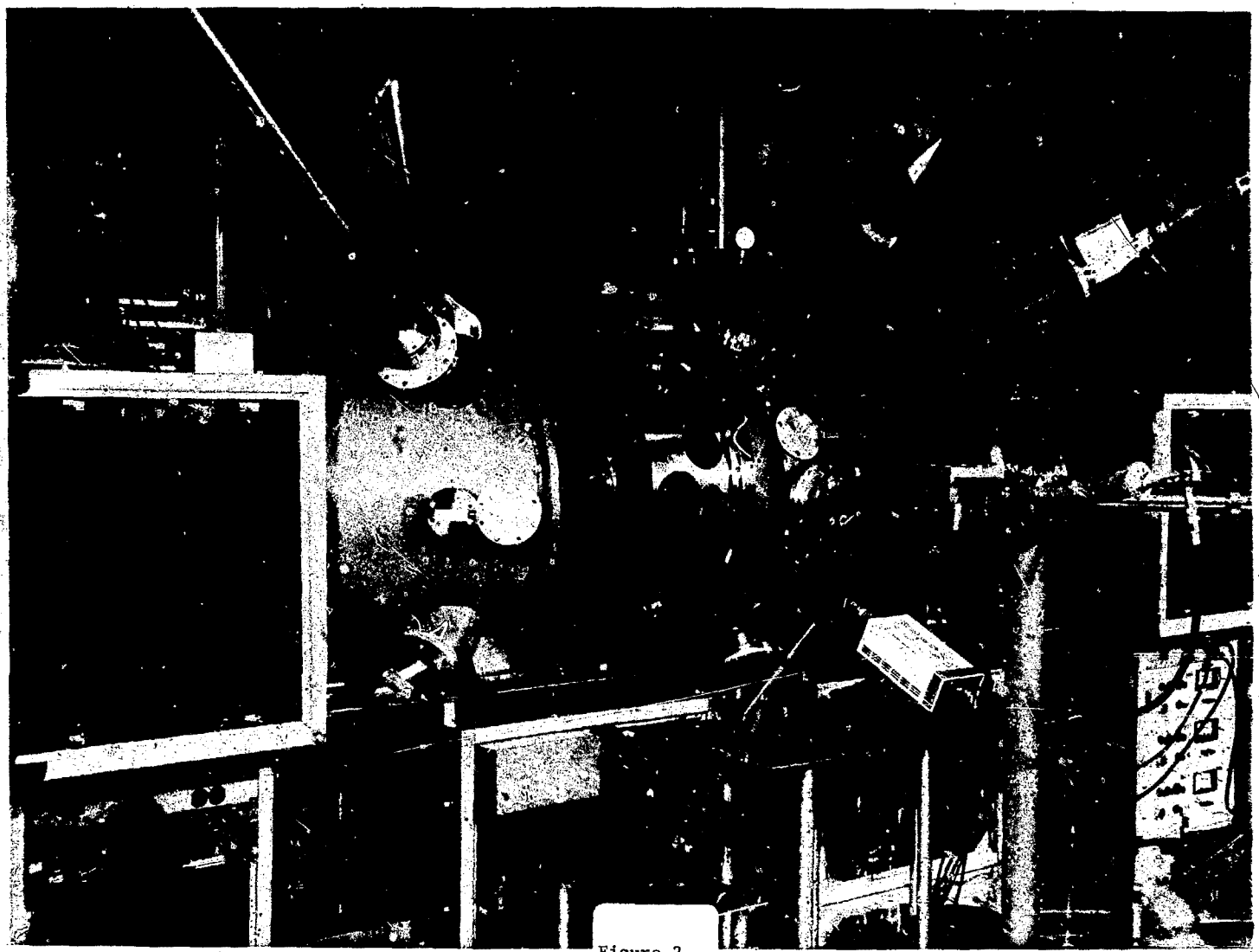

Figure 2

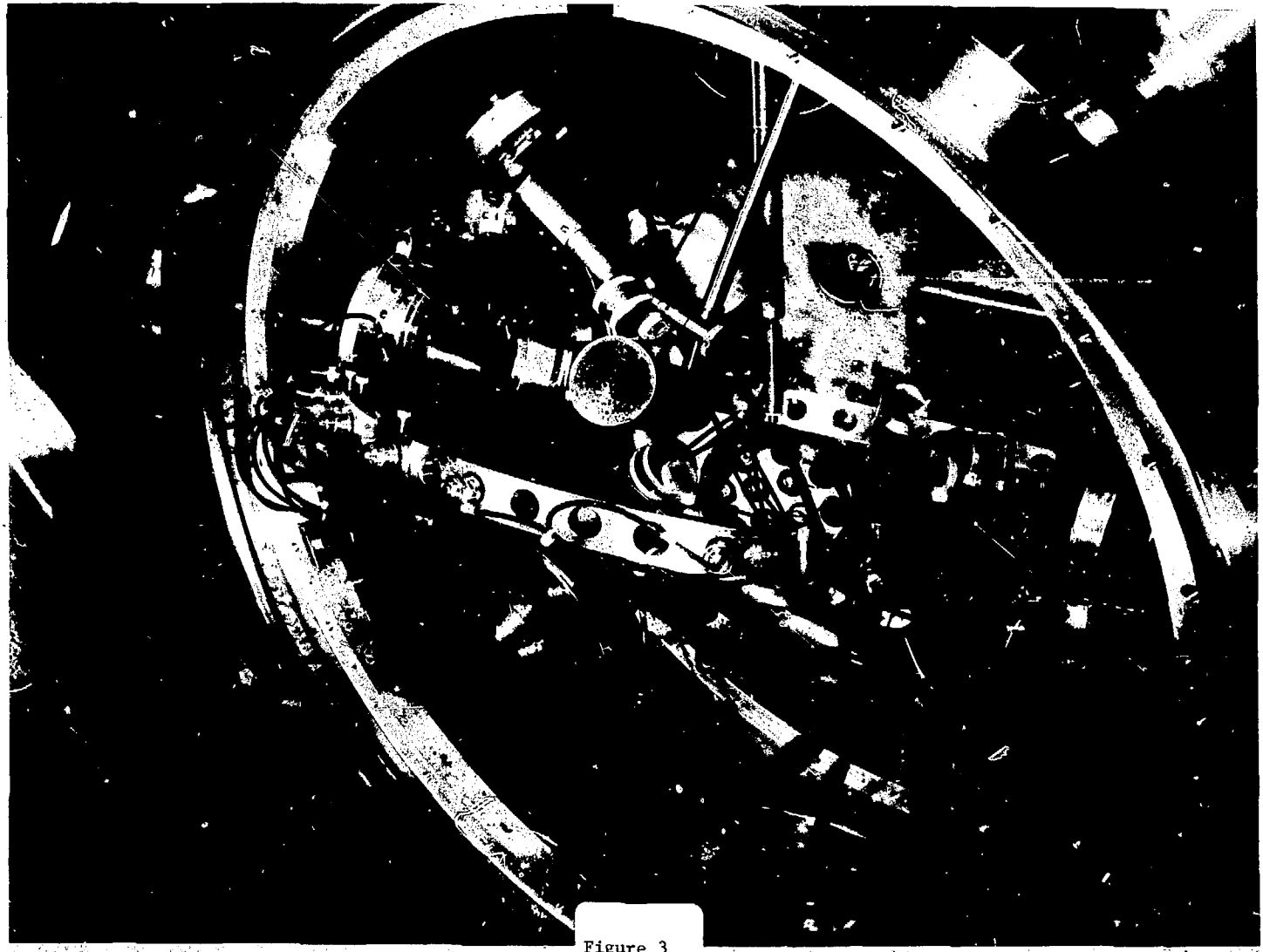

Figure 3

LASER FUSION EXPERIMENT DIAGNOSTICS

Measurement	Instrument	Record
Neutron count	1 Cu activation counter	Coincidence countering system
	1 time of flight detector (2 fluor-PM)	6 traces + 8 CAMAC channels
	2 fluor-PM systems (6 detectors)	12 traces
X-ray spectrum	Active-gypsum flat crystal	Digitized image from reticon array
	RAP bent crystal	Film
	CAR carbon reflector	Film
	Lead myristic bent crystal	Film
	7 channel K-edge filters	7 CAMAC channels
	4 channel K-edge filters	3 traces + 1 CAMAC channel
X-ray spatial distribution	1 axisymmetric x-ray microscope	Film
	2 x-ray microscopes (4 channels each)	2 Film (8 images)
	1 zone plate imaging system	Film
X-ray temporal character	4 LEXD	4 traces
	Filtered x-ray streak camera	Film (10 images)
X-ray calorimetry	4 SiSB detectors	4 CAMAC channels
	3 Ta foil x-ray calorimeters	3 chart records
α spectrum	1 Quadrupole triplet spectrometer	3 traces
	2 Magnetic-TOF spectrometers	6 traces
α image	1 Pin hole camera	Film
	1 Zone plate imaging system	Film
Ion energy spectrum	2 Magnetic spectrometers	4 traces
	1-4 channel CN detector	4 Films
Ion spatial distribution	8 Faraday cups	12 traces
	11 differential calorimeters	11 chart records
	1 pin hole camera	Film
Electron energy spectrum	Magnetic spectrometer	9 CAMAC channels
Second harmonic conversion efficiency	2 PIN diodes	2 CAMAC channels

20-90-0177-0411

8/77

Table IIIa

LASER FUSION EXPERIMENT DIAGNOSTICS

Measurement	Instrument	Record
Laser temporal and spatial distribution both incident and scattered	2 Target plane multiple image cameras	2 Films (50 images)
	2 Target plane streak cameras	2 Films (6 images)
	Forward and backscatter streak camera	1 Film (3 images)
	2 forward and backscatter multiple image cameras	2 Films (10 images)
Optical energy balance	North and South incident calorimeters	Computer (2 channels)
	North and South forward and backscatter calorimeters	Computer (2 channels)
	40 PIN diodes	40 CAMAC channels
	10-1.06 μm calorimeters	10 chart records
	or box calorimeter	6 chart records
Laser system performance	Oscillator streak camera	1 trace
	Switched out pulse energy diode	1 trace
	Pulse train monitor	1 trace
	Spark gap timing monitor	1 trace
	Prepulse monitor	1 trace
	7 interstage calorimeters	Computer (7 channels)
	6 nearfield beam photos	6 Films
	Flashlamp current monitors	20 traces
	Faraday rotator field monitors	10 traces

Total for one shot:
- 85 oscilloscope traces
- 82 data channels from computerized acquisition system
- 105 photographic images
- 24 chart records
- 1 digitized image (1024 data at computer output)
- 1 coincidence counter output

20-90-0177-0410

Table IIIb

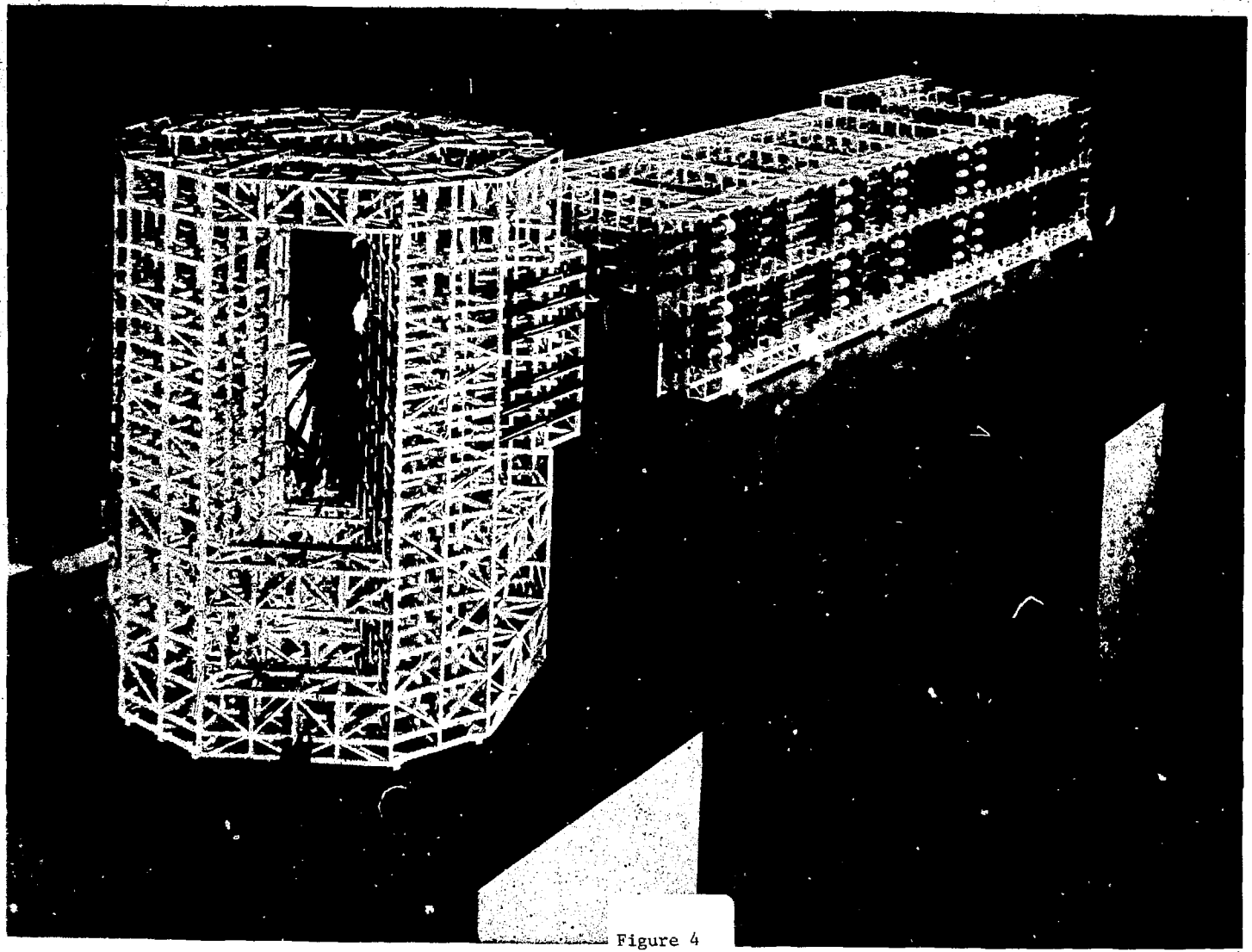

Figure 4

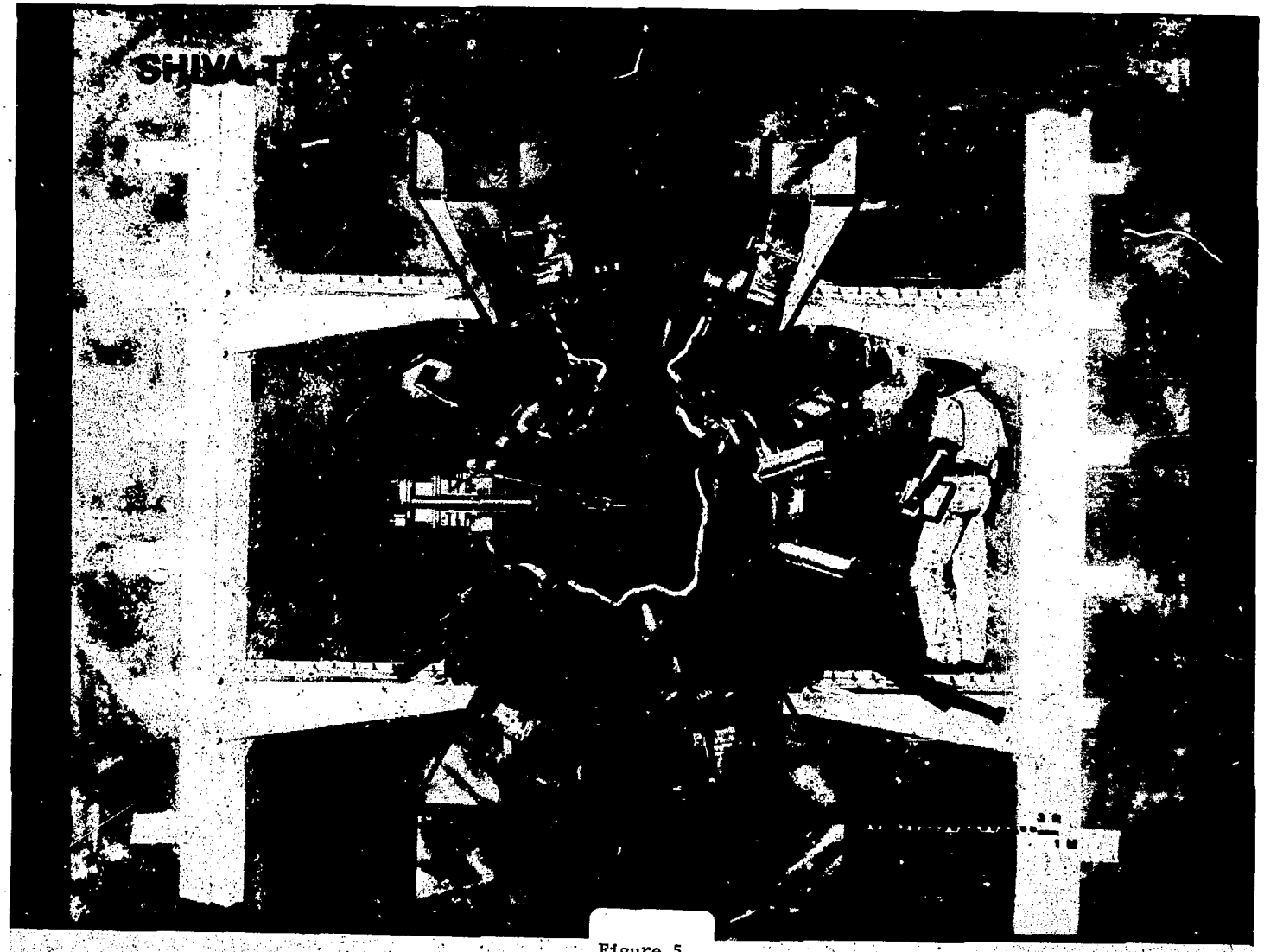

Figure 5

DIAGNOSTICS FOR INITIAL HYPERION TARGET EXPERIMENTS ON SHIVA

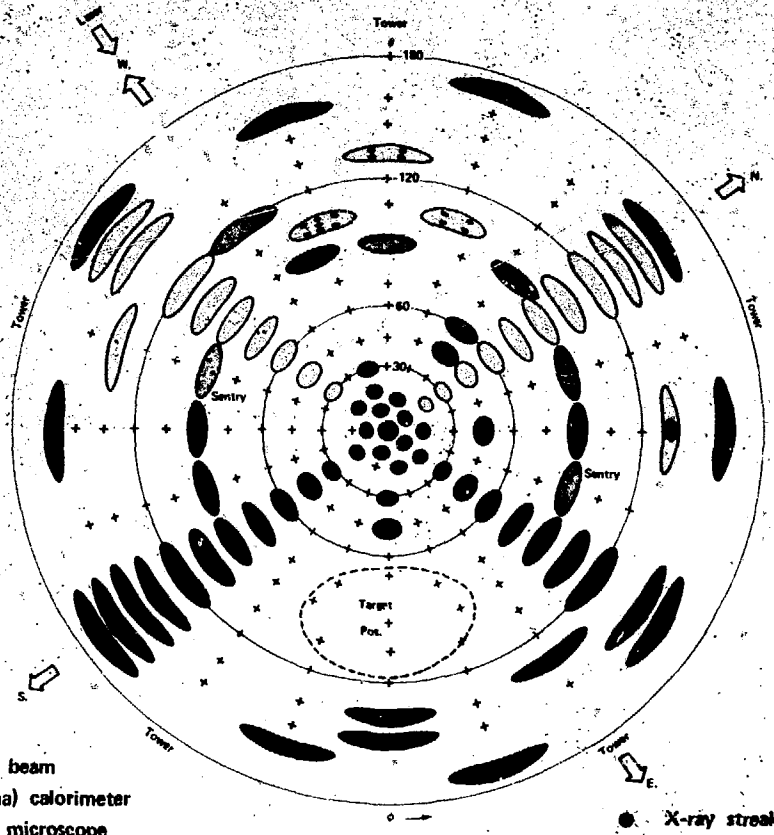

- ● Laser beam
- ○ (Plasma) calorimeter
- ● X-ray microscope
- ● Energy balance package
- ○ X-ray spectrometer

- ● $D\text{-}H^3_e$ proton detector

- ● X-ray streak camera
- ● Target viewers
- ● α-spectrometer
- ● Neutron detector

3/77

Figure 6

SHIVA COMPUTER SYSTEM

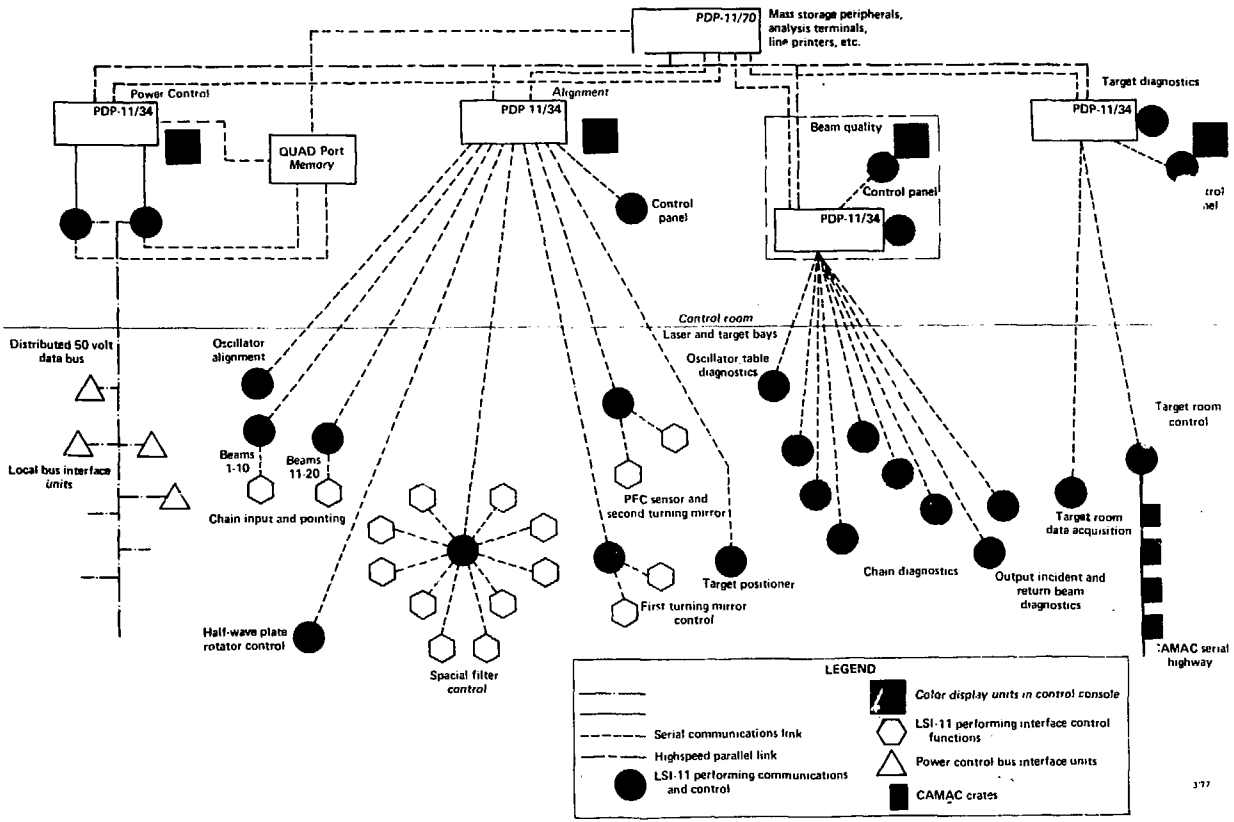

Figure 7

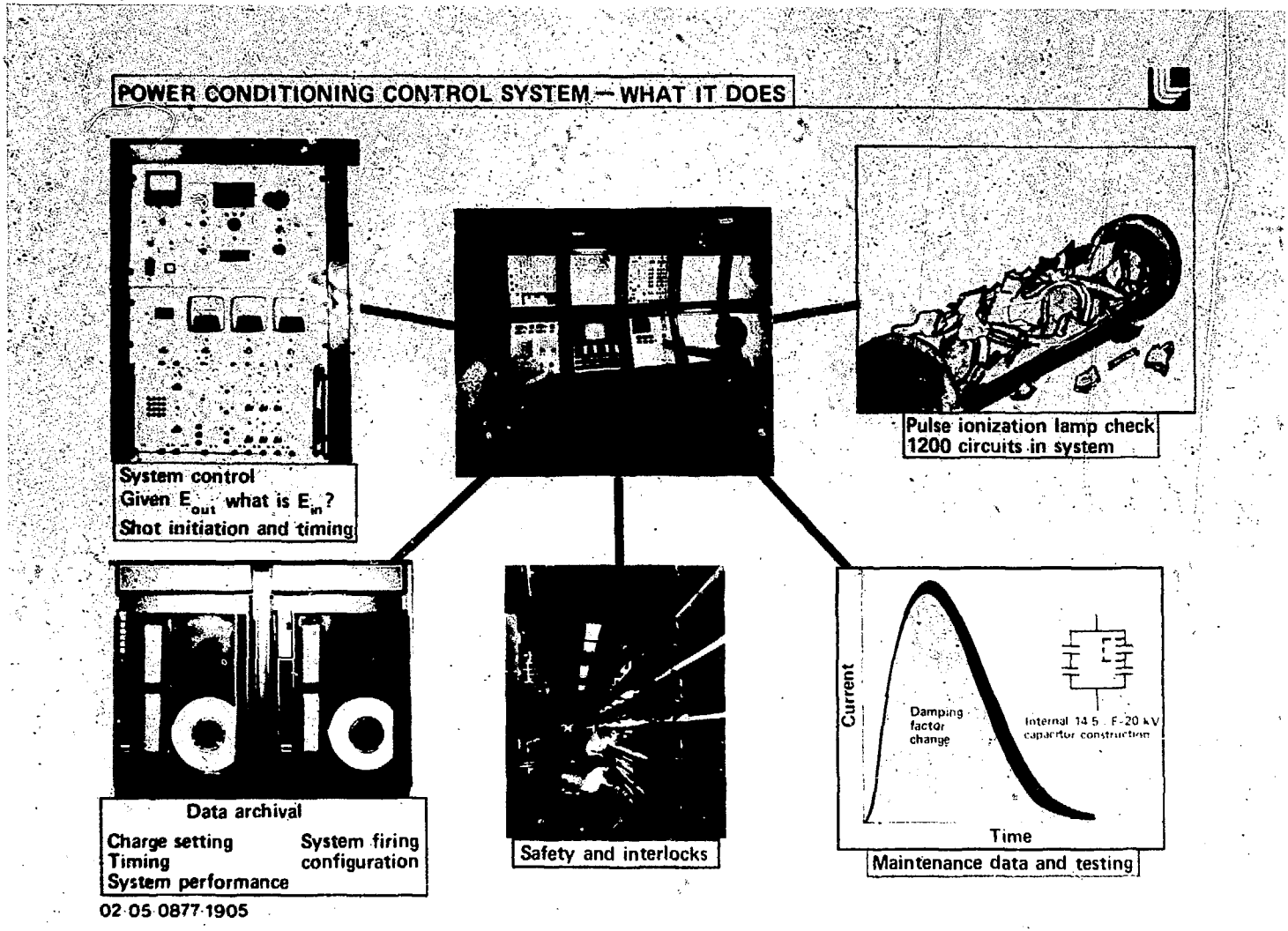
POWER CONDITIONING CONTROL SYSTEM — WHAT IT DOES
System control
Given E_{out} what is E_{in}?
Shot initiation and timing
Pulse ionization lamp check
1200 circuits in system
Data archival
Charge setting
Timing
System performance
System firing configuration
Safety and interlocks
Current
Damping factor change
Internal 14.5 F-20 kV capacitor construction
Time
Maintenance data and testing
02-05-0877-1905

Figure 8a

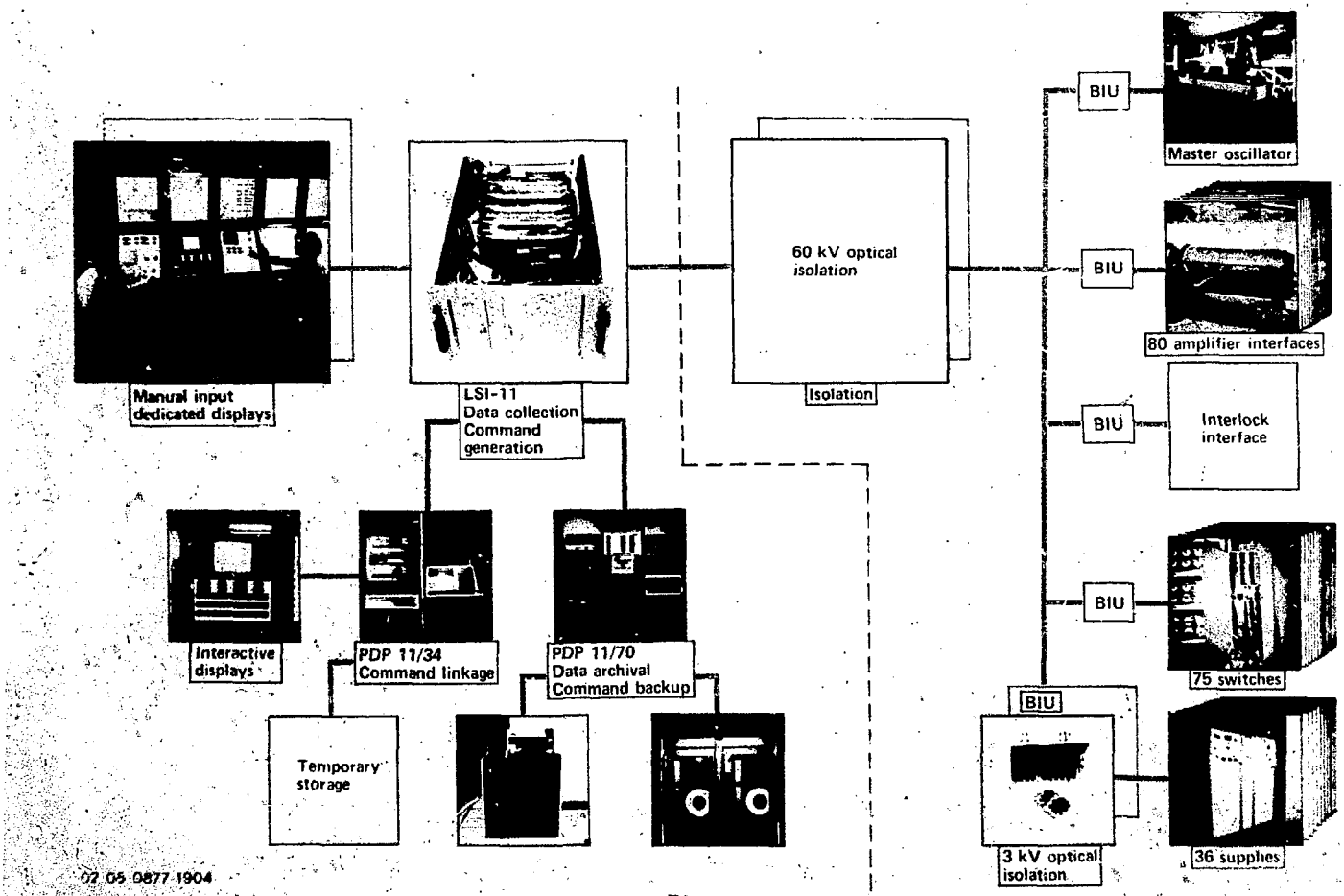
Manual input
dedicated displays
LSI-11
Data collection
Command
generation
60 kV optical
isolation
Isolation
BIU
Master oscillator
BIU
80 amplifier interfaces
BIU
Interlock
interface
BIU
75 switches
BIU
3 kV optical
isolation
36 supplies
Interactive
displays
PDP 11/34
Command linkage
PDP 11/70
Data archival
Command backup
Temporary
storage
02 05 0877 1904

Figure 8b

BEAM DIAGNOSTICS PRIMARY SENSOR AND DATA ACQUISITION STATIONS

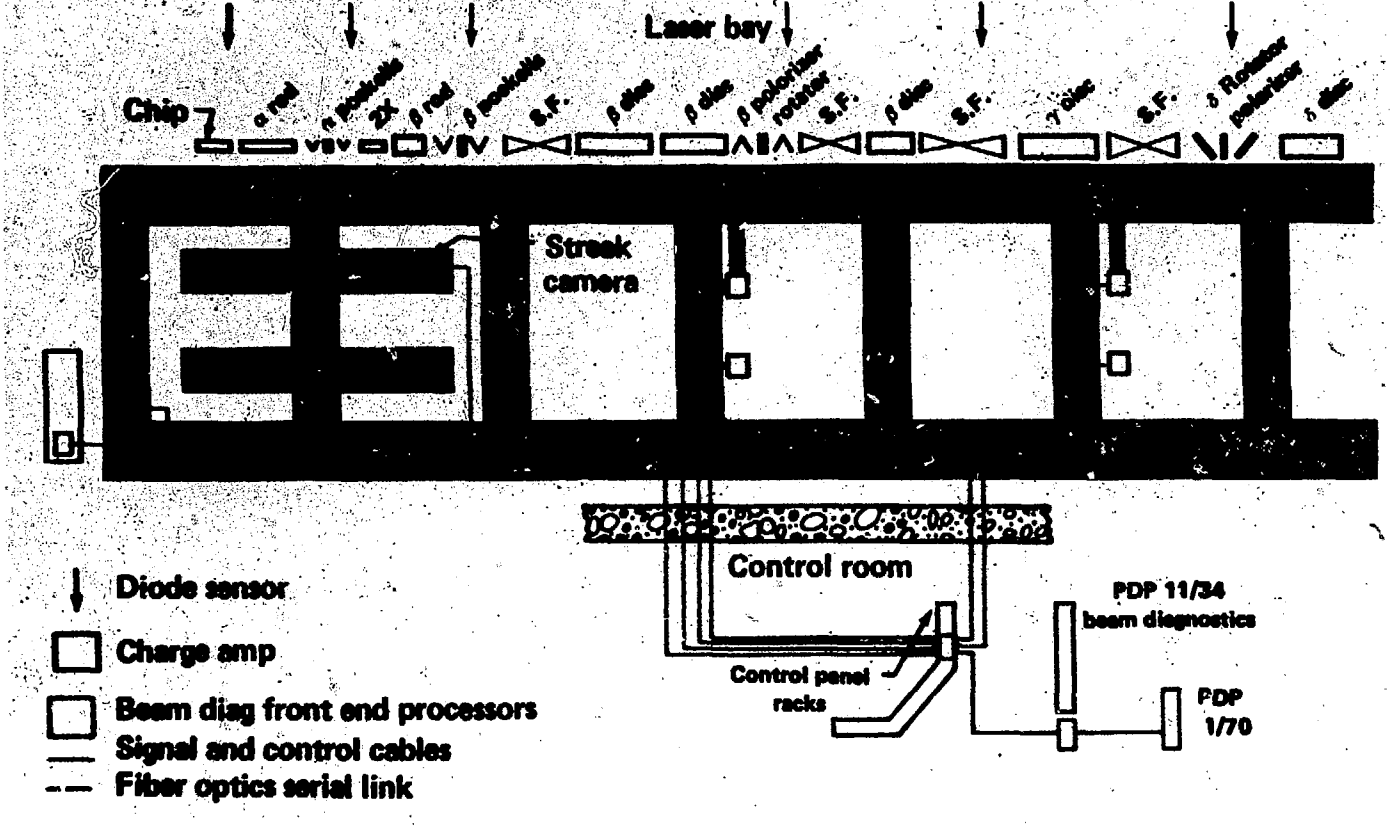

Figure 9

SHIVA INCIDENT BEAM DIAGNOSTICS PACKAGE

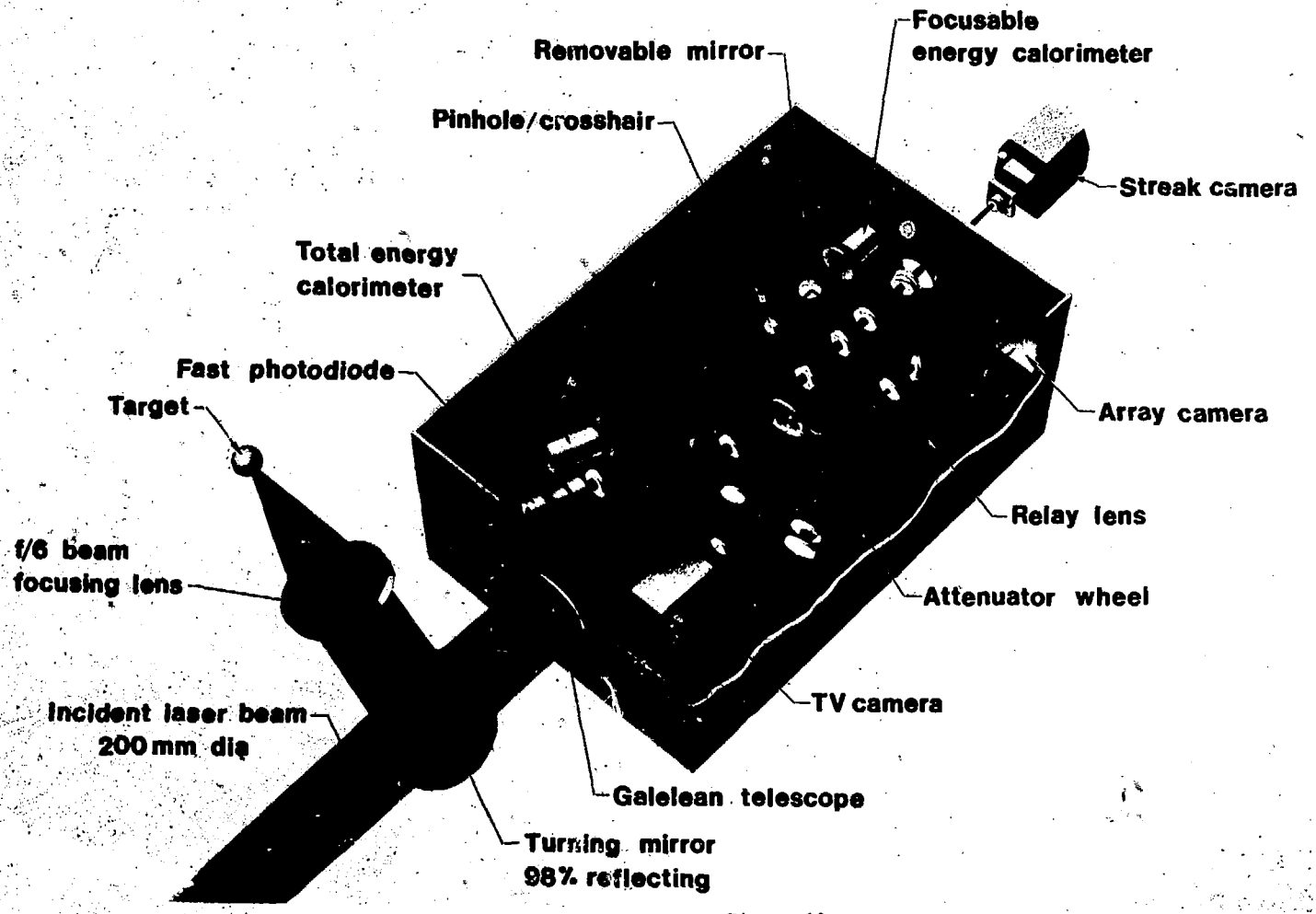

Figure 10

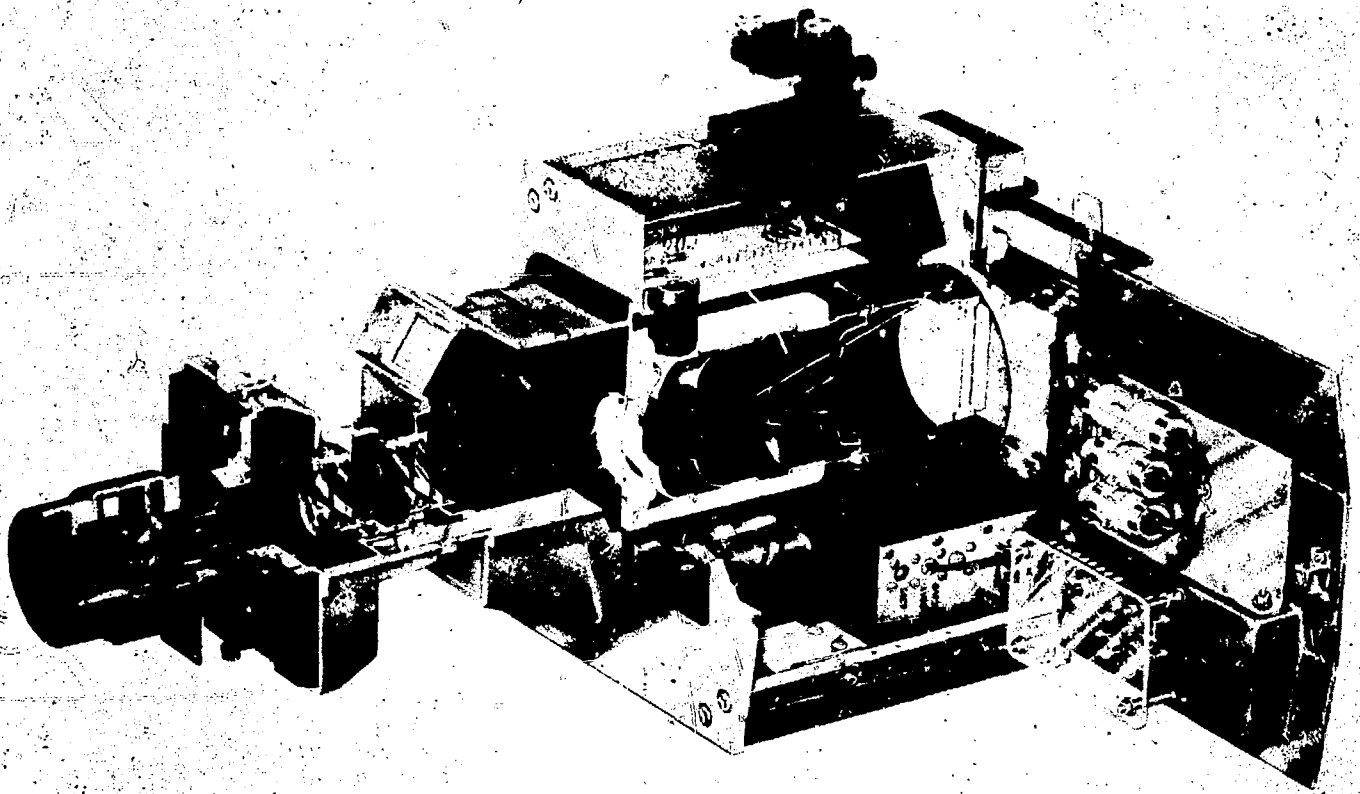

OPTICAL STREAK CAMERA

Figure 11

ARGUS LASER SYSTEM, NORTH ARM, TYPICAL BEAM PERFORMANCE DATA AT I.5 TW

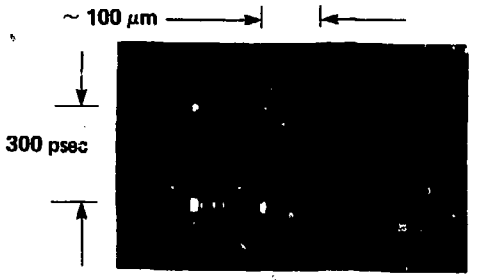

a. Equivalent plane streak

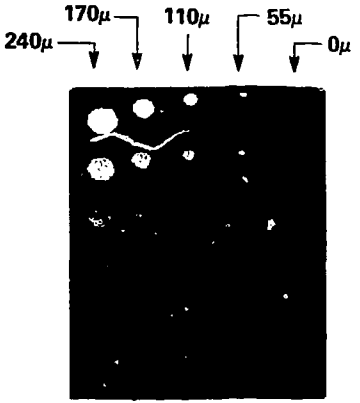

b. Equivalent plane profile

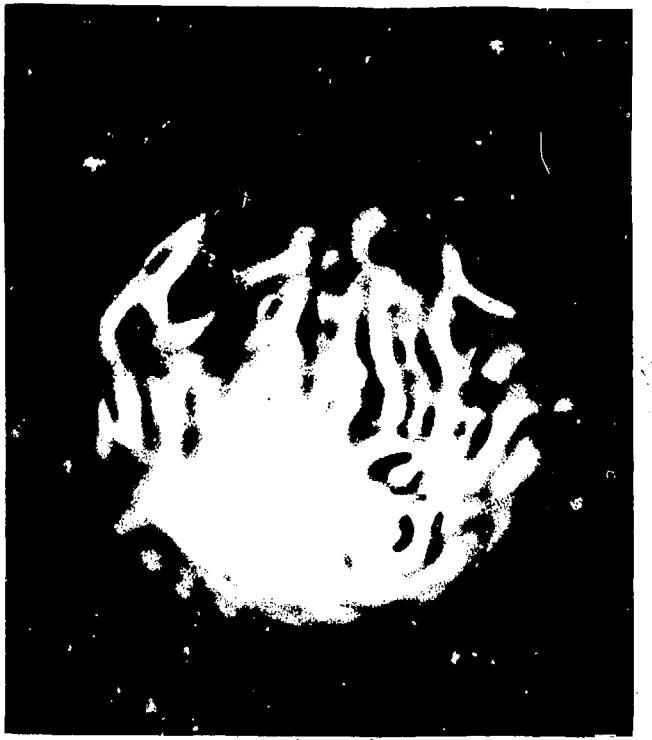

c. Near field profile

Note 17 cm to be diameter of beam picture on plate.

10/76

Figure 12

ARGUS NORTH BEAM – TARGET PLANE ENERGY DISTRIBUTION

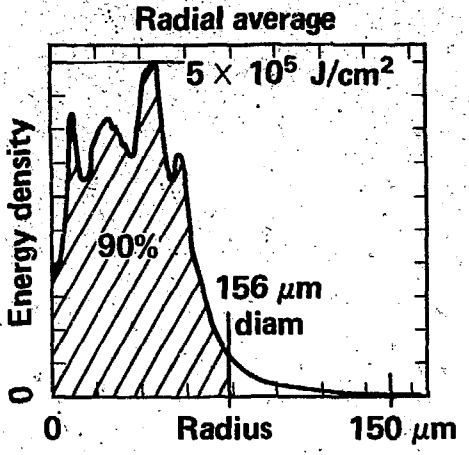

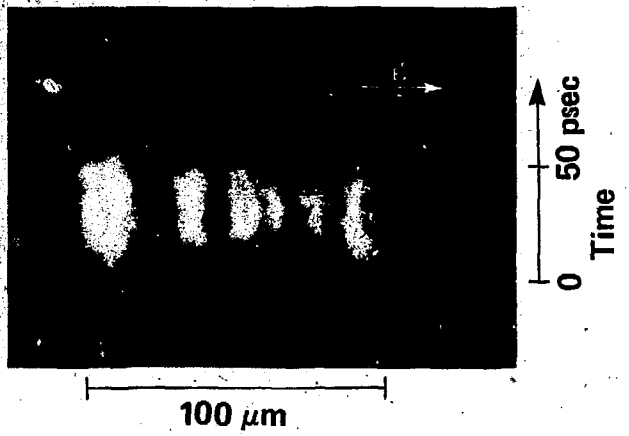

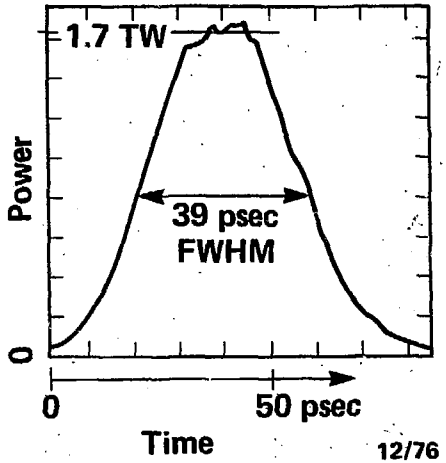

12/76

Figure 13

RETURN BEAM DIAGNOSTICS PACKAGE

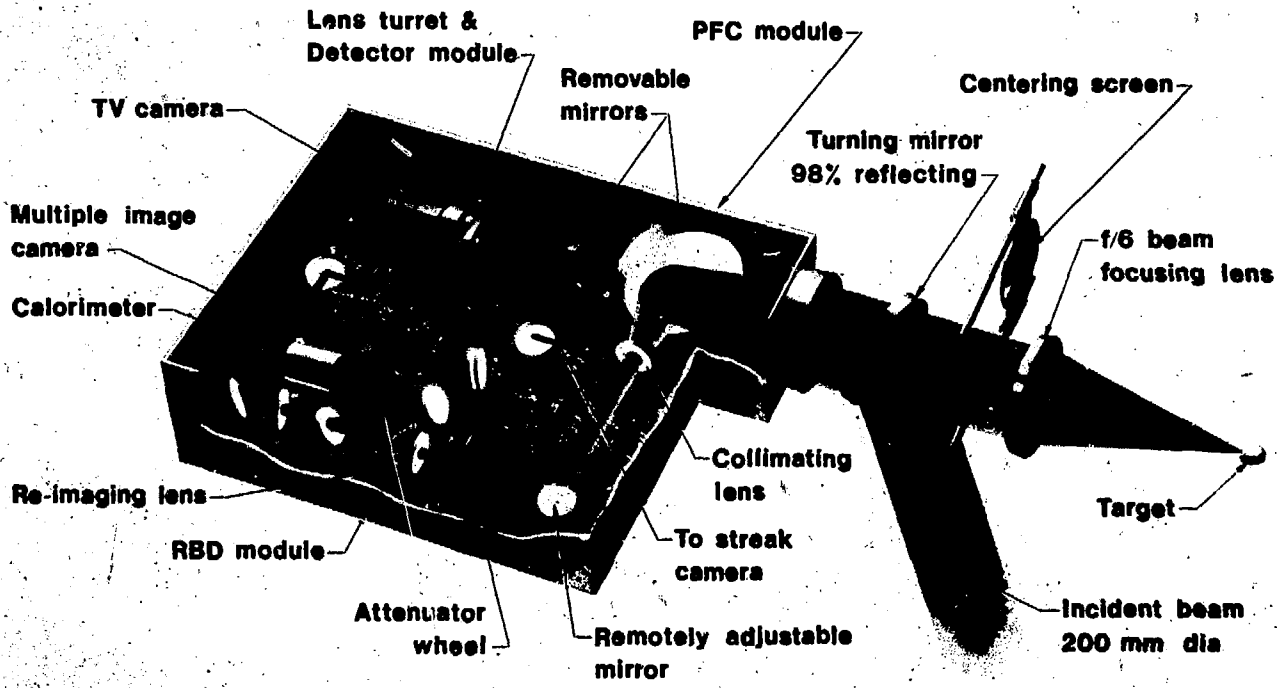

Figure 14

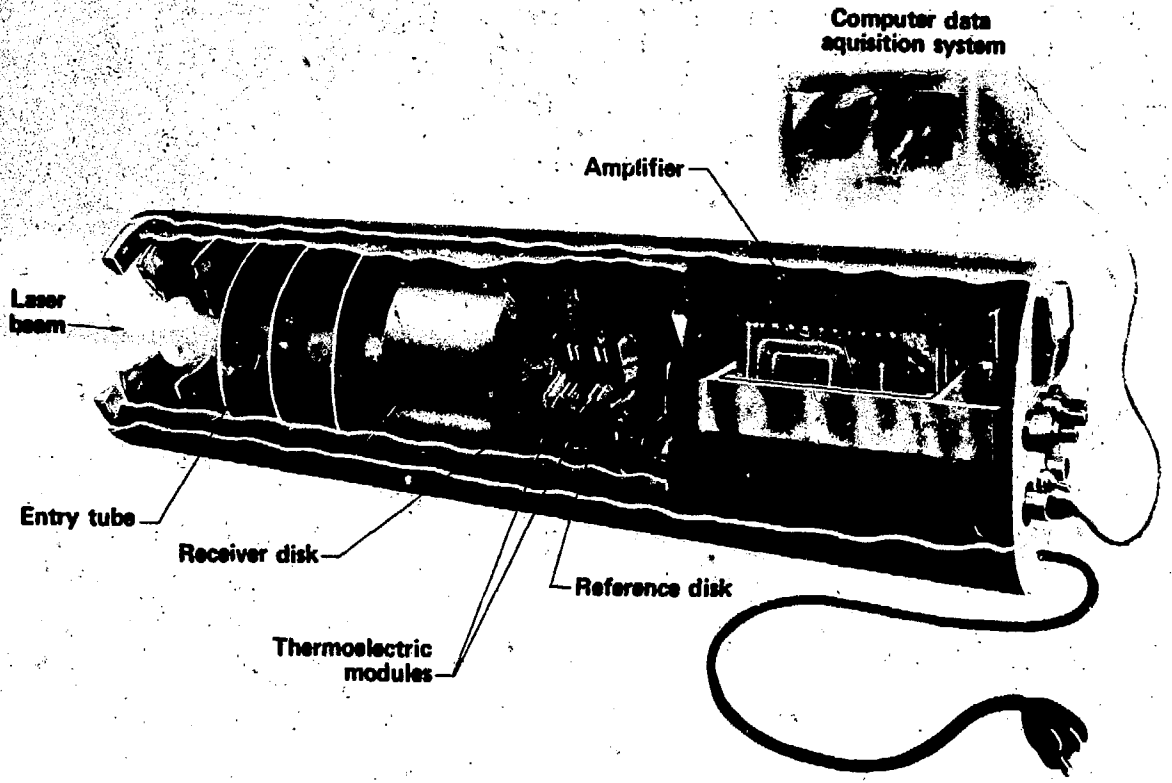
Computer data
aquisition system
Amplifier
Laser
beam
Entry tube
Receiver disk
Reference disk
Thermoelectric
modules

Figure 15

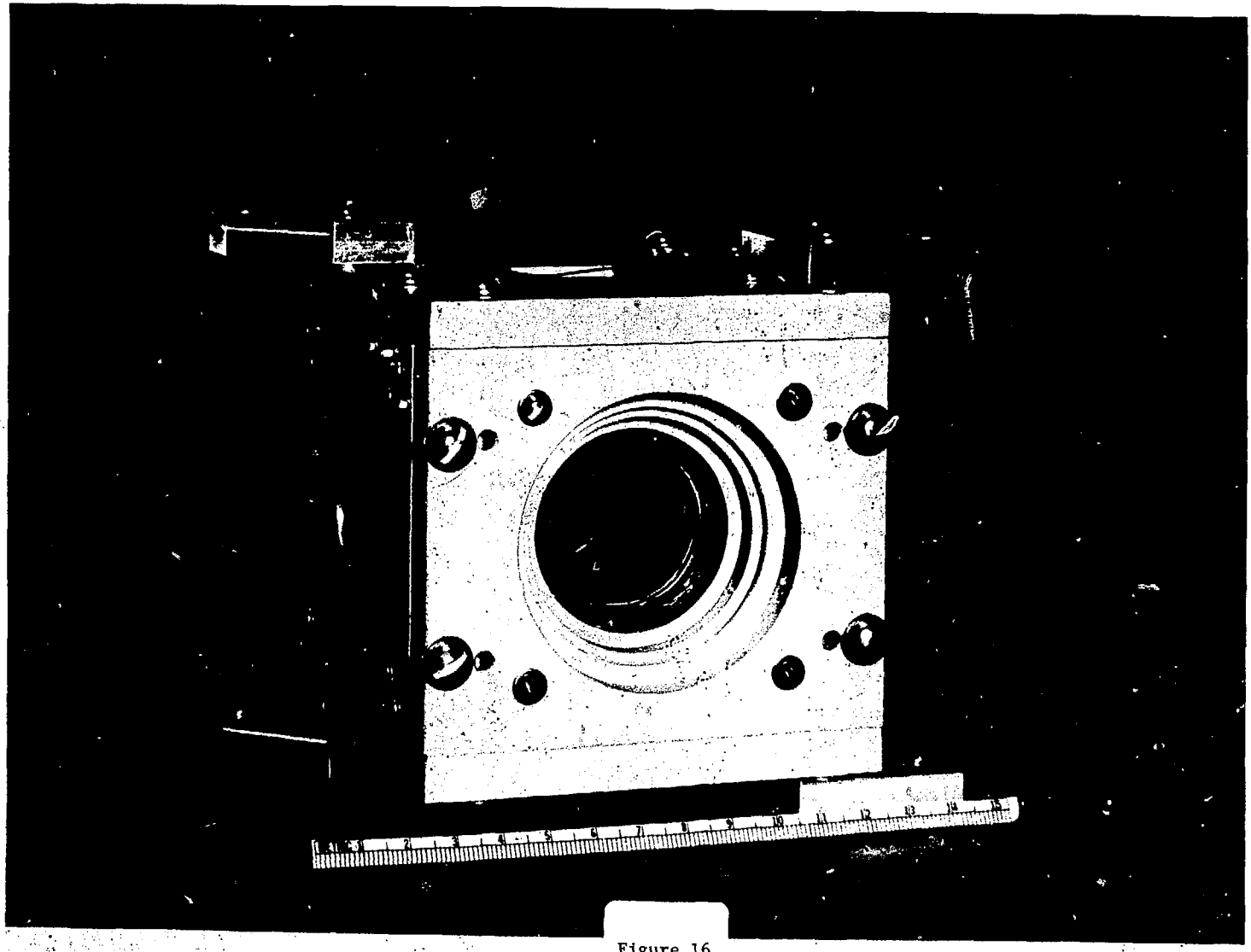

Figure 16

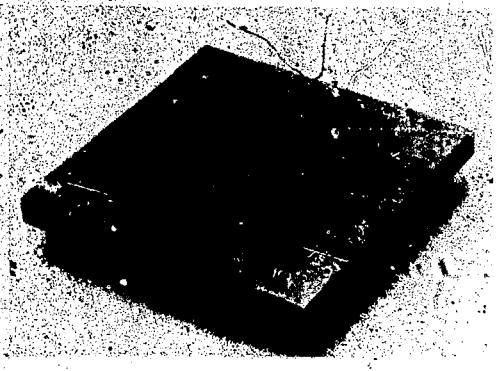

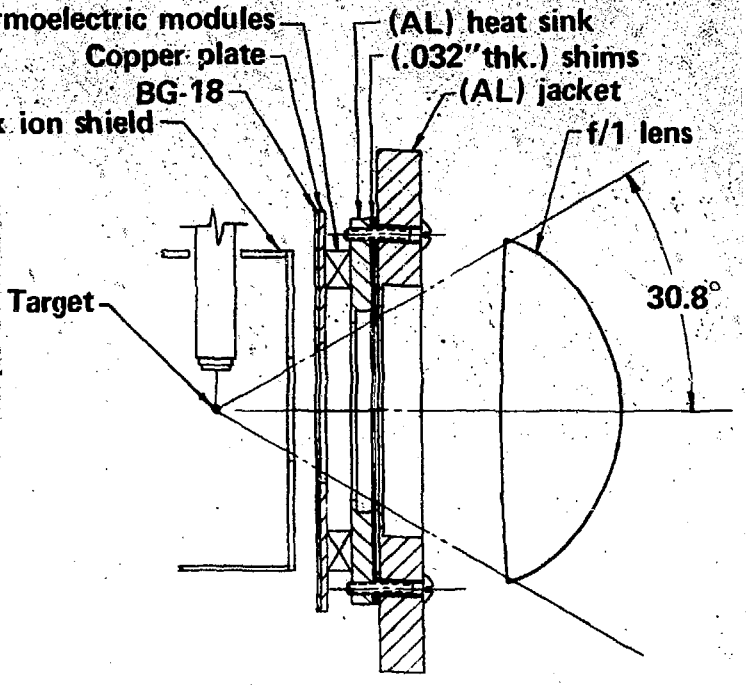
Thermoelectric modules
Copper plate
BG-18
Pyrex ion shield
(AL) heat sink
(.032"thk.) shims
(AL) jacket
f/1 lens
Target
30.8°

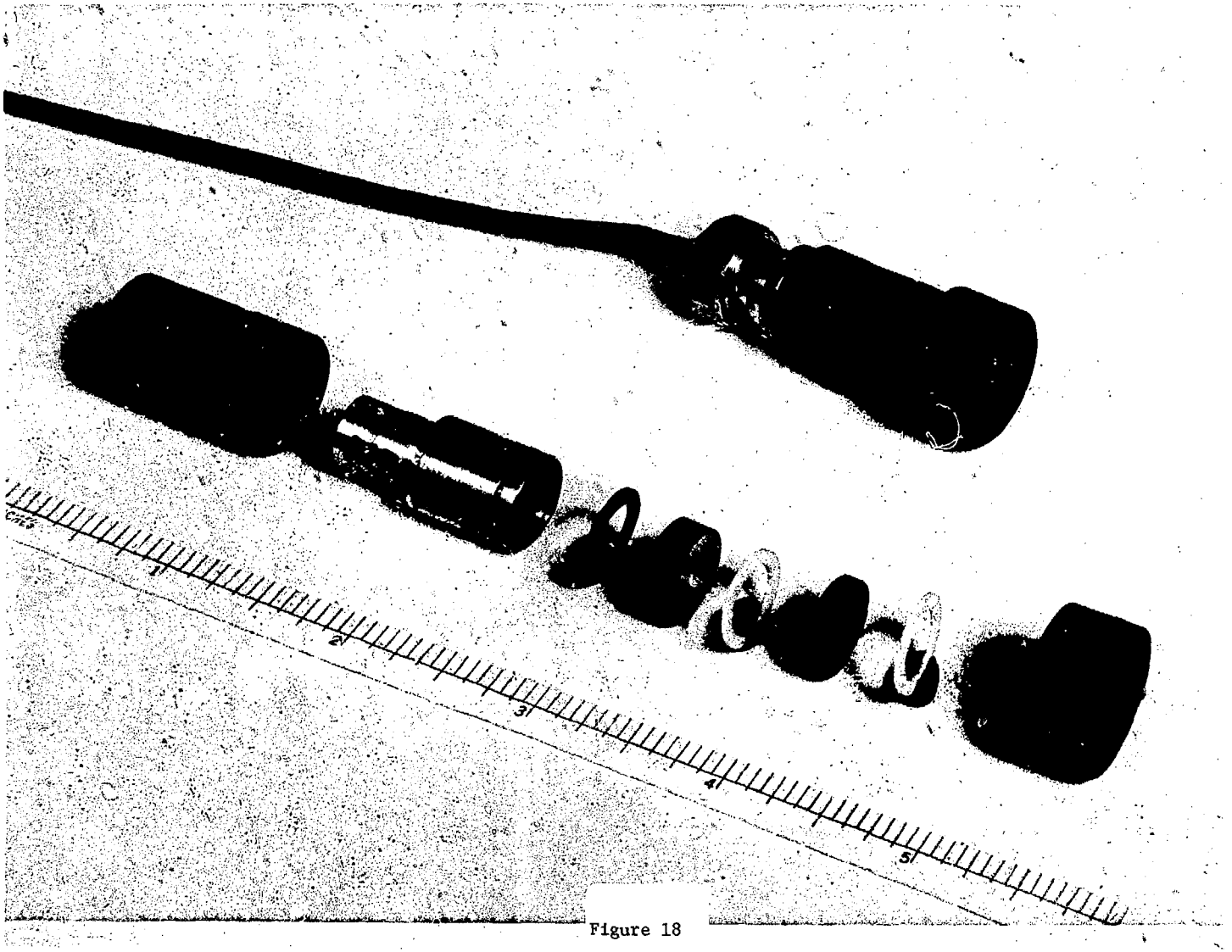

Figure 18

MINIATURE 1.06 μm CALORIMETER

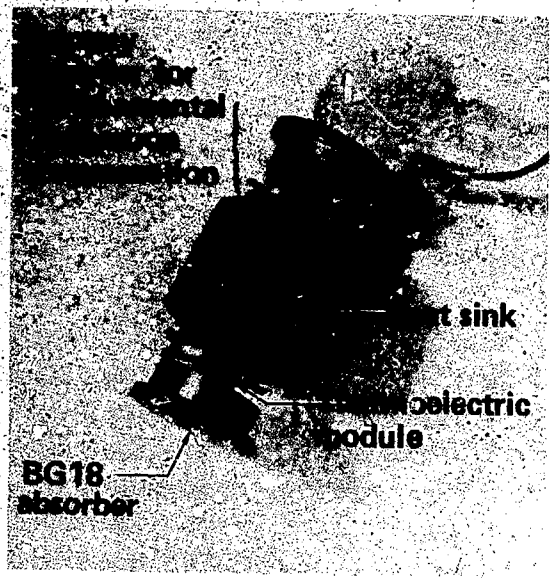

Detector

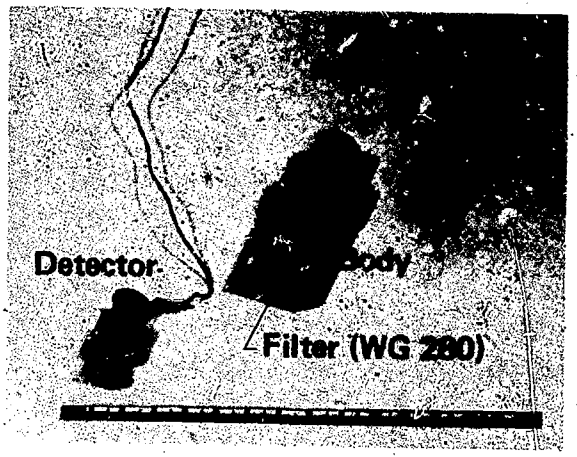

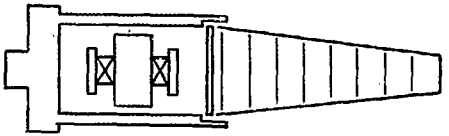

Assembly

20-10-0877-1687

Figure 19

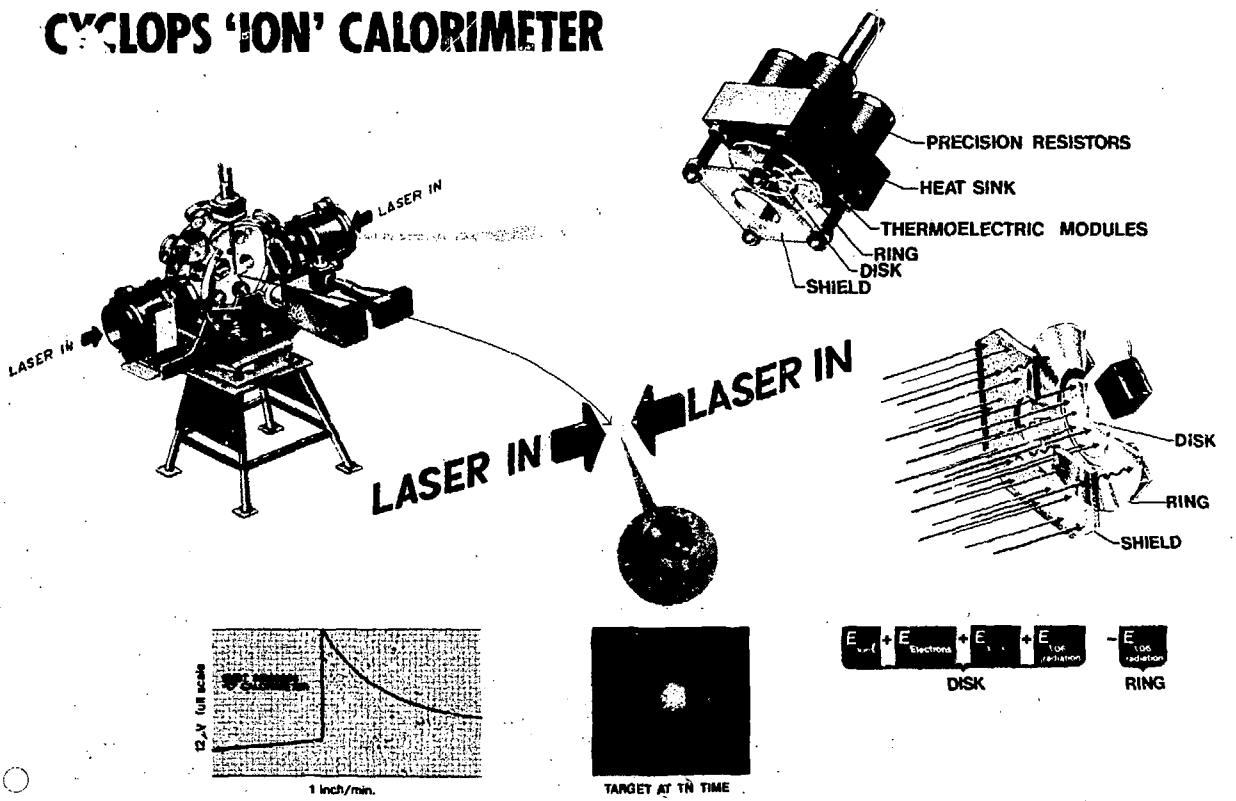
CYCLOPS 'ION' CALORIMETER
PRECISION RESISTORS
HEAT SINK
THERMOELECTRIC MODULES
RING
DISK
SHIELD
LASER IN
LASER IN
LASER IN
LASER IN
DISK
RING
SHIELD
12 μV full scale
1 inch/min.
TARGET AT TN TIME
DISK
RING

Figure 20

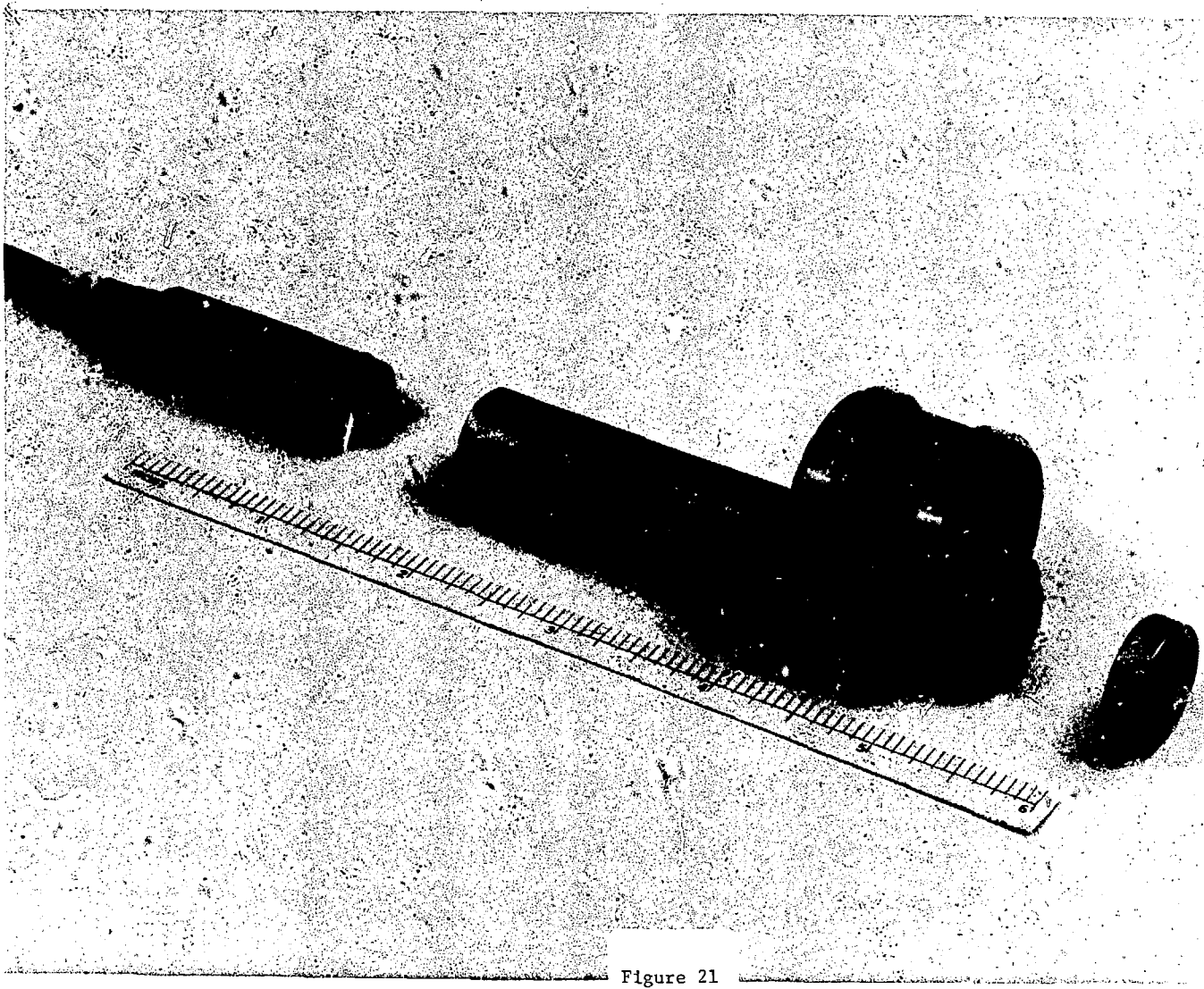

Figure 21

K-EDGE FILTER EXPERIMENT

(X-RAY SPECTRUM)

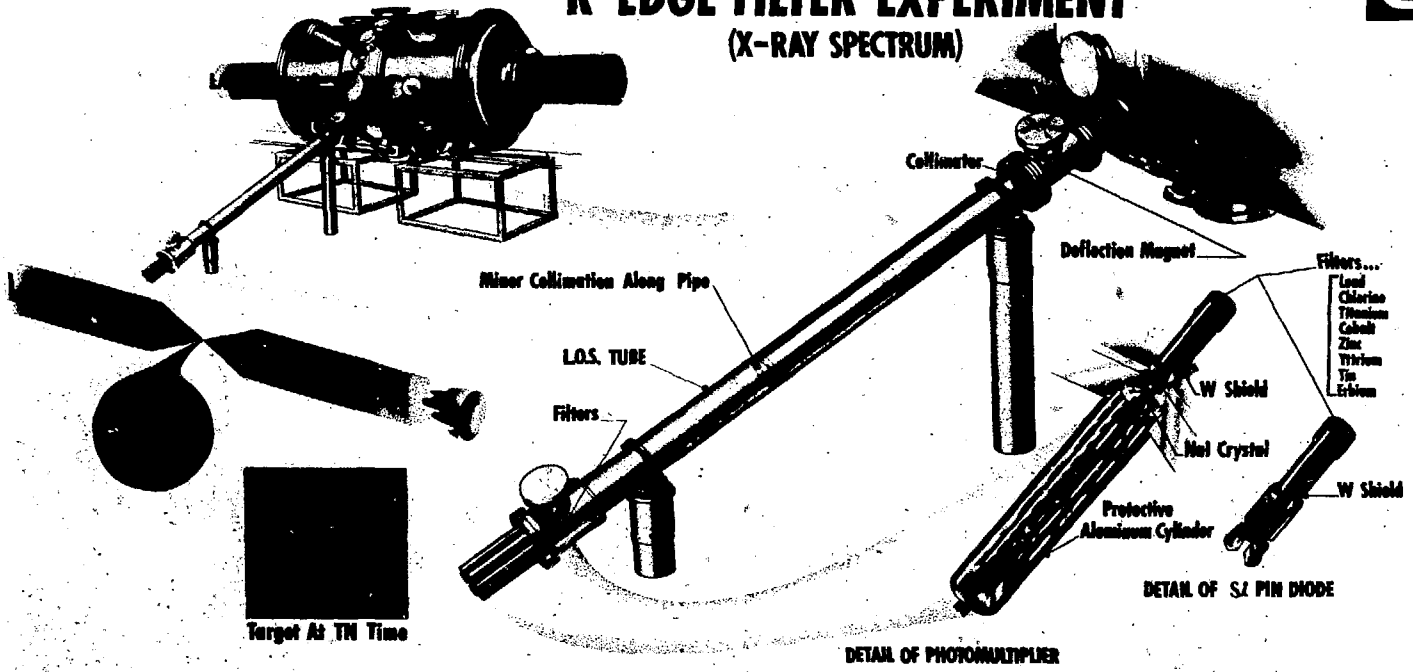

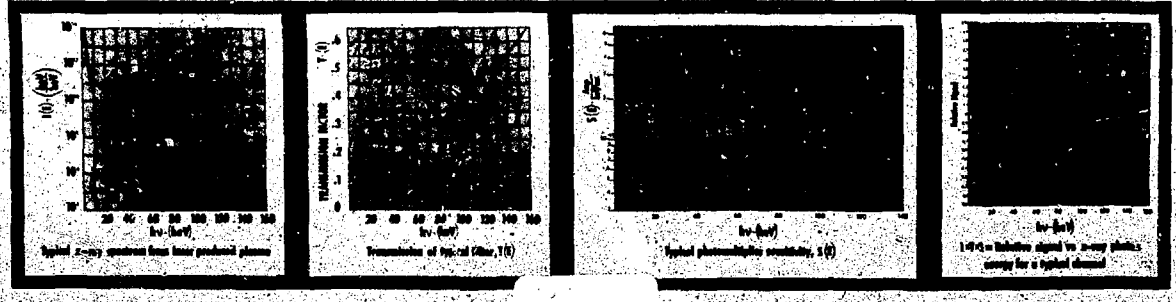

UNCLASSIFIED

Figure 22

TRIPLE CRYSTAL SPECTROGRAPH

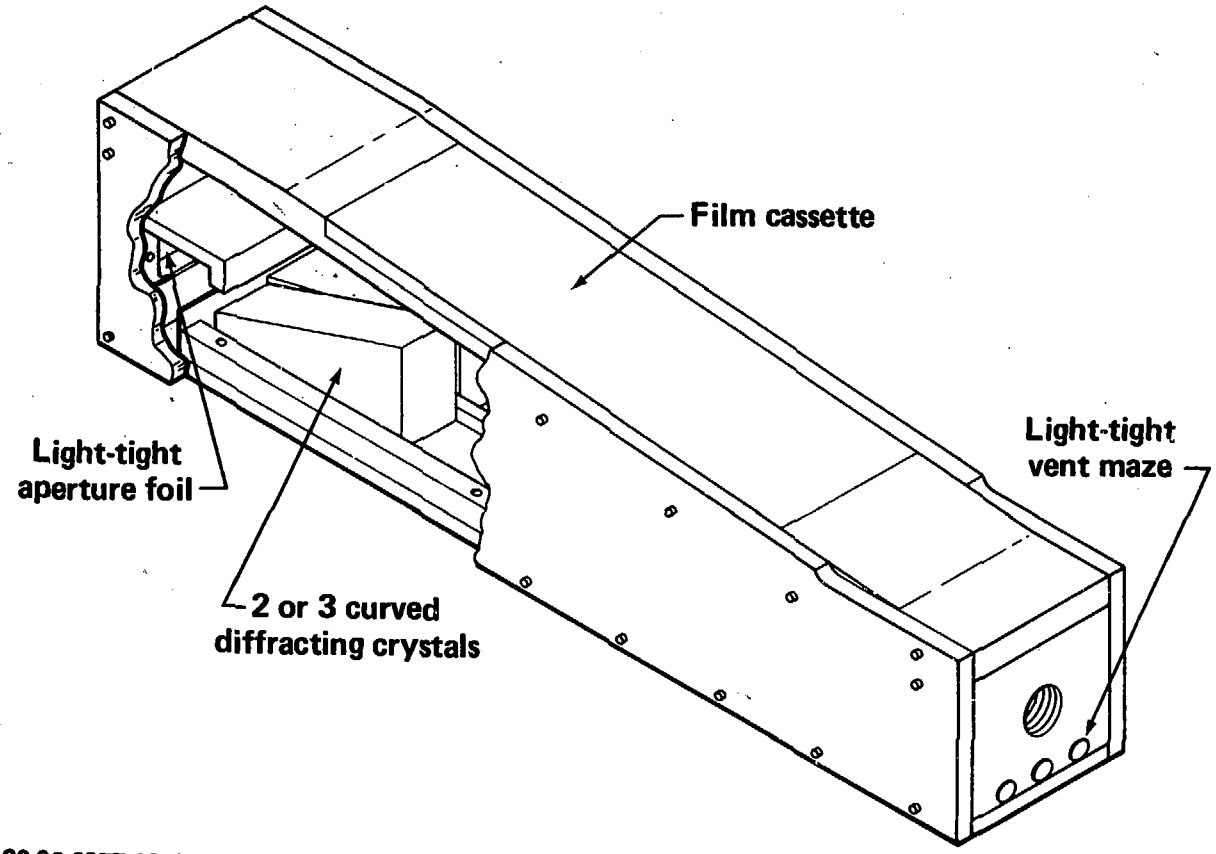

Figure 23

MEAN RESOLVING POWER AND ENERGY COVERAGE OF CRYSTALS, FOR $10° \leqslant \theta_B \leqslant 45°$

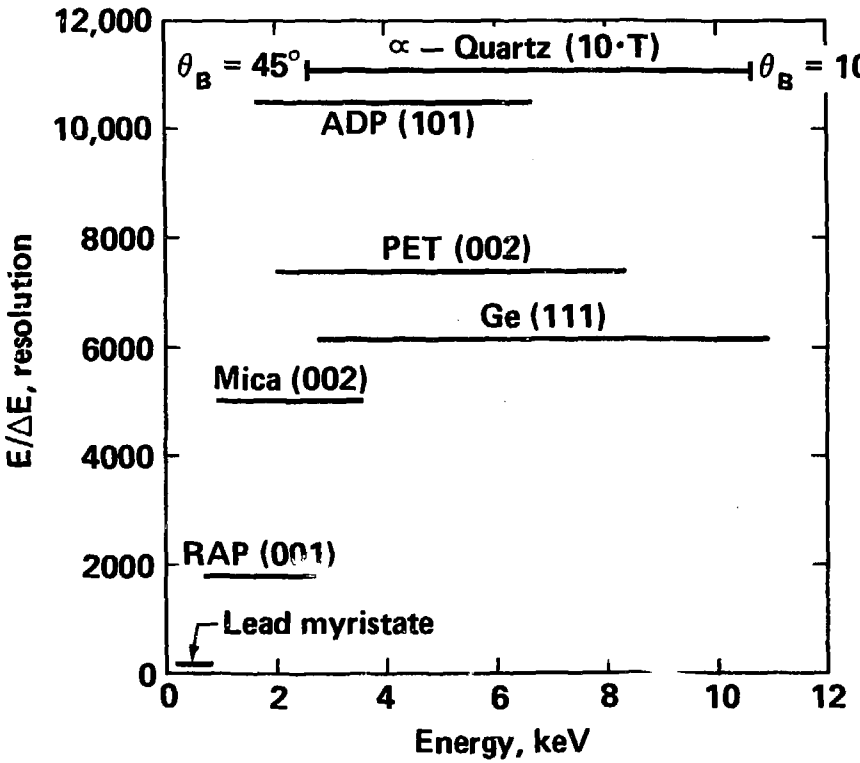

Note that reflecting power is usually sacrificed for high resolution, E/ΔE

20-90-0877-1633

Figure 24

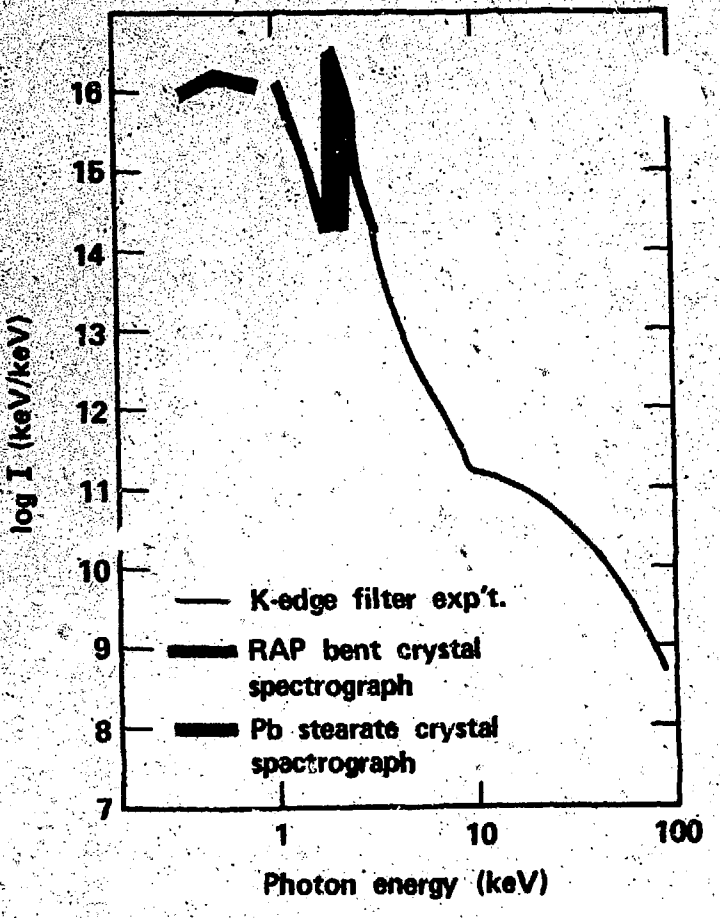
16
15
14
13
12
11
10
9
8
7
log I (keV/keV)
K-edge filter exp't.
RAP bent crystal spectrograph
Pb stearate crystal spectrograph
1
10
100
Photon energy (keV)

Figure 25

LASER PLASMA INTENSITY CHART

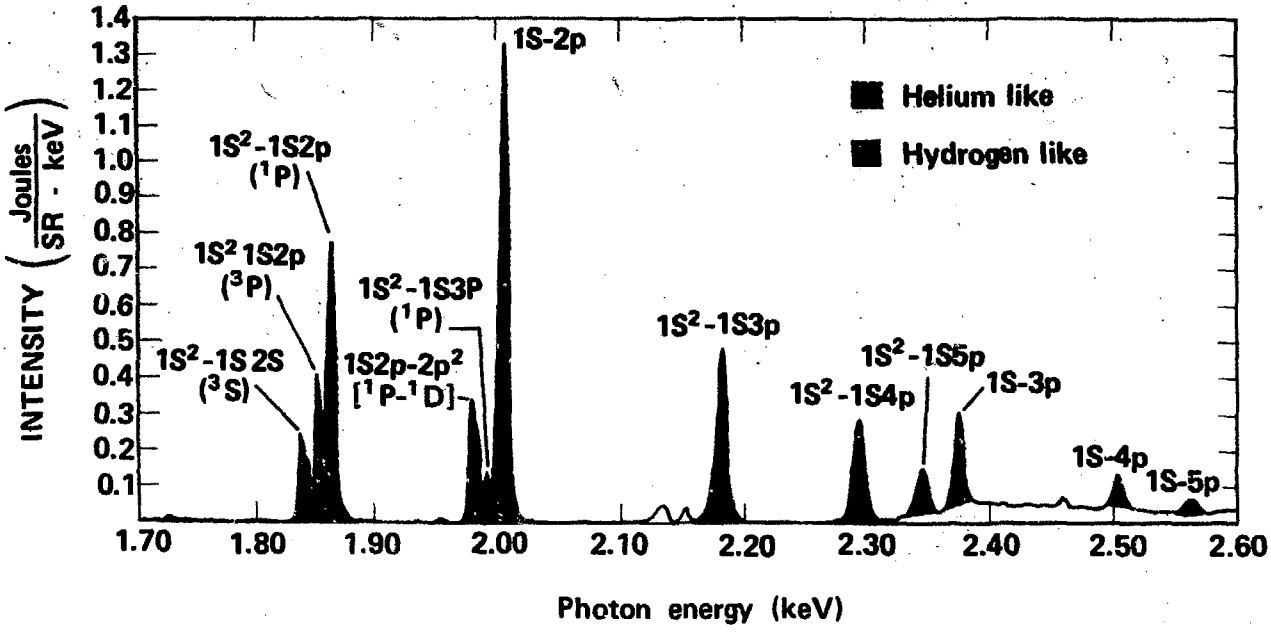

Figure 26

COMPOSITE X-RAY SPECTRUM, FROM FOUR INSTRUMENTS, FOR A GLASS MICROSPHERE TARGET (140 μm DIAMETER)IRRADIATED BY THE ARGUS LASER WITH A 535J, 187 ps GAUSSIAN PULSE

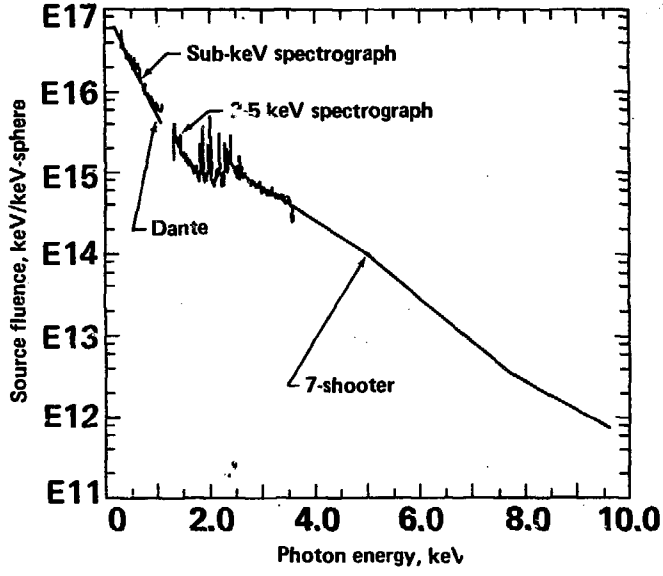

Instrument	Description	Coverage
Dante	Filter/reflector discrimination, fast XRD	0.2-1.1 keV in 3 chls
Sub-keV spectrograph	Lead myristate xtal diffraction, VUV film	0.32-1.0 keV, 10 eV resolution
2-5 keV spectrograph	RAP xtal diffraction, no-screen film	1.4-4.2 keV, 2-3 eV resolution
Seven shooter	Filter discrimination, PIN diode	2.5-3.0 keV in 6 chls

20-90-0777-1508

Figure 27

COMPRESSION SPECTROGRAPH

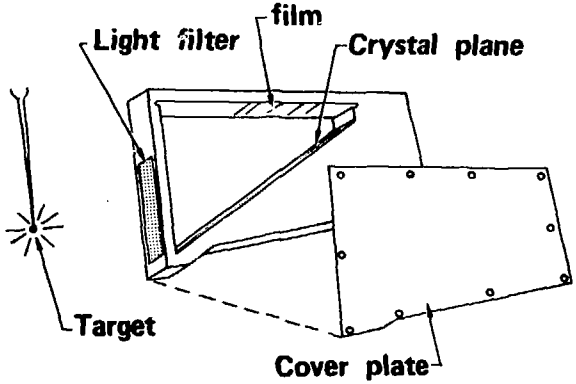

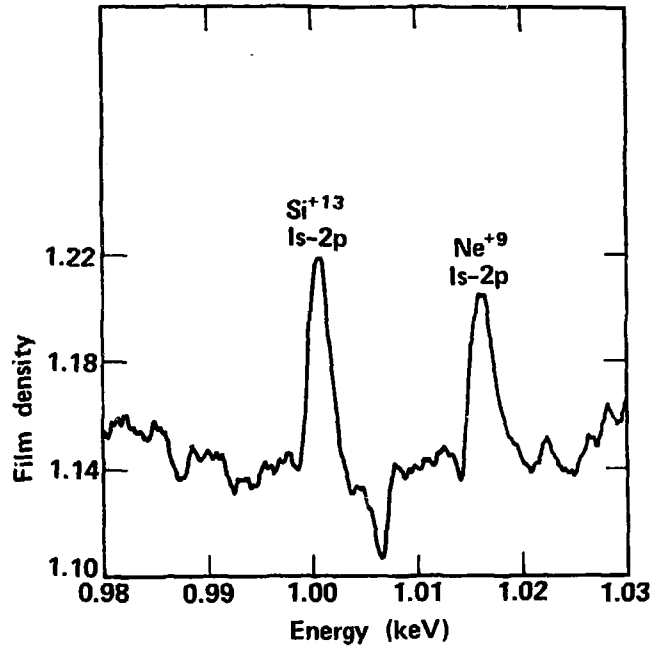

Detail of 1s-2p line of the hydrogen-like neon ion

11/76

Figure 28

SIMPLE 4-CHANNEL X-RAY MICROSCOPE

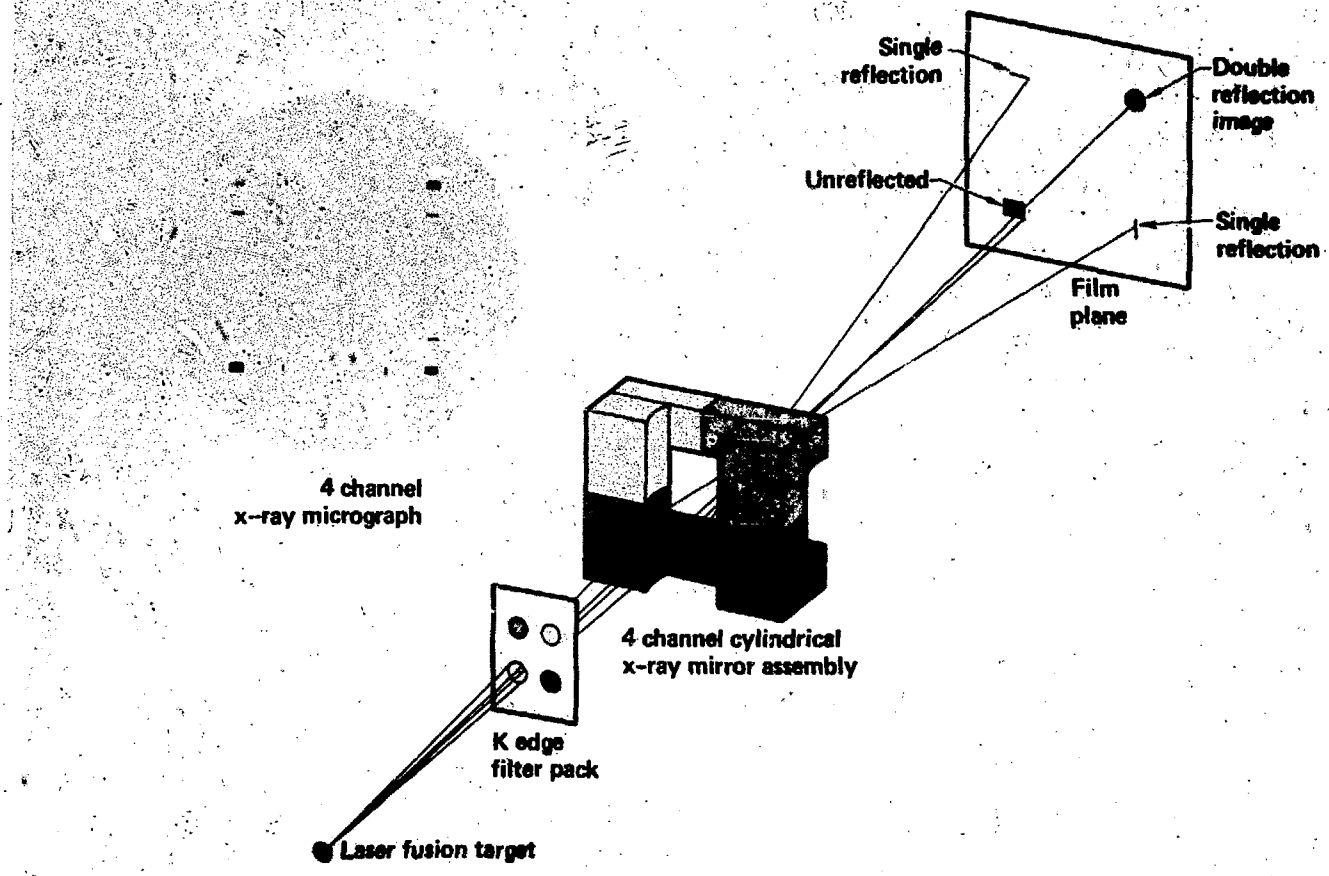

20-50-0877-1847

Figure 29

CARBON, QUARTZ, NICKEL AND GOLD X-RAY MICROSCOPE MIRRORS PROVIDE X-RAY IMAGING CAPABILITY BETWEEN 0.1 AND 10 keV

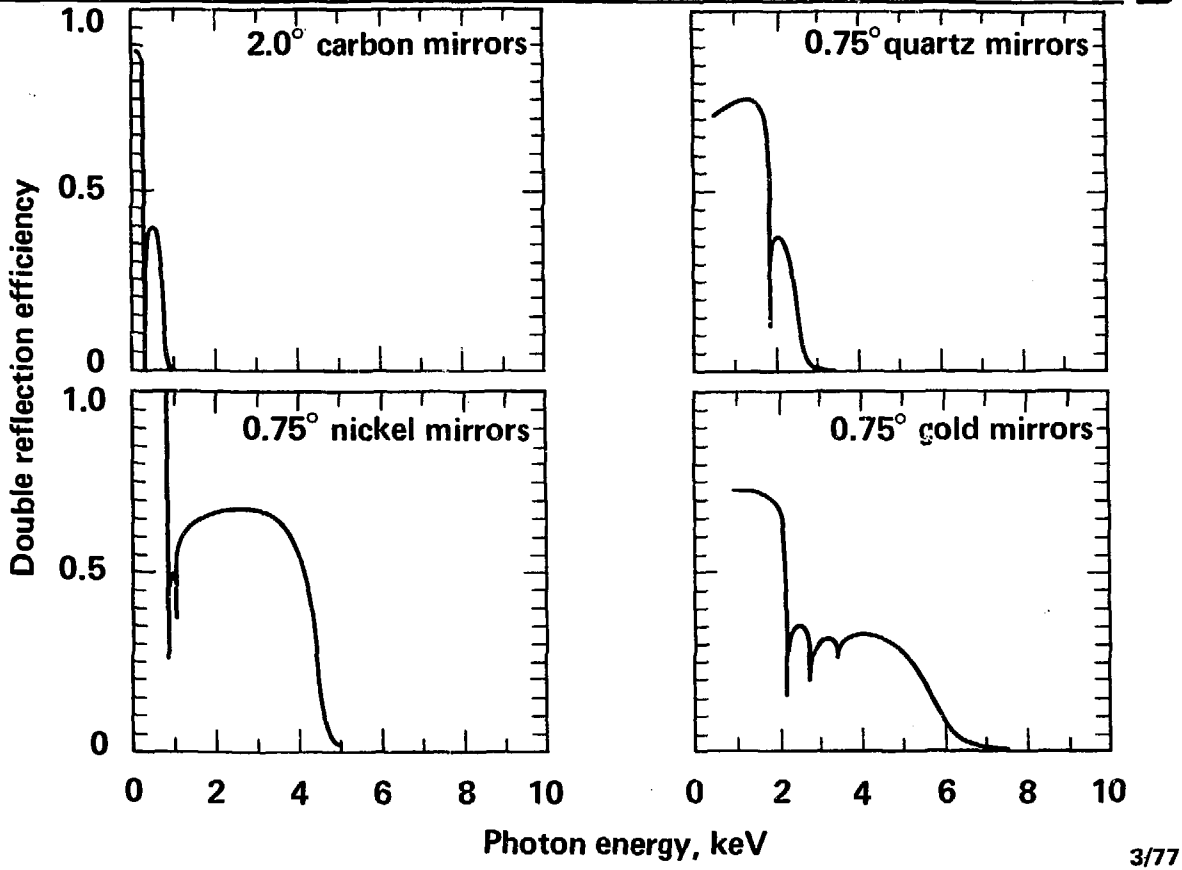

3/77

Figure 30

MULTICHANNEL X-RAY MICROSCOPE SPECTRAL ENERGY WINDOWS

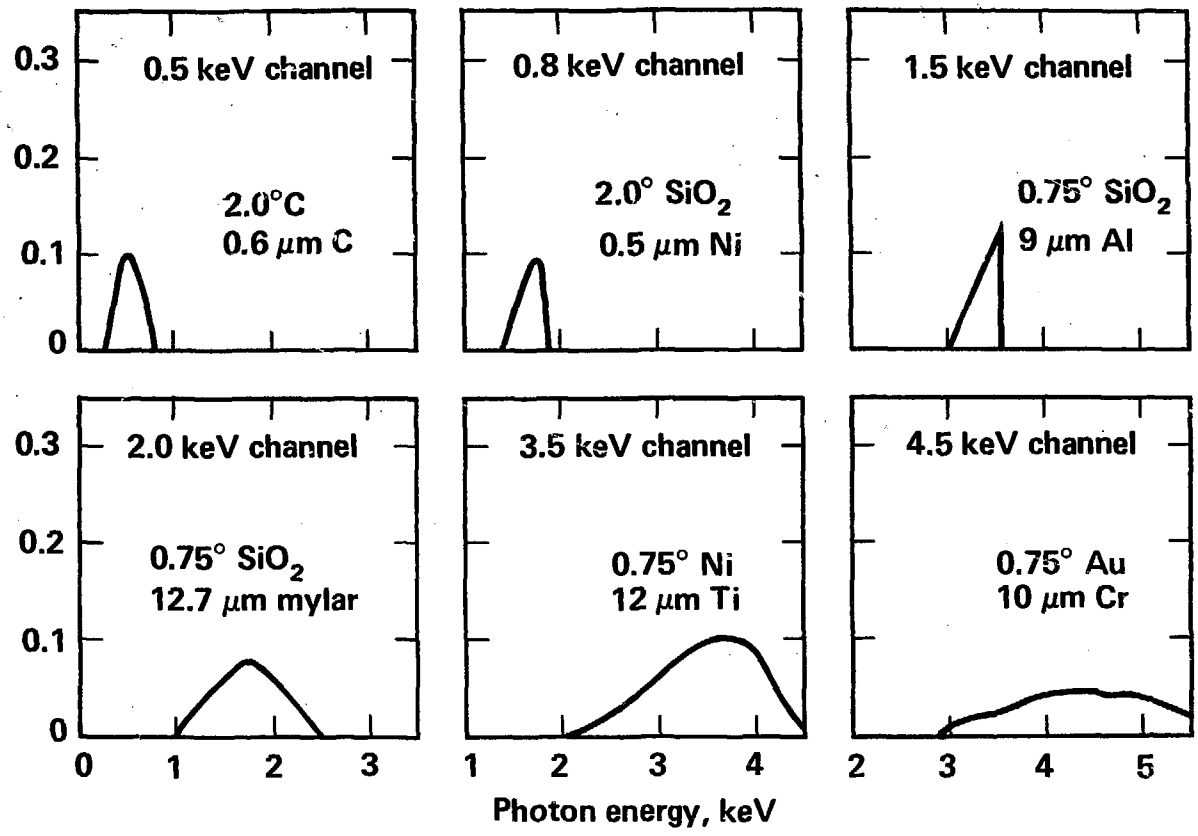

20-50-0877-1729

Figure 31

X-RAY MICROSCOPE

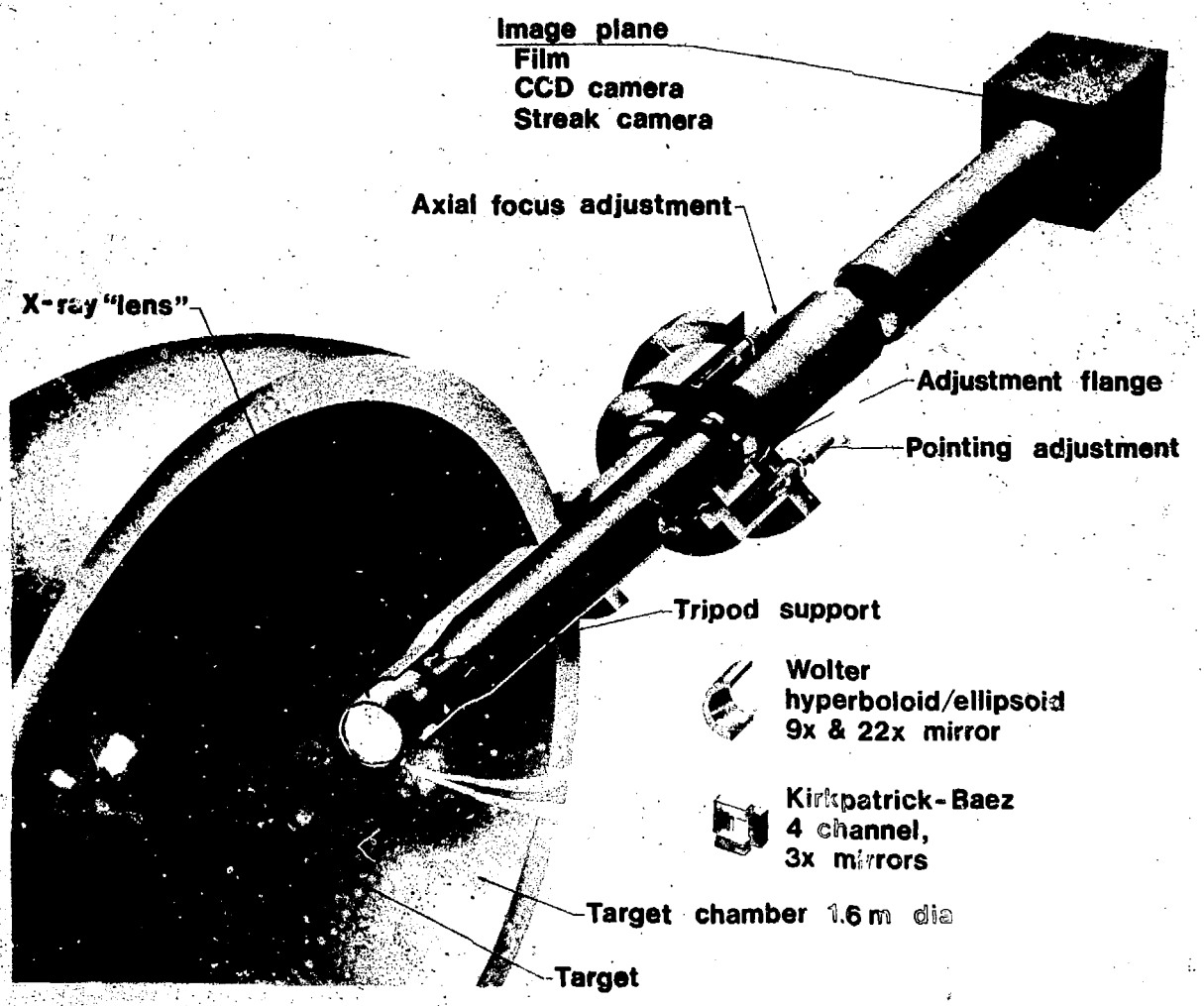

Figure 32

INCREASED INCIDENT POWER IMPROVES ABSORPTION AND COMPRESSION SYMMETRY WITH f/1 OPTICS

32 J–73 psec
75062405-1

63 J–48 psec
36080611-5-1

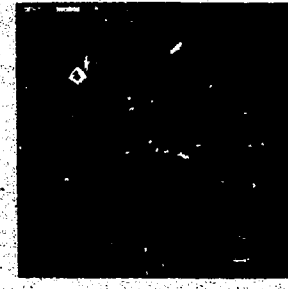

1.5 keV

JANUS – 0.4 TW

ARGUS – 2.0 TW

32 J–73 psec
75062405-4

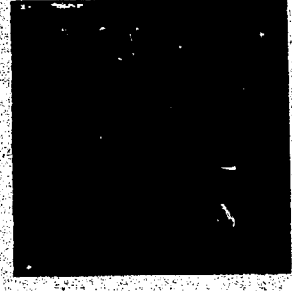

83 J–29 psec
36101203-5-4

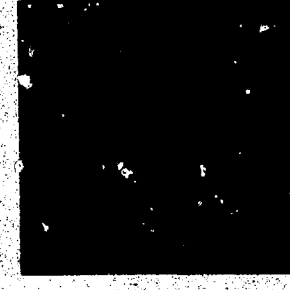

2.5 keV

11/76

Figure 33

WOLTER TYPE I X-RAY MICROSCOPE SCHEMATIC

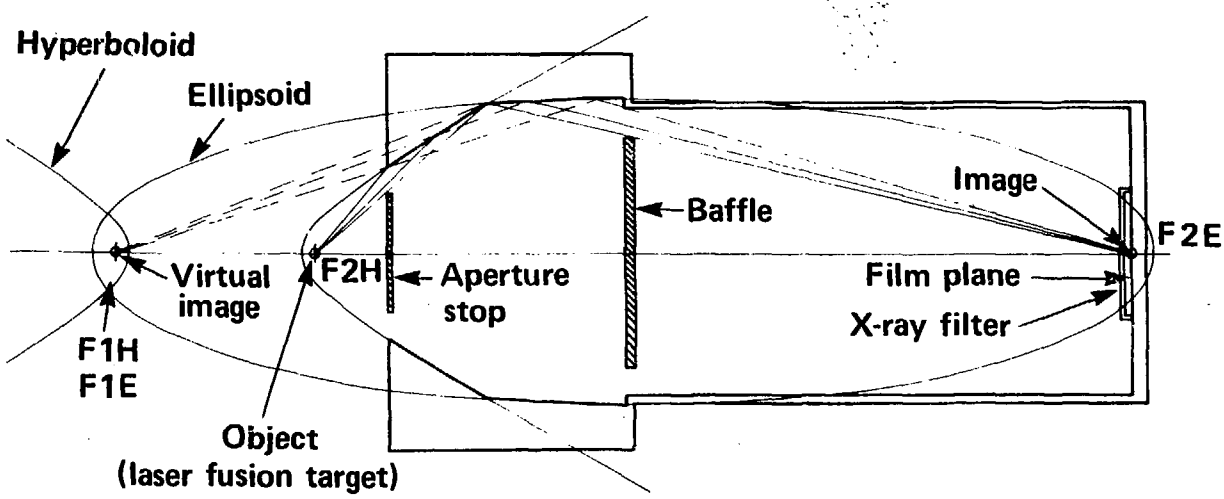

Figure 34

NUMERICALLY CONTROLLED CORRECTIONS IMPROVE THE SURFACE FIGURE OF DIAMOND TURNED AXISYMMETRIC X-RAY MICROSCOPES

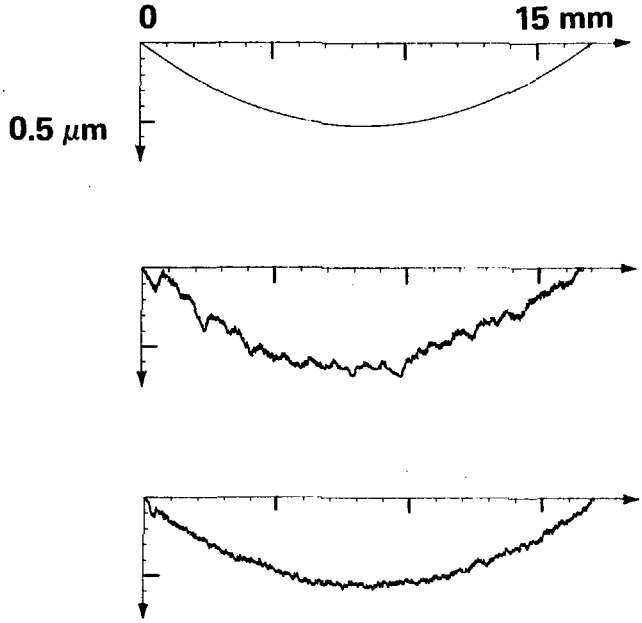

Figure 35

AXISYMMETRIC X-RAY MICROSCOPE RESOLUTION IMPROVES WITH MORE ACCURATE FIGURING OF THE HYPERBOLOID/ELLIPSOID REFLECTING SURFACES

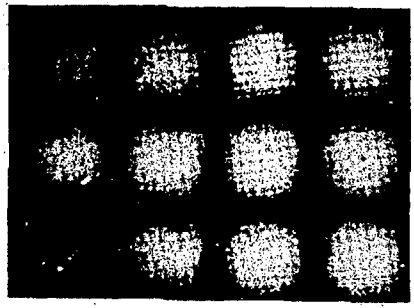

9X-30 ~8 μm resolution

Resolution micrographs

9X-2 ~4 μm resolution

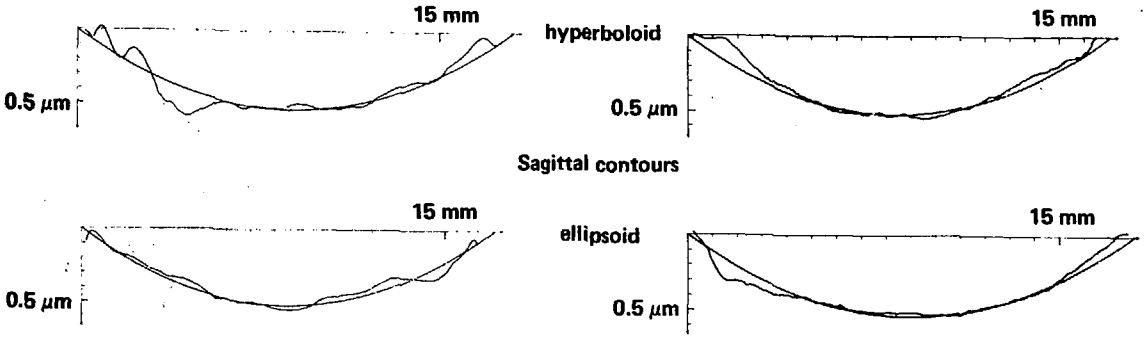

Figure 36

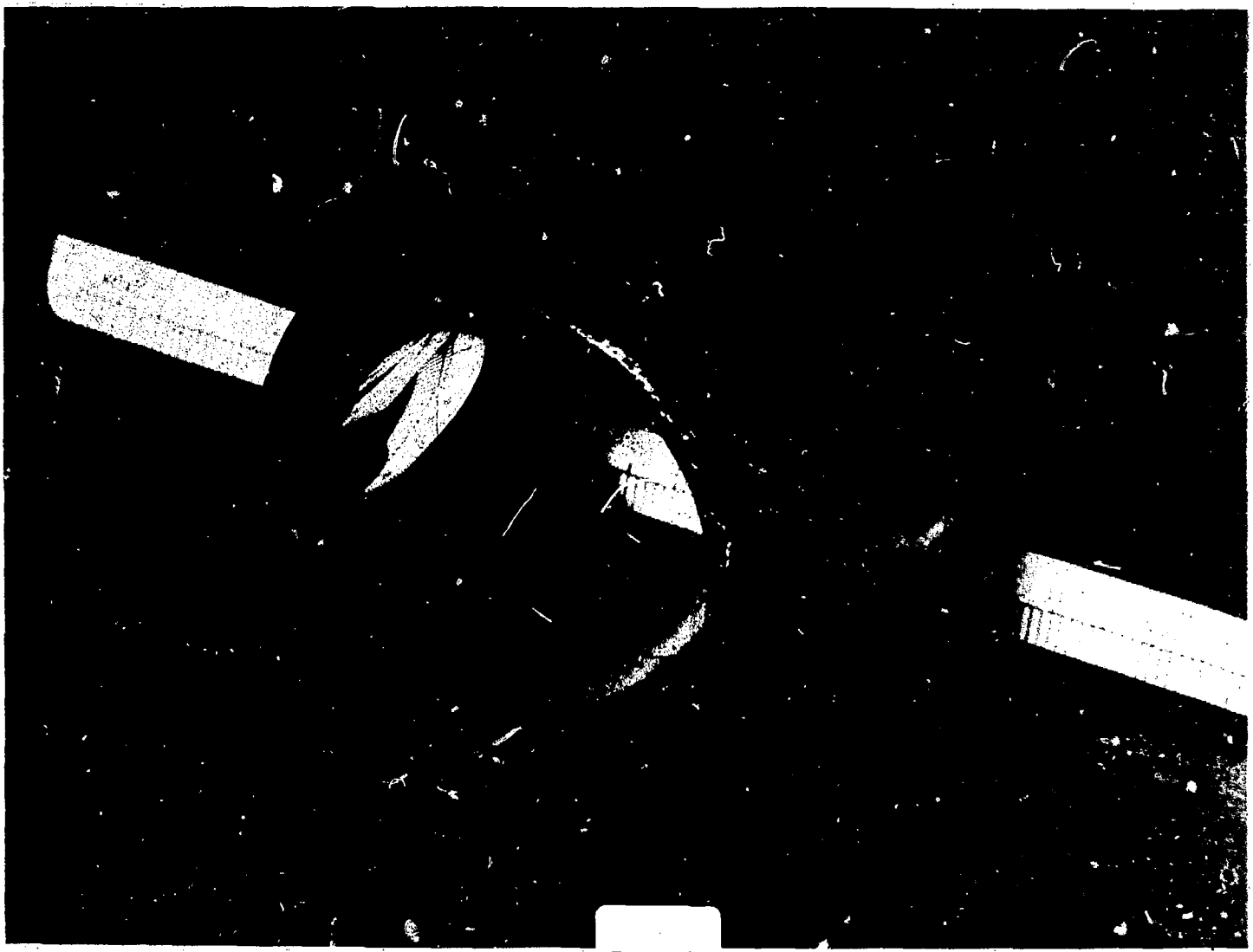

Figure 37

ZONE PLATE CODED IMAGING (PRINCIPLES):

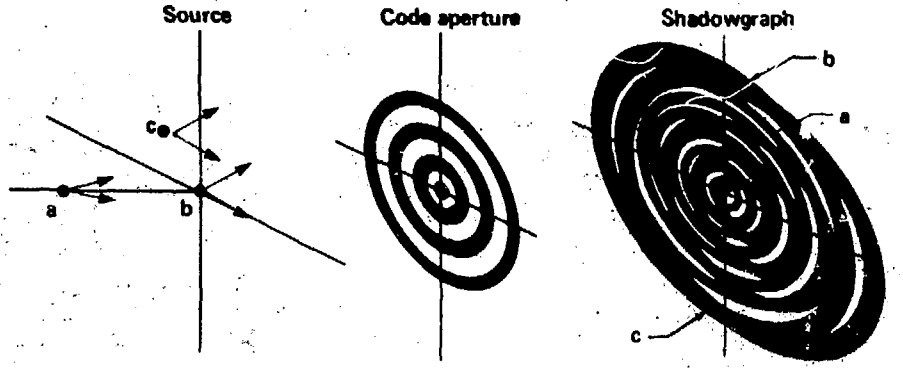

Each zone plate shadow uniquely characterizes the position of its associated source point

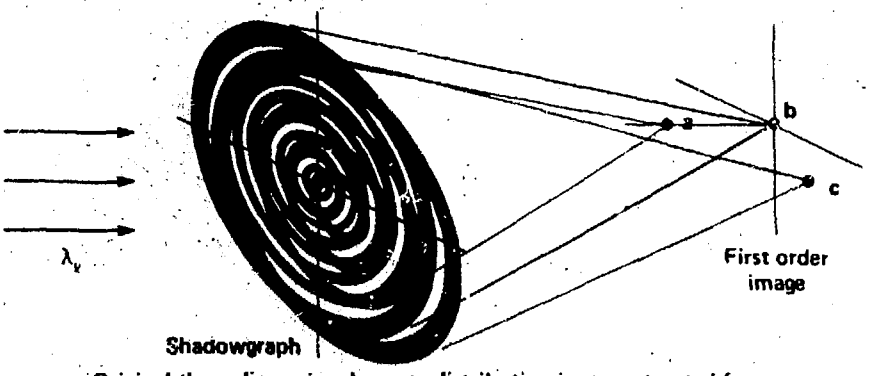

Original three dimensional source distribution is reconstructed from the shadowgraph

4/77

Figure 38

PARAMETRIC COMPARISON: X-RAY MICROSCOPE VERSUS ZONE PLATE CAMERA

Parameters	X-ray microscope	Zone plate camera
Planar resolution limit	1 μm surface smoothness limited	5.3 μm* limited by diffraction effects during shadowgraph recording
Solid angle for radiation collection	5×10^{-4} sr	9×10^{-1} sr
Tomographic resolution	None	10 μm
Radiations imaged	X-rays $\lambda \geqslant 2$ Å	All radiations $\lambda \leqslant 2.5$ Å ↓
Typical object distance	(30-50) cm	(1-2) cm

*ZPCI planar resolution limit depends on source spectrum. Specifically, $\delta \simeq 3.3\sqrt{\lambda_x S_1}$, λ_x is the maximum wavelength of interest. The P.R.L. quoted corresponds to $S_1 = 1$ cm, $\lambda_x = 2.5$ Å.

↓ZPCI spectral range depends on minimum linewidth of coded aperture. Specifically, $\lambda_x \leqslant (\Delta r)^2/4\, S_1$. The λ value quoted corresponds to $S_1 = 1$ cm, $\Delta r \simeq 3$ μm.

5/77

Figure 39

ZONE PLATE CODED IMAGE SUPRATHERMAL X-RAY DATA: (PRELIMINARY RESULTS)

Reconstructed x-ray image

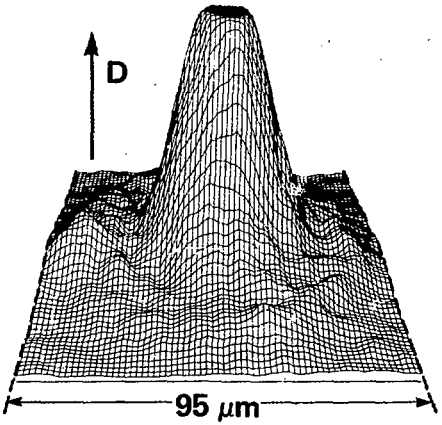

(3-D film density contour representation)

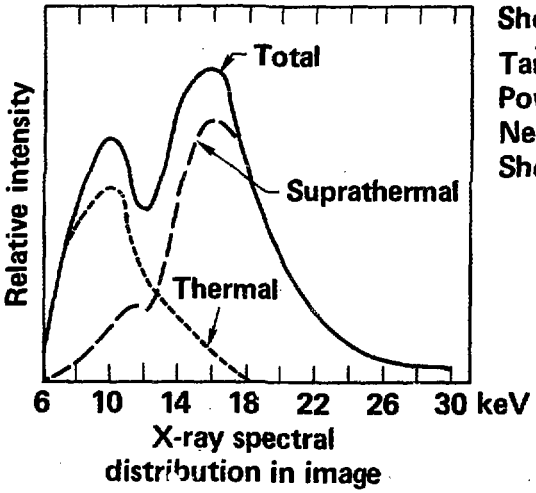

Shot Parameters:

Targer ball diameter: 89 μm
Power on target: 4×10^{12} watt
Neutron yield: $(1.4 \pm 0.3) \times 10^{9}$
Shot I.D. 36120906; RX1291-1C

Figure 40

ALICS/CALICS SPECTROMETER

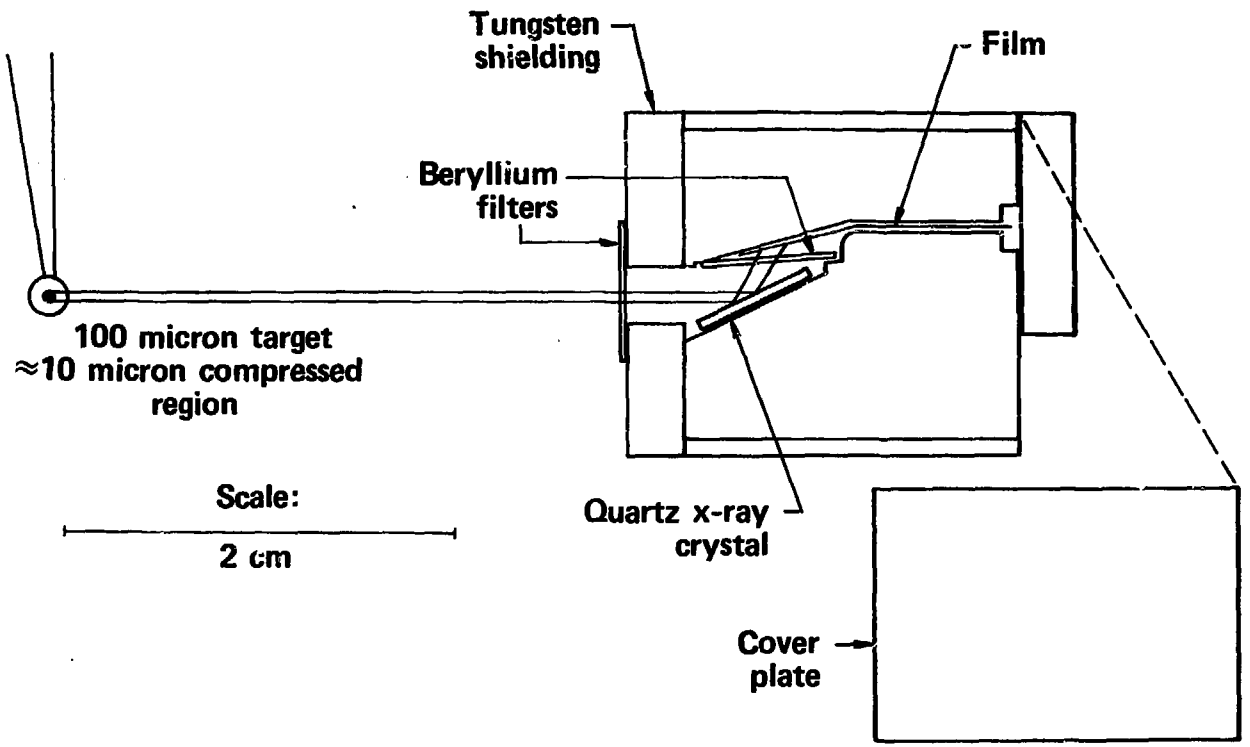

Figure 41

X-RAY STREAK CAMERA

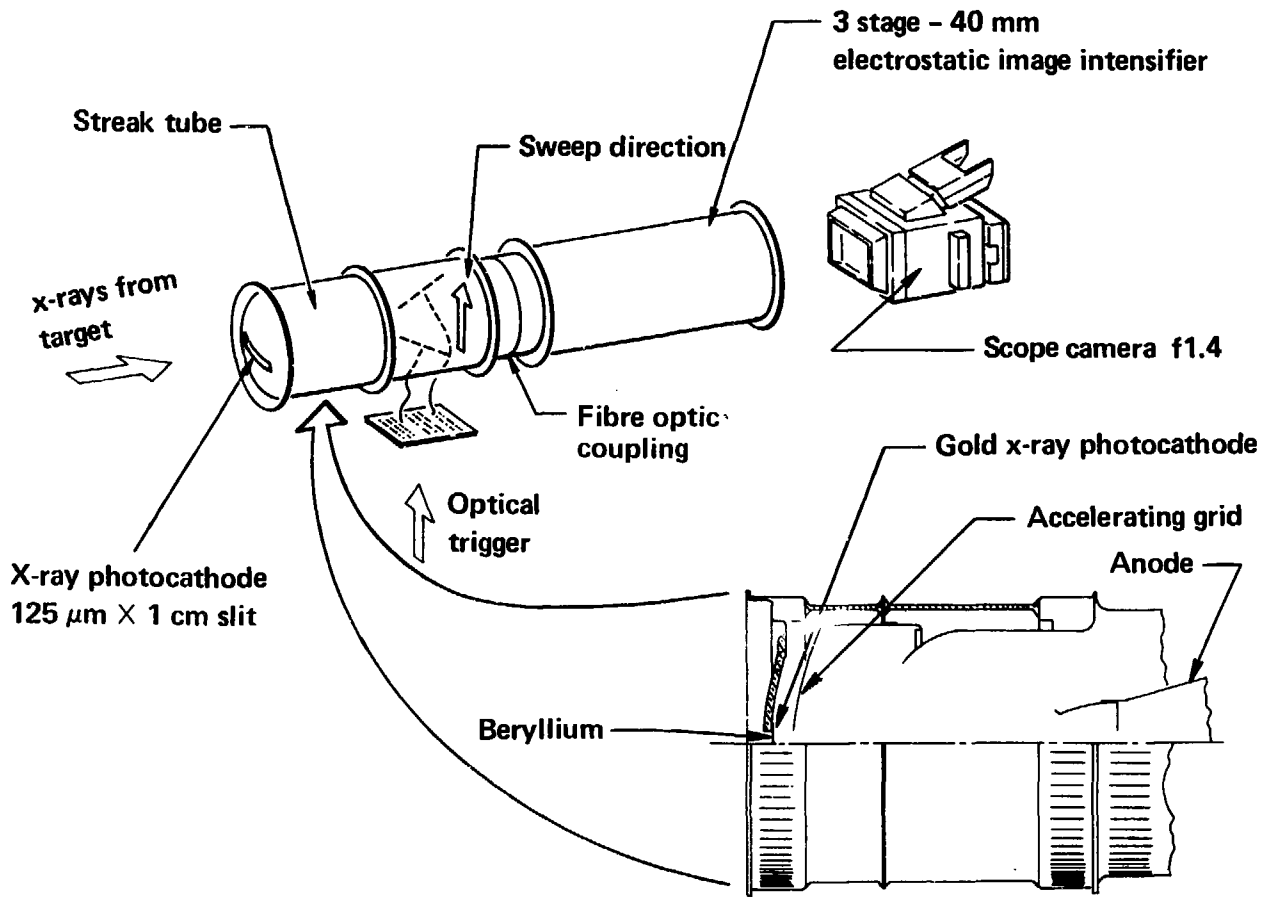

Figure 42

TIME RESOLVED X-RAY SPECTRUM

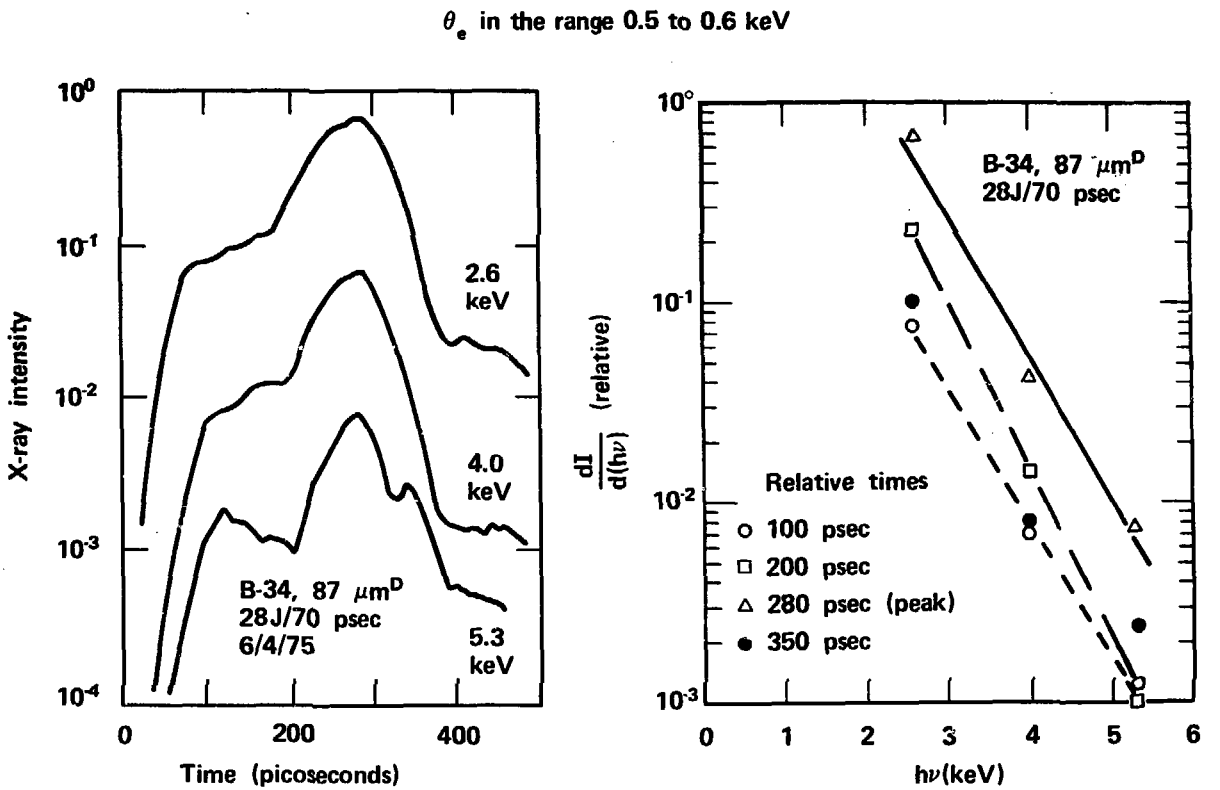

Figure 43

X-RAY TEMPORAL SIGNATURE AS A FUNCTION OF LASER POWER

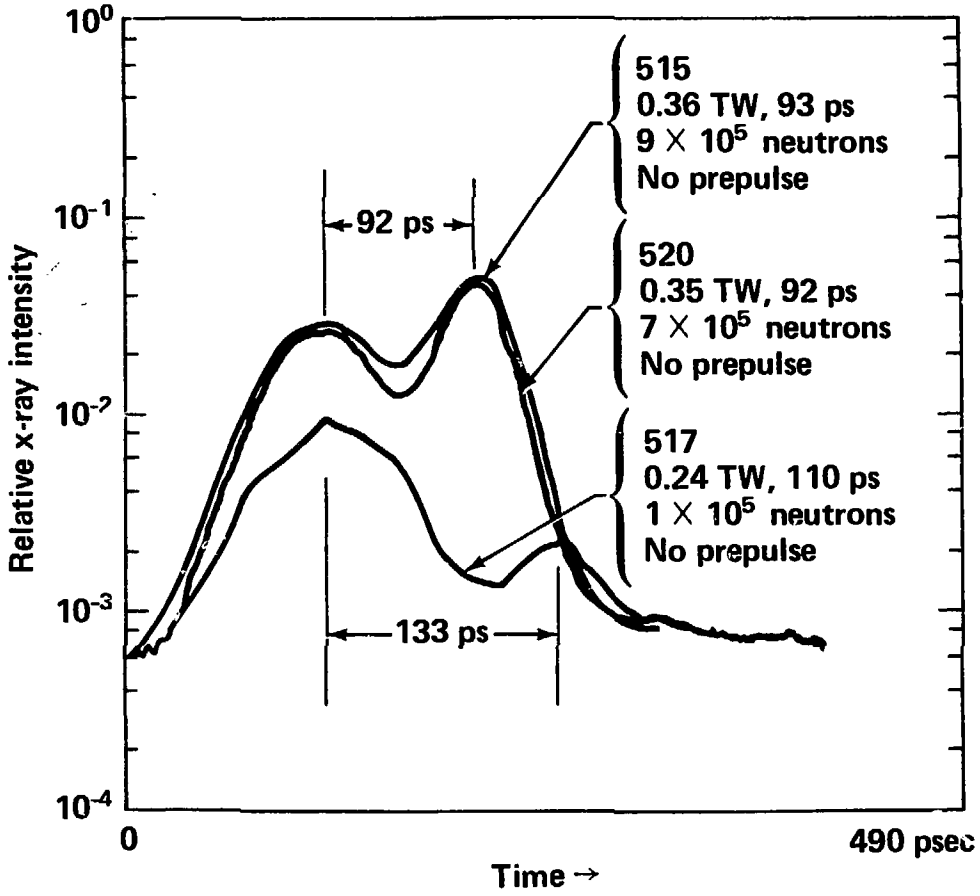

Figure 44

X-RAY STREAK RECORD OF Au-DISK

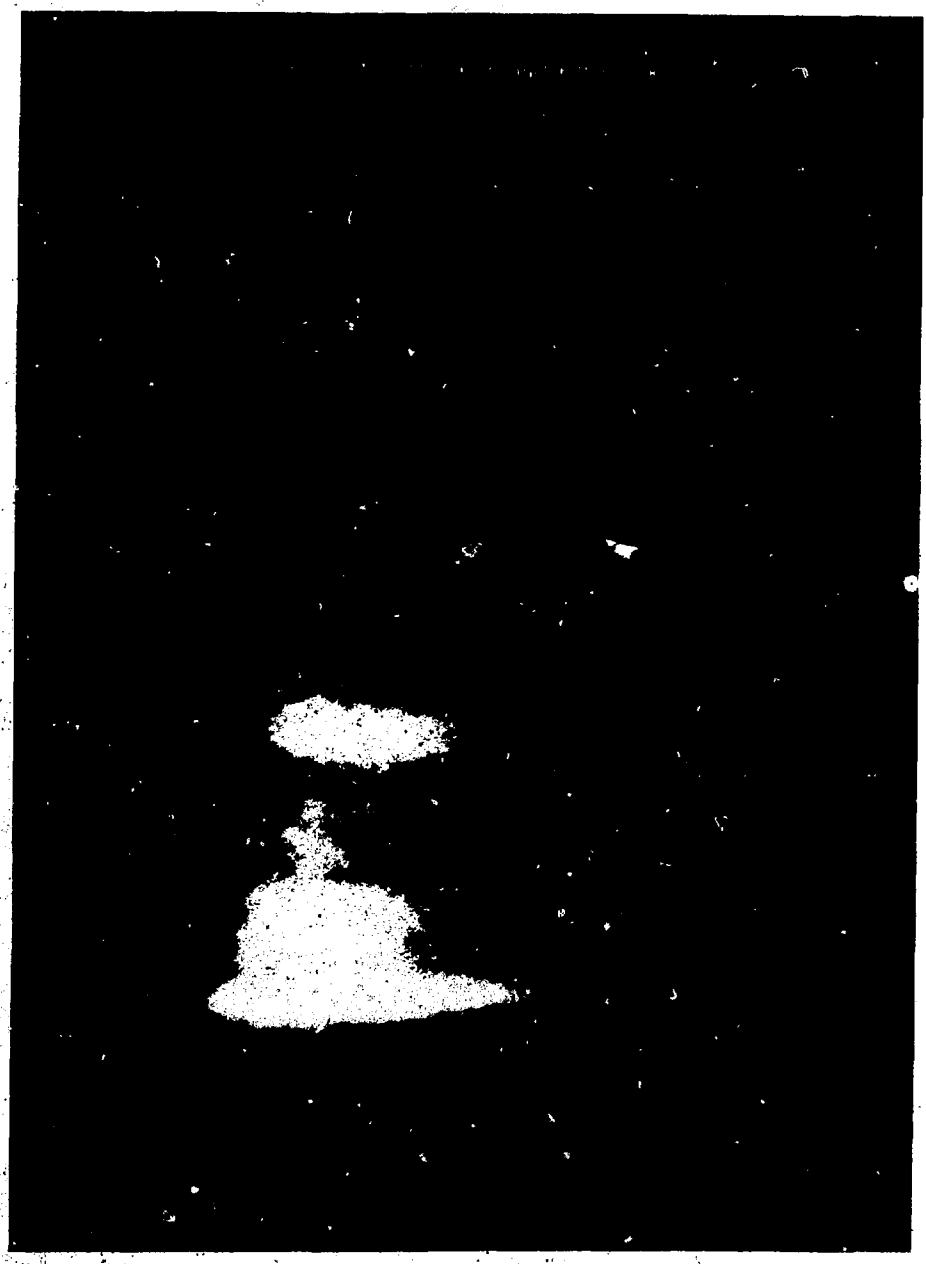

Figure 45

TIME-RESOLVED X-RAY EMISSION AND X-RAY SPECTRA OF Au-DISK

Shot #37070712: 357 J/242 ps, 2.82 × 10^{15} W/cm^2

Channel	Elem.	K-edge (keV)
1	Cl	2.8
4	Ti	4.96
6	Co	7.7
7	Zn	9.7
8	Ag	25.5

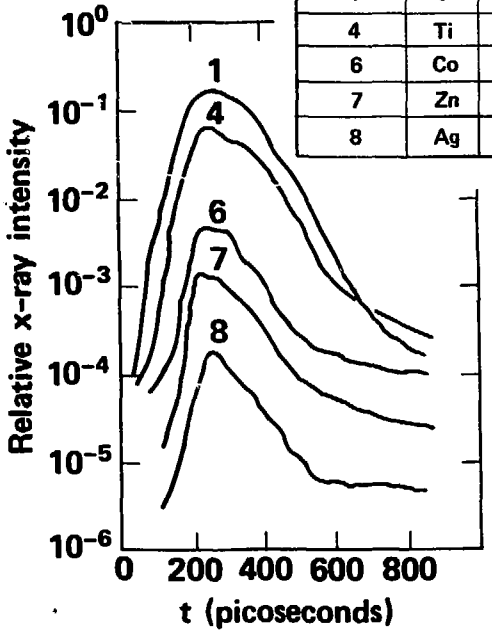

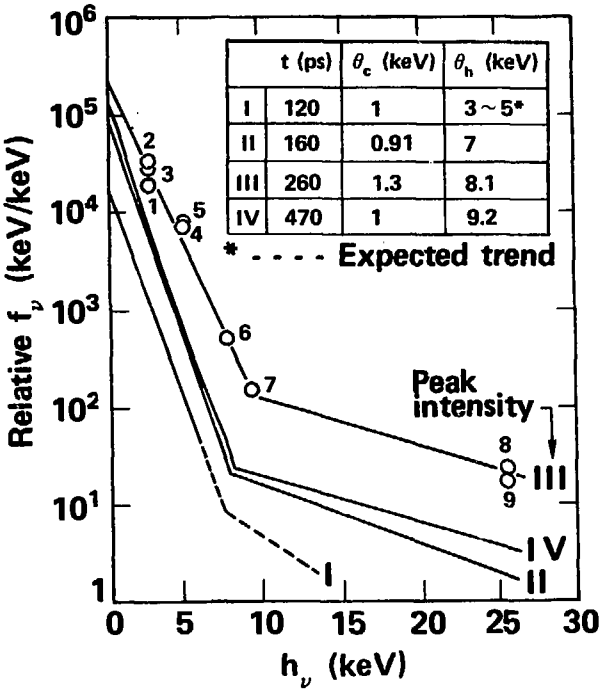

	t (ps)	θ_c (keV)	θ_h (keV)
I	120	1	3 ~ 5*
II	160	0.91	7
III	260	1.3	8.1
IV	470	1	9.2

* - - - - Expected trend

20-50-0877-1540

Figure 46

TIME-RESOLVED X-RAY SPECTRA (Au-DISK)

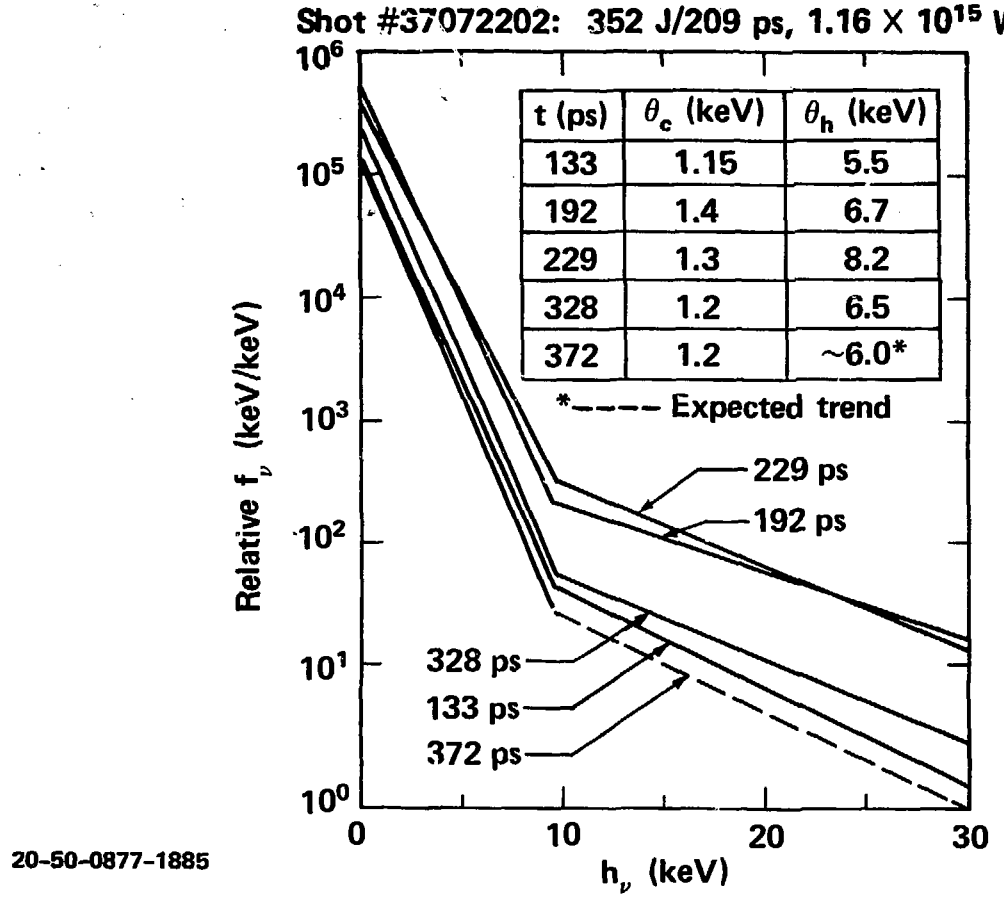

Figure 47

EVOLUTION OF THERMAL AND SUPRATHERMAL TEMPERATURES OF GOLD DISK TARGET

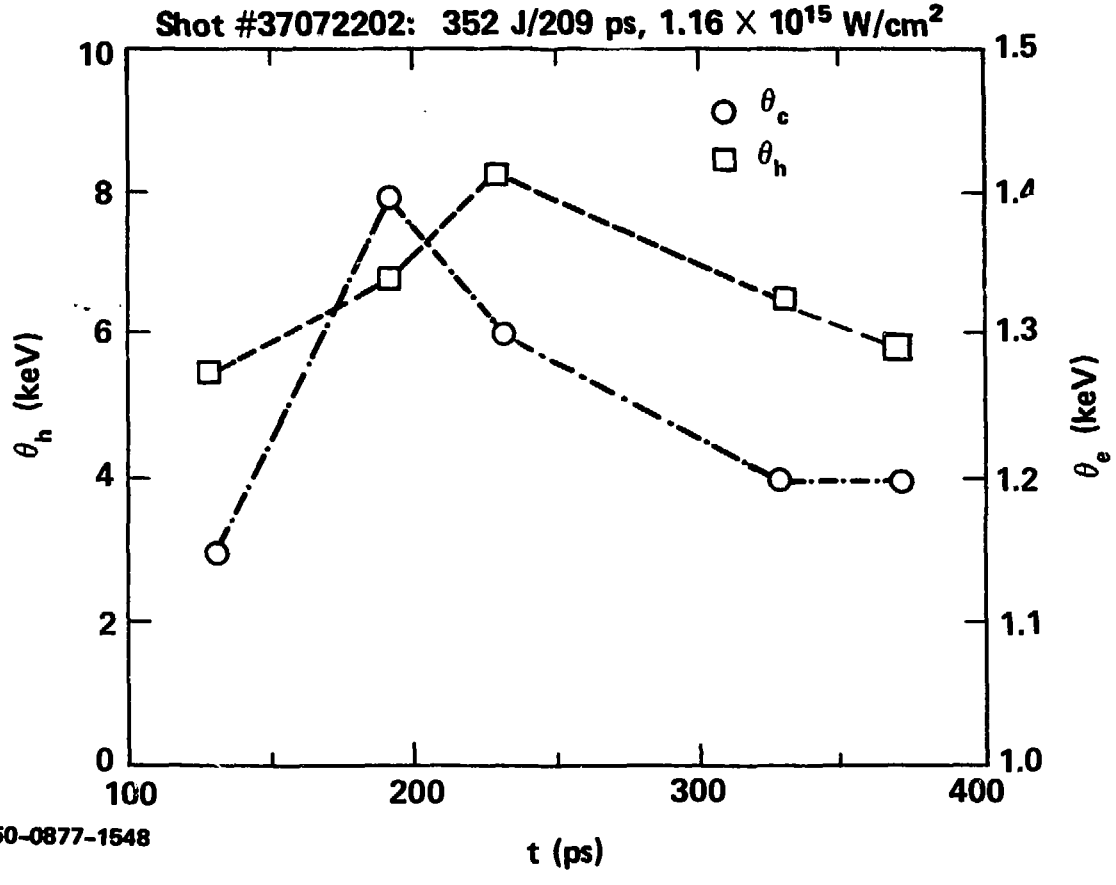

Figure 48

DANTE

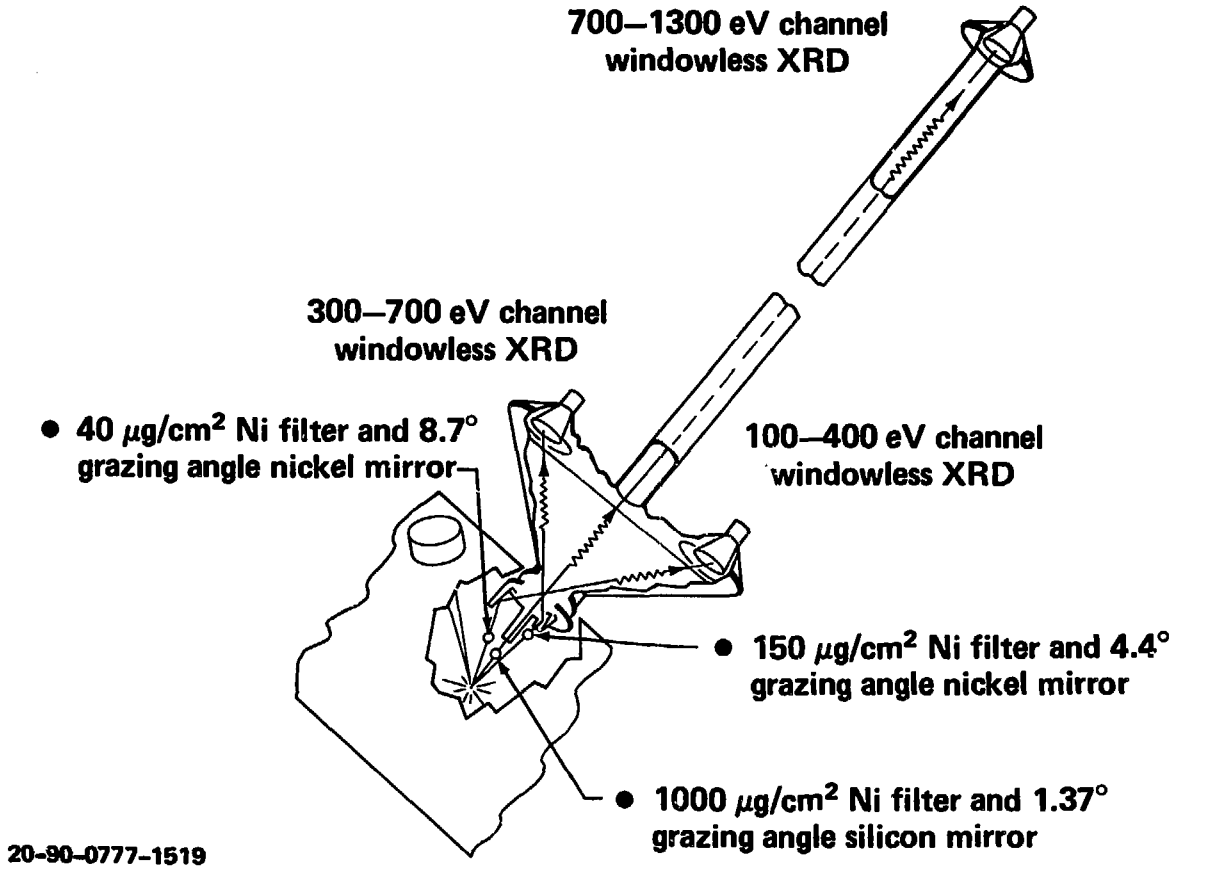

Figure 4

3 CHANNEL SUBKILOVOLT DETECTOR RESPONSE FUNCTIONS

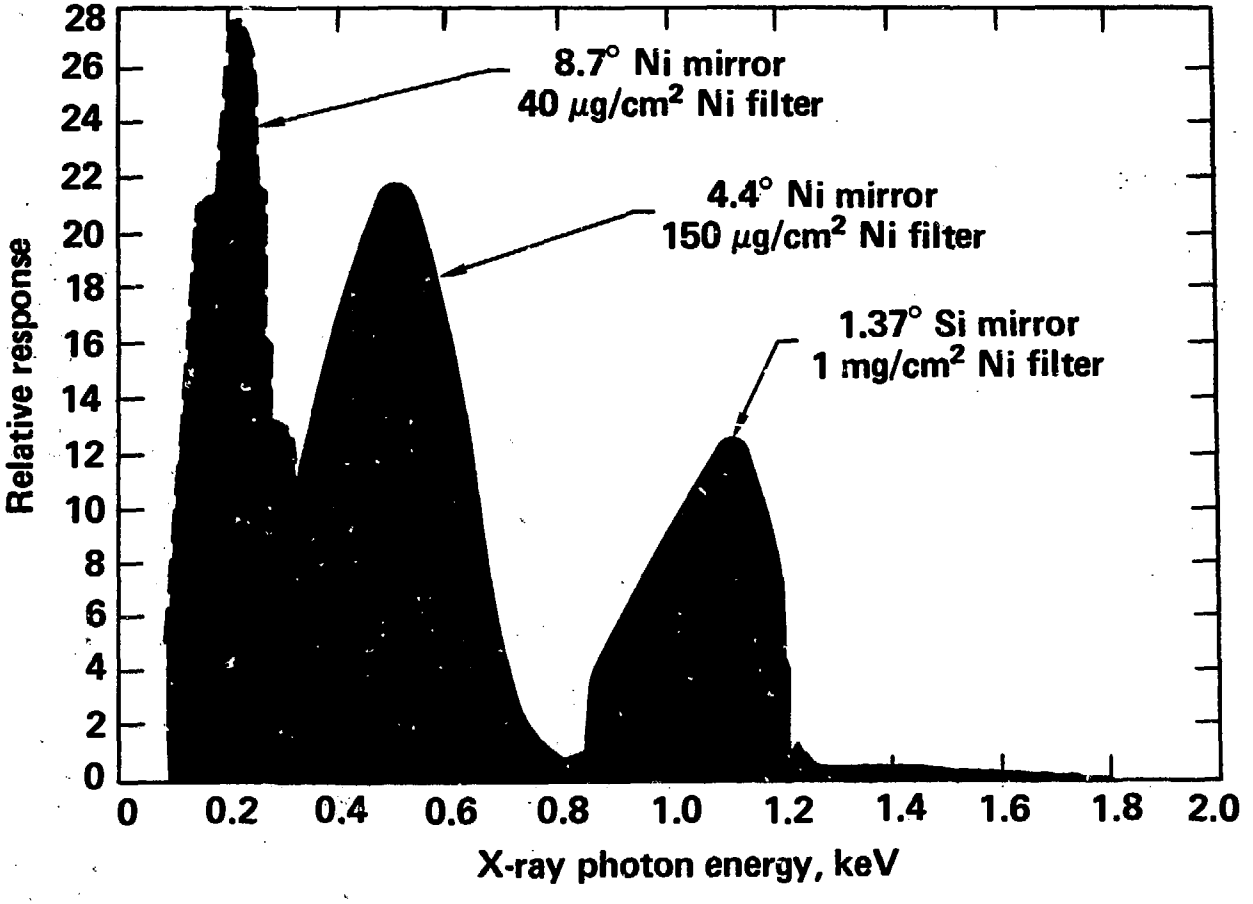

20-50-0777-1413

Figure 50

ALIGNMENT SCHEME FOR SPACE-TIME X-RAY EMISSION STUDIES

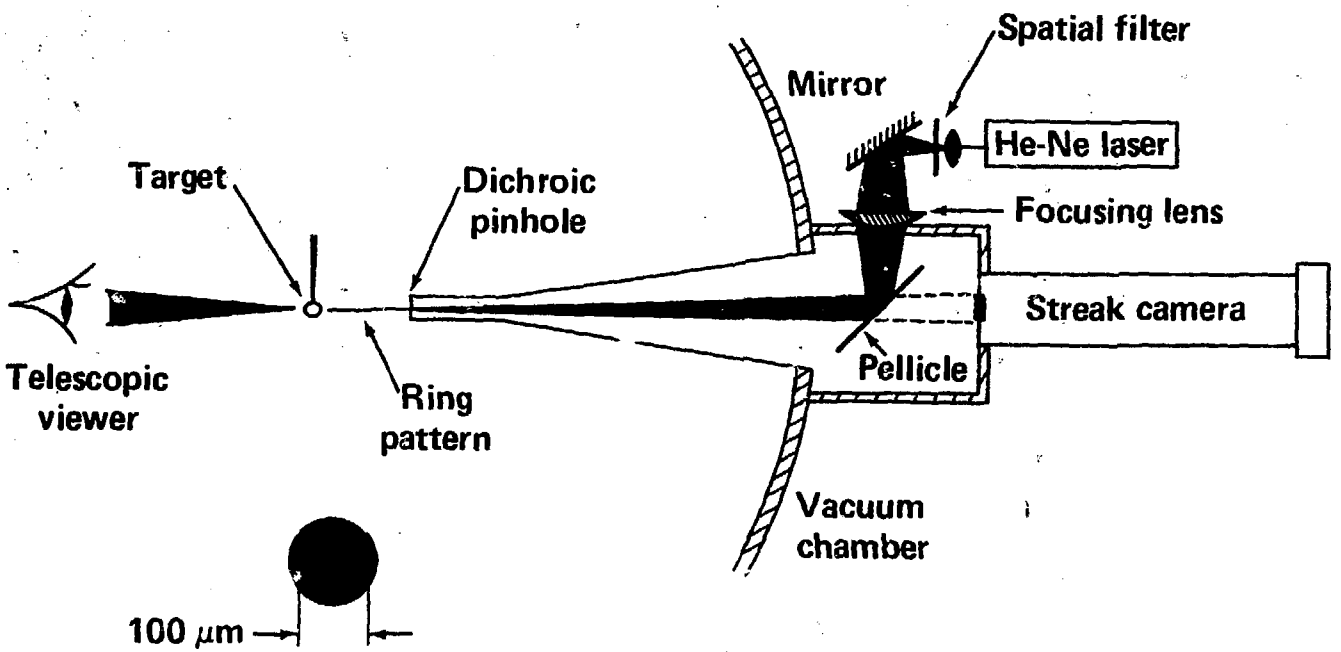

Figure 51

TIME RESOLVED IMPLOSION VELOCITIES

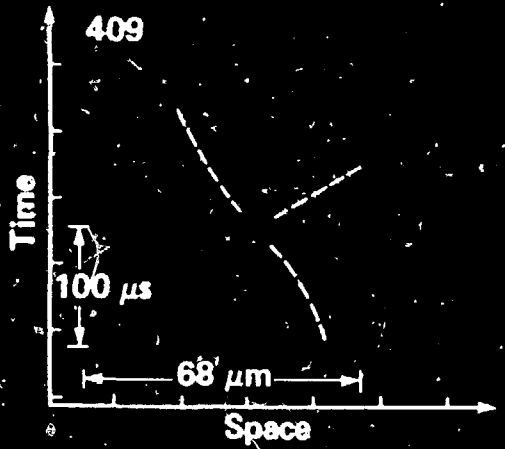

One-sided implosion
(76070906)

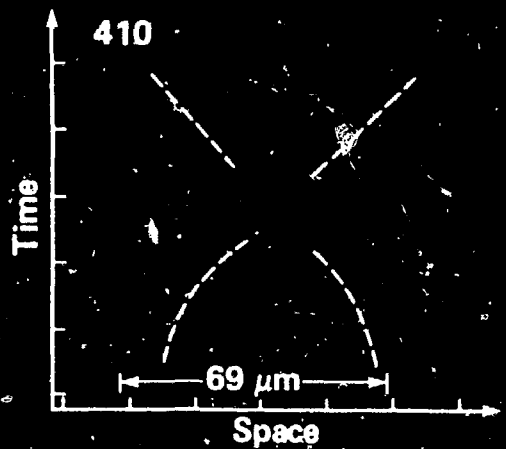

Two-sided implosion
(77070805)

Parameters: 0.5 μm wall, 1.3 – 1.8 mg/cc DT fill, 0.45 TW/70 ps FWHM,
2×10^5 neutrons one-sided, 1×10^6 neutrons two-sided.

40-80-0877-1631

Figure 52

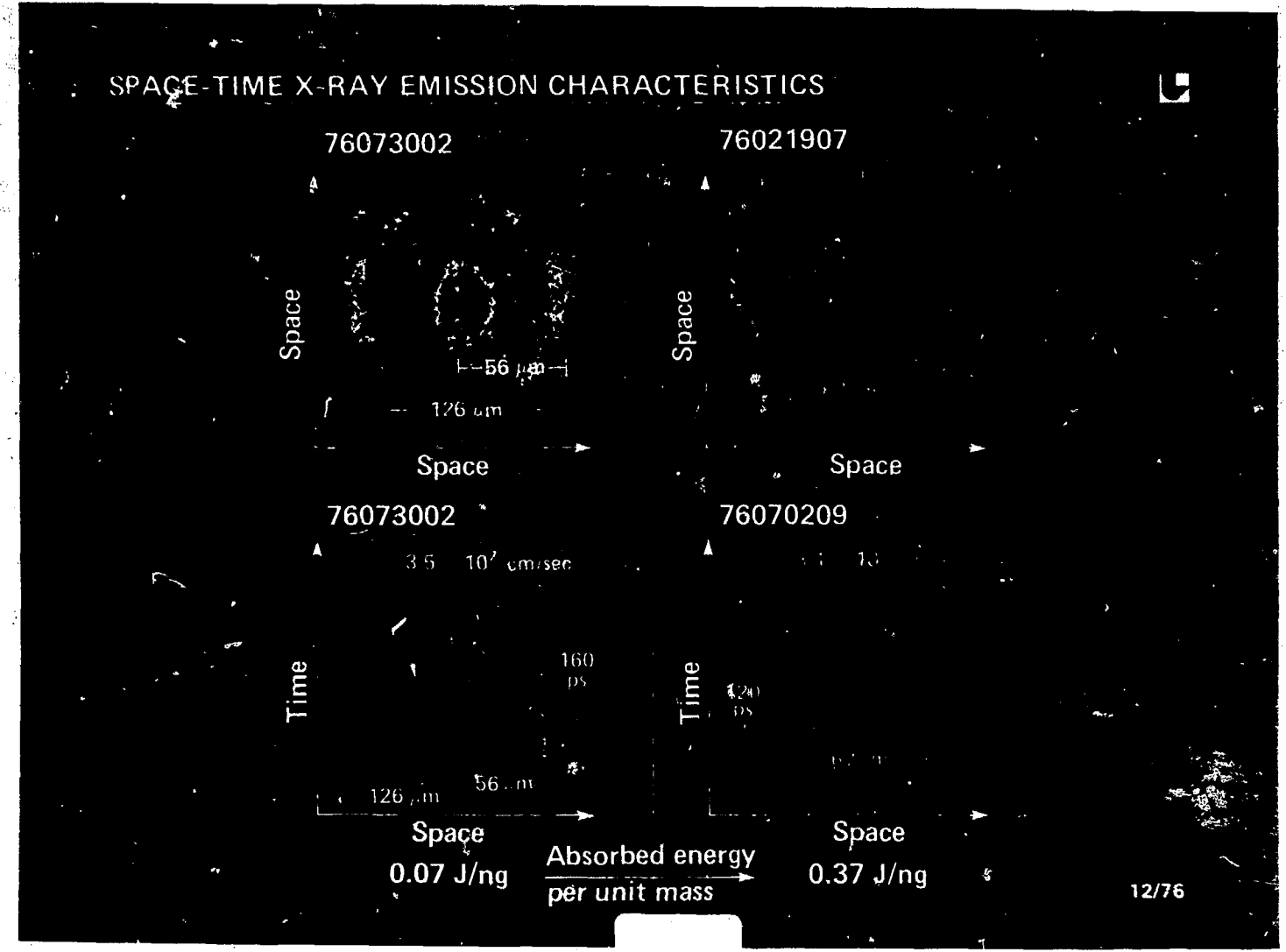
SPACE-TIME X-RAY EMISSION CHARACTERISTICS
76073002
76021907
Space
56 μm
126 μm
Space
Space
Space
76073002
76070209
3.5 10⁷ cm/sec
Time
160 ps
Time
126 μm
56 μm
Space
0.07 J/ng
Absorbed energy per unit mass
Space
0.37 J/ng
12/76

Figure 53

ULTRAFAST FRAMING CAMERA

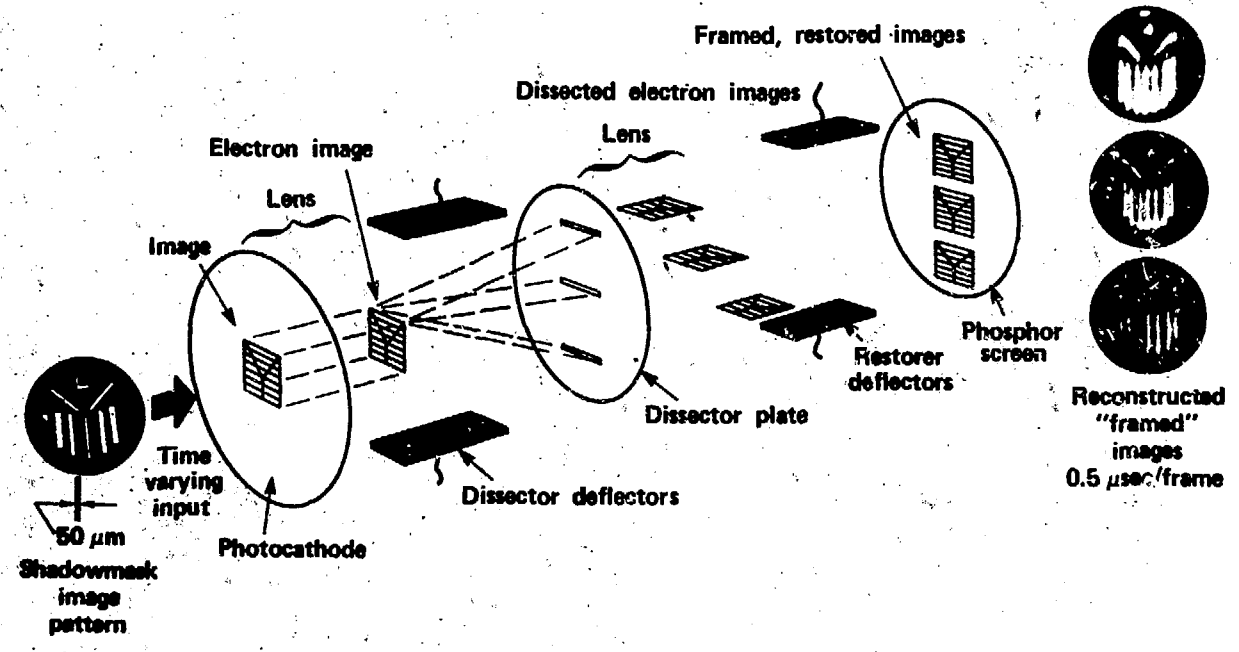

UV HOLOGRAPHIC INTERFEROMETER PROBE PULSE OPTICS

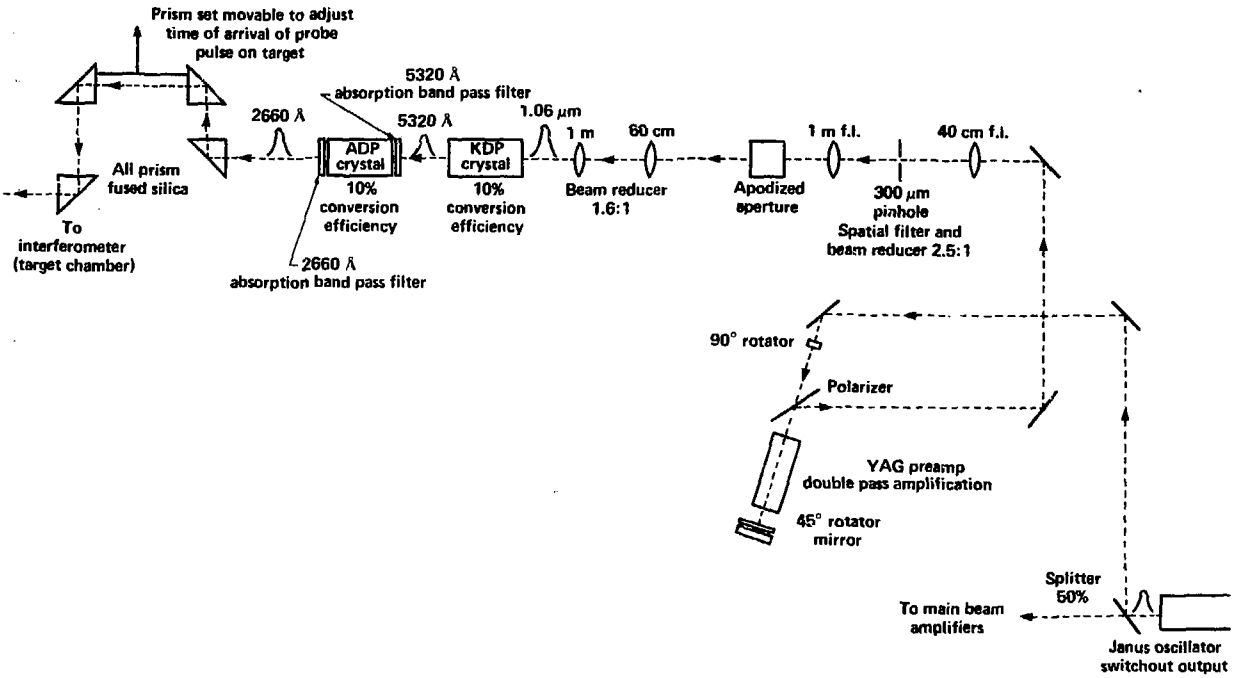

20-01-0877-1521

Figure 55

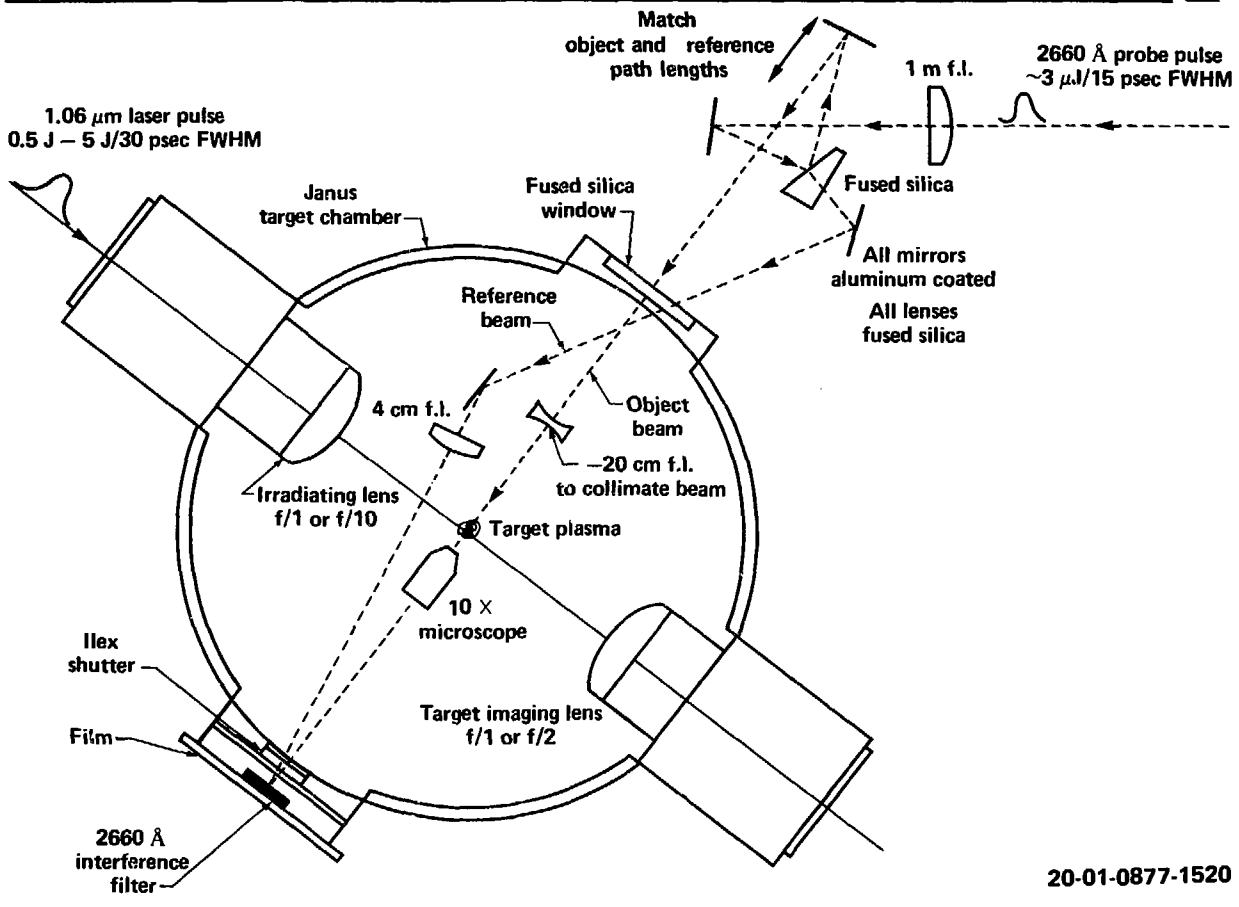
UV HOLOGRAPHIC INTERFEROMETER TARGET CHAMBER SETUP
Match
object and reference
path lengths
1 m f.l.
2660 Å probe pulse
~3 μJ/15 psec FWHM
1.06 μm laser pulse
0.5 J – 5 J/30 psec FWHM
Janus
target chamber
Fused silica
window
Fused silica
All mirrors
aluminum coated
All lenses
fused silica
Reference
beam
4 cm f.l.
Object
beam
–20 cm f.l.
to collimate beam
Irradiating lens
f/1 or f/10
Target plasma
10 X
microscope
Ilex
shutter
Film
Target imaging lens
f/1 or f/2
2660 Å
interference
filter
20-01-0877-1520

Figure 56

FRINGE NUMBER IS A STRONG FUNCTION OF IMAGE PLANE POSITION IN A STEEP GRADIENT PLASMA – CAN LEAD TO LARGE ERRORS IF MISINTERPRETED

77050202

Figure 57

PROFILE STEEPENING ON AXIS

(2660 Å, 15 psec, 1 μm)

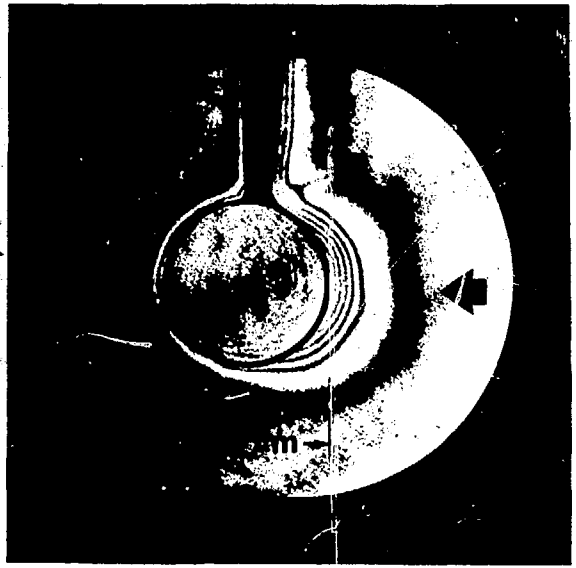

1.06 μm, ~10^{14} W/cm^2, 41 μm^D

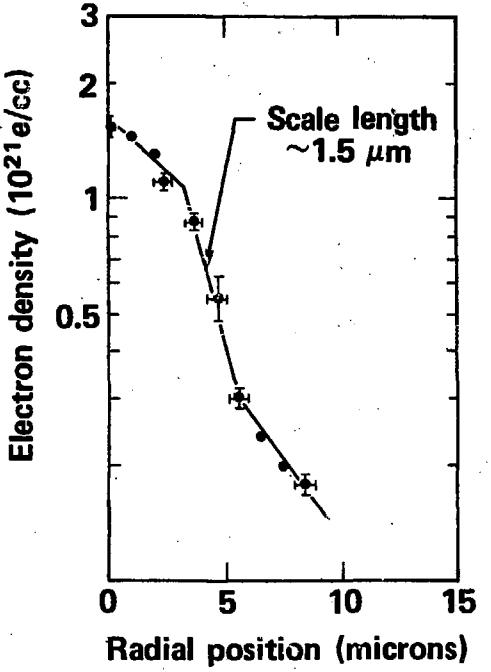

40-90-0877-1518

Figure 58

ELLIPSOMETER DETERMINES THE POLARIZATION ELLIPSE OF THE SCATTERED LIGHT

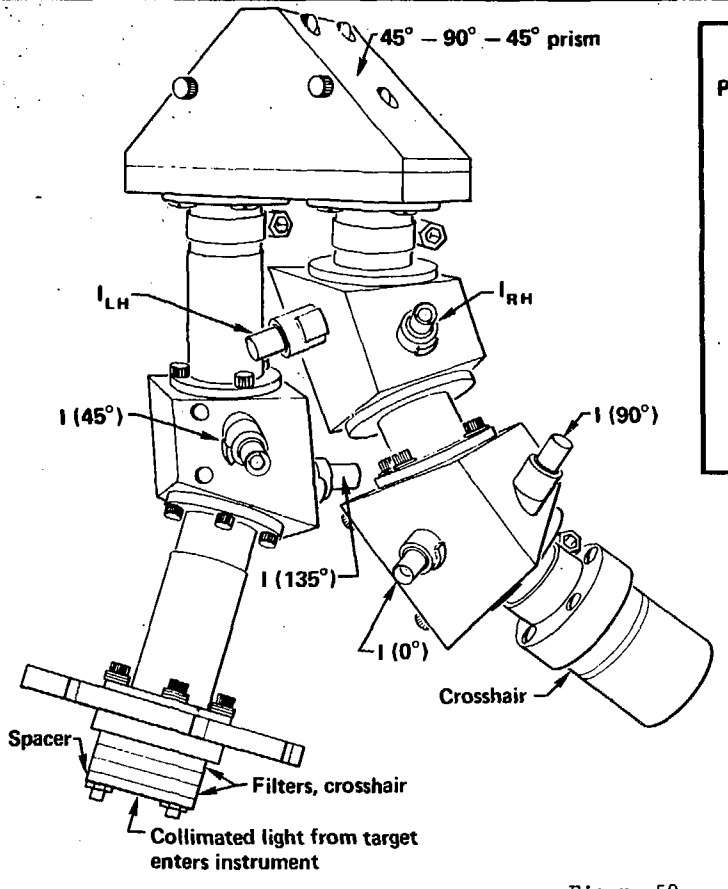

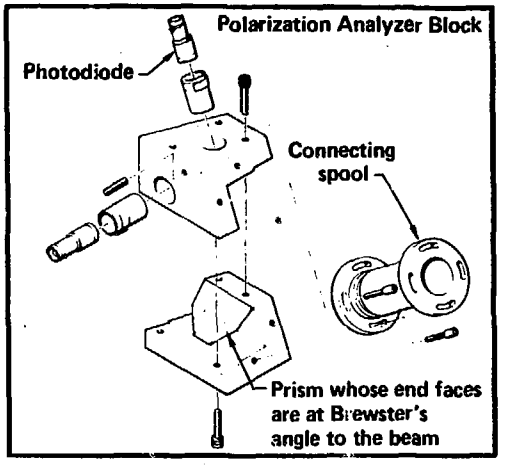

Figure 59

DETERMINATION OF THE SCALE HEIGHT BY POLARIMETRY

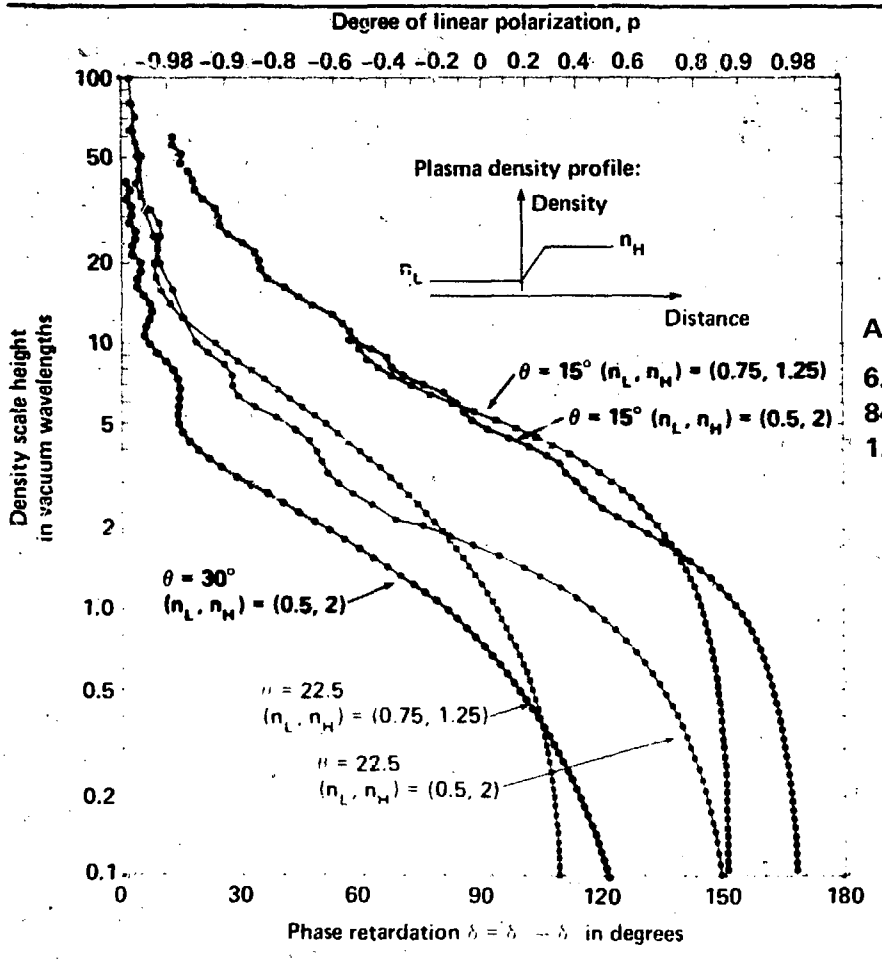

ARGUS shot #36080406

6.4J (N)/40.6J (S) incident
84 μ OD, 0.8 μ WT, 1.9 mg/cm^3 DT
1.3 · 10^7 neutrons

p = 0.77

Figure 60

ELECTRON SPECTROMETER (90° FOCUSING)

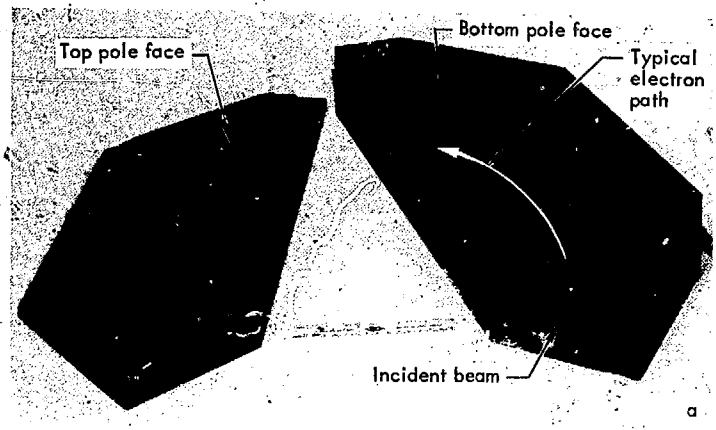

a. Magnet

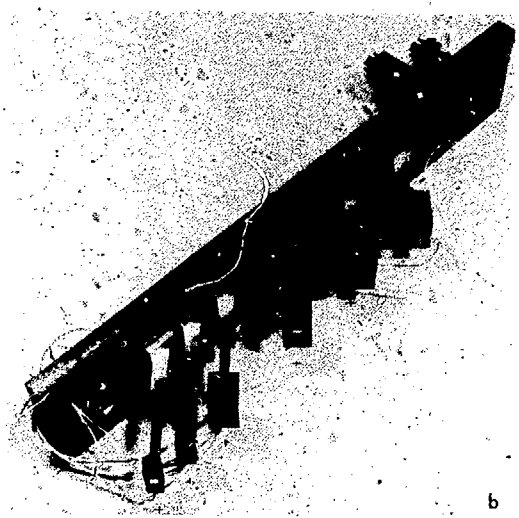

b. Associated detector array.

Figure 61

THE HIGH RESOLUTION WIDE BAND SPECTROMETER COVERS A PROTON ENERGY RANGE FROM 12 keV TO 60 MeV

For each channel mE/q^2 = constant

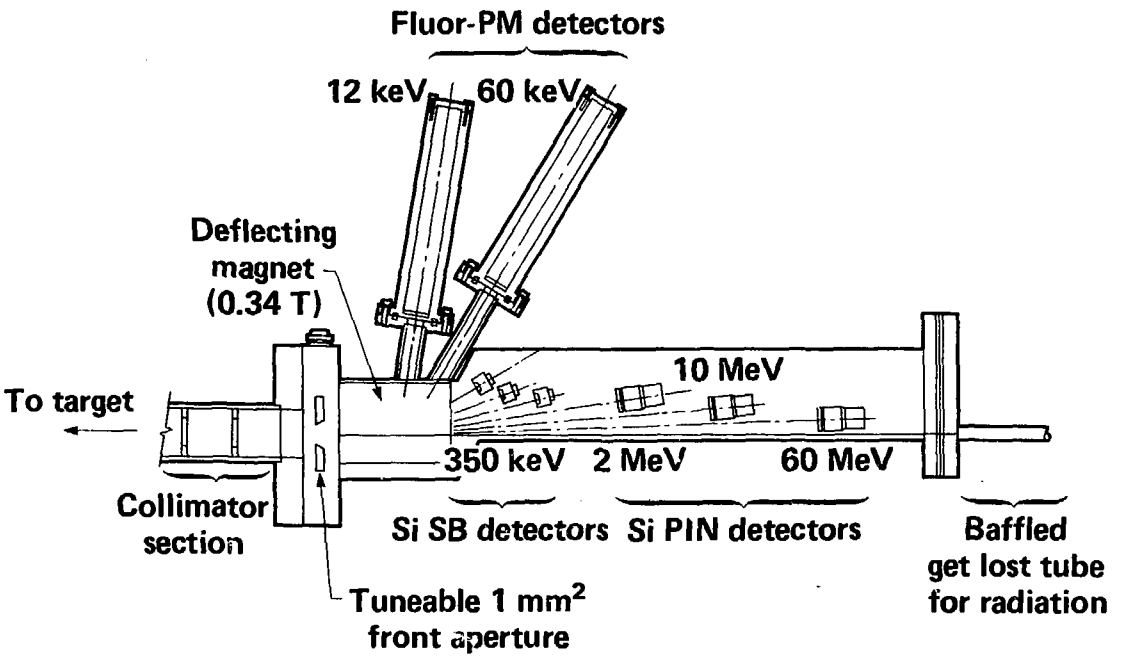

20-90-0877-1603

Figure 62

MAGNETIC DEFLECTION AND TIME OF FLIGHT SEPARATE IONS OF DIFFERENT CHARGE TO MASS RATIO

Within the deflection region, trajectories are circles with radius R, such that

$$BR = \frac{m}{q} v = \frac{1}{q} \sqrt{2mE}$$

In the drift region, trajectories are straight lines, such that

$$x = R - \sqrt{R^2 - L^2} + \frac{LD}{\sqrt{R^2 - L^2}}$$

or for $R > L,D$ $\quad x = \frac{L}{R}\left(D + \frac{L}{2}\right)$

For $R > L,D$ the time of flight for a target to magnet entrance distance d is

$$t = (d + L + D)/v$$

∴For a narrow slit at x . . . . $t \sim m/q$

20-90-0877-1604

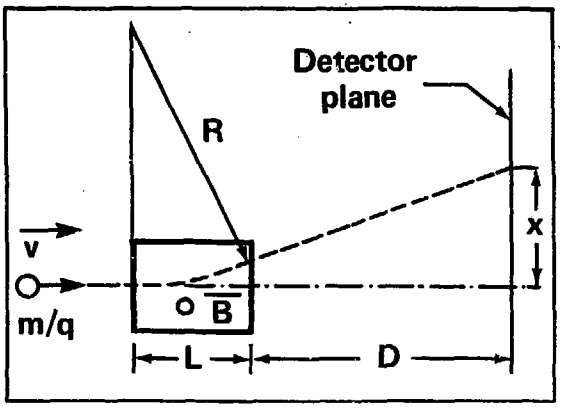

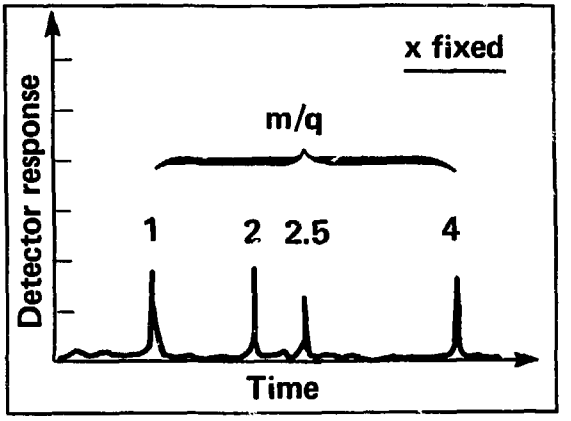

Figure 63

TOF NEUTRON DETECTOR

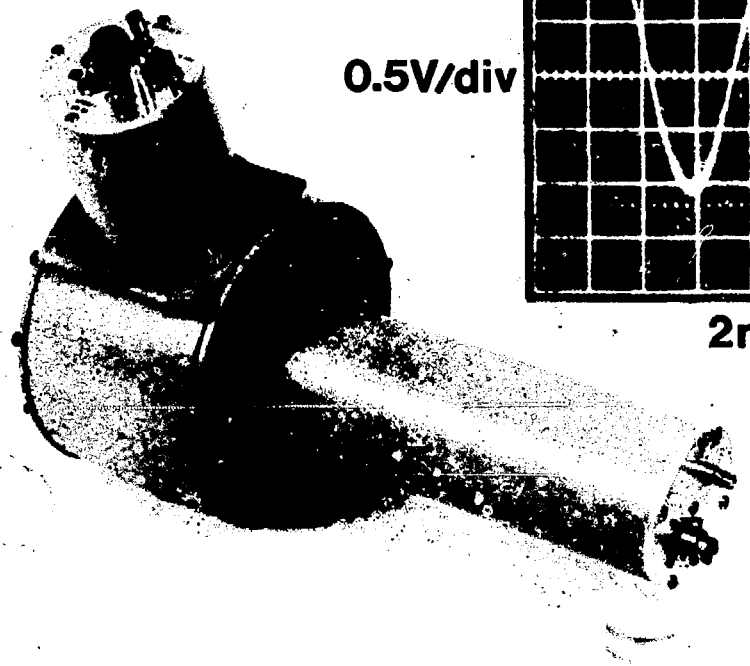

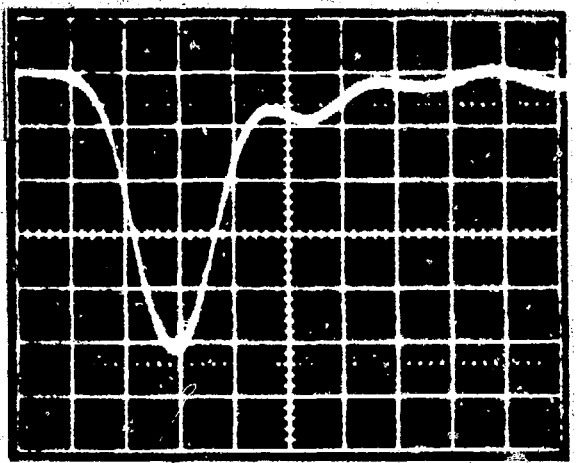

Sensitivity
0.14 V·ns/neutron

40-46-0577-1421

Figure 64

D-T NEUTRON YIELD BY ACTIVATION OF COPPER

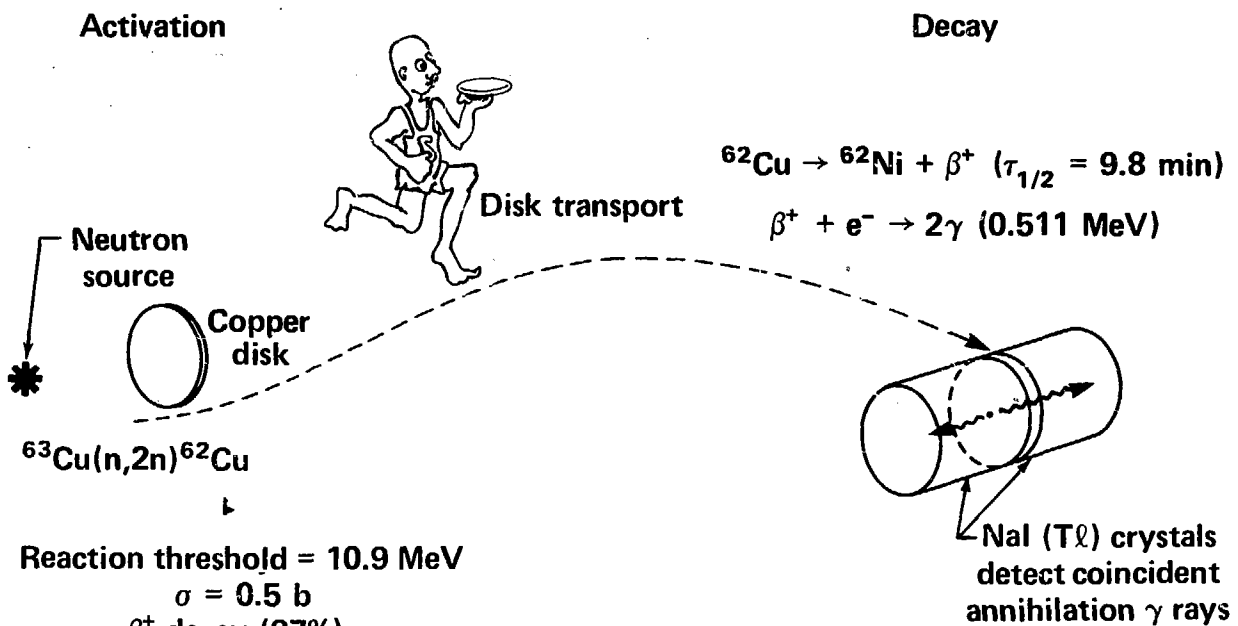

40-46-0877-1592

Figure 65

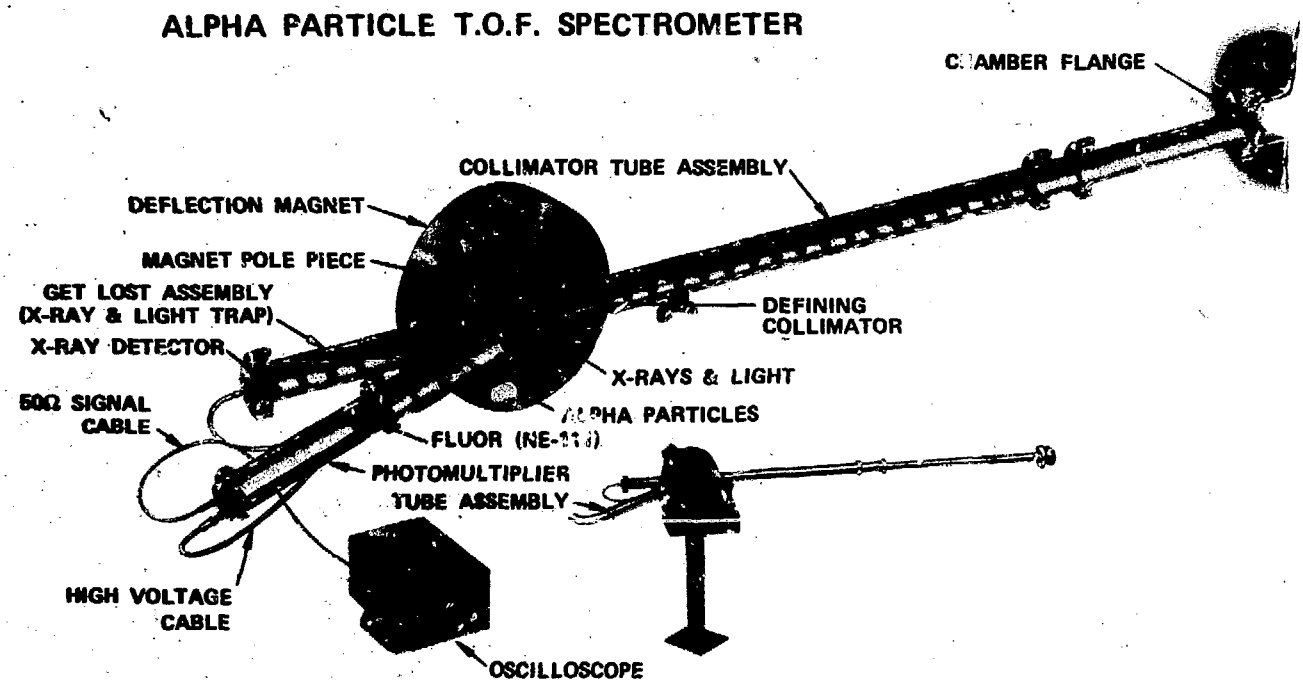
ALPHA PARTICLE T.O.F. SPECTROMETER
CHAMBER FLANGE
COLLIMATOR TUBE ASSEMBLY
DEFLECTION MAGNET
MAGNET POLE PIECE
GET LOST ASSEMBLY
(X-RAY & LIGHT TRAP)
X-RAY DETECTOR
50Ω SIGNAL
CABLE
DEFINING
COLLIMATOR
X-RAYS & LIGHT
ALPHA PARTICLES
FLUOR (NE-11
PHOTOMULTIPLIER
TUBE ASSEMBLY
HIGH VOLTAGE
CABLE
OSCILLOSCOPE

Figure 66

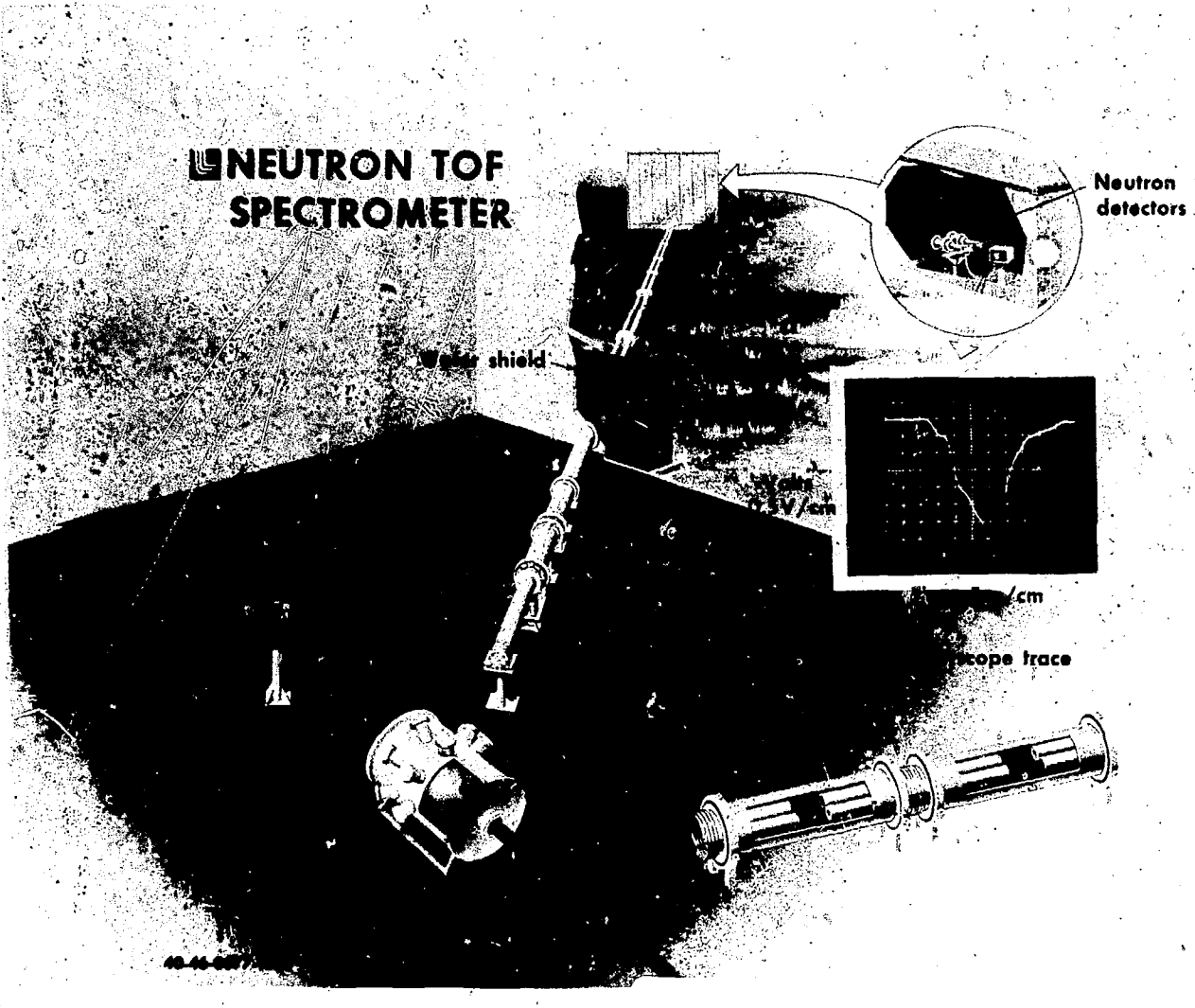
NEUTRON TOF SPECTROMETER
Neutron detectors
shield
V/cm
/cm
cope trace

Figure 67

NEUTRON AND α TIME-OF-FLIGHT MEASUREMENTS DETERMINE THE FUEL TEMPERATURE

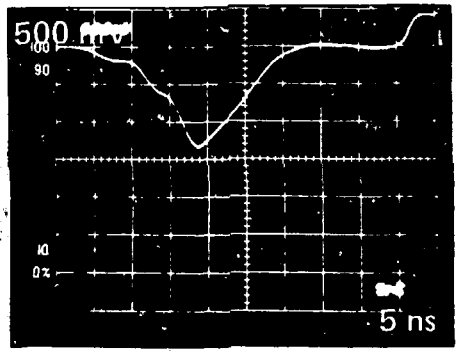

Neutrons

E_{peak} = 14.07 MeV
ΔE = 423 keV
$\Rightarrow T_i \leqslant$ 5.7 keV
346 neutrons reacting with detector

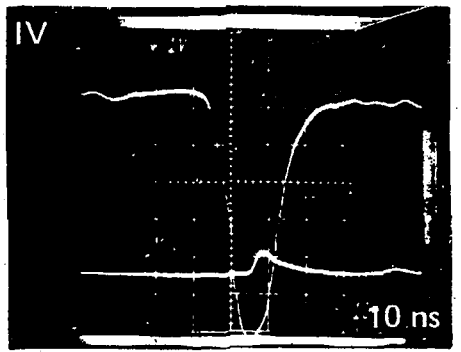

α-particles

E_{peak} = 3.4 MeV
ΔE = 460 keV
$\Rightarrow T_i \leqslant$ 6.7 keV
405 α's reacting with detector

Shot: 36092208

9/76

Figure 68

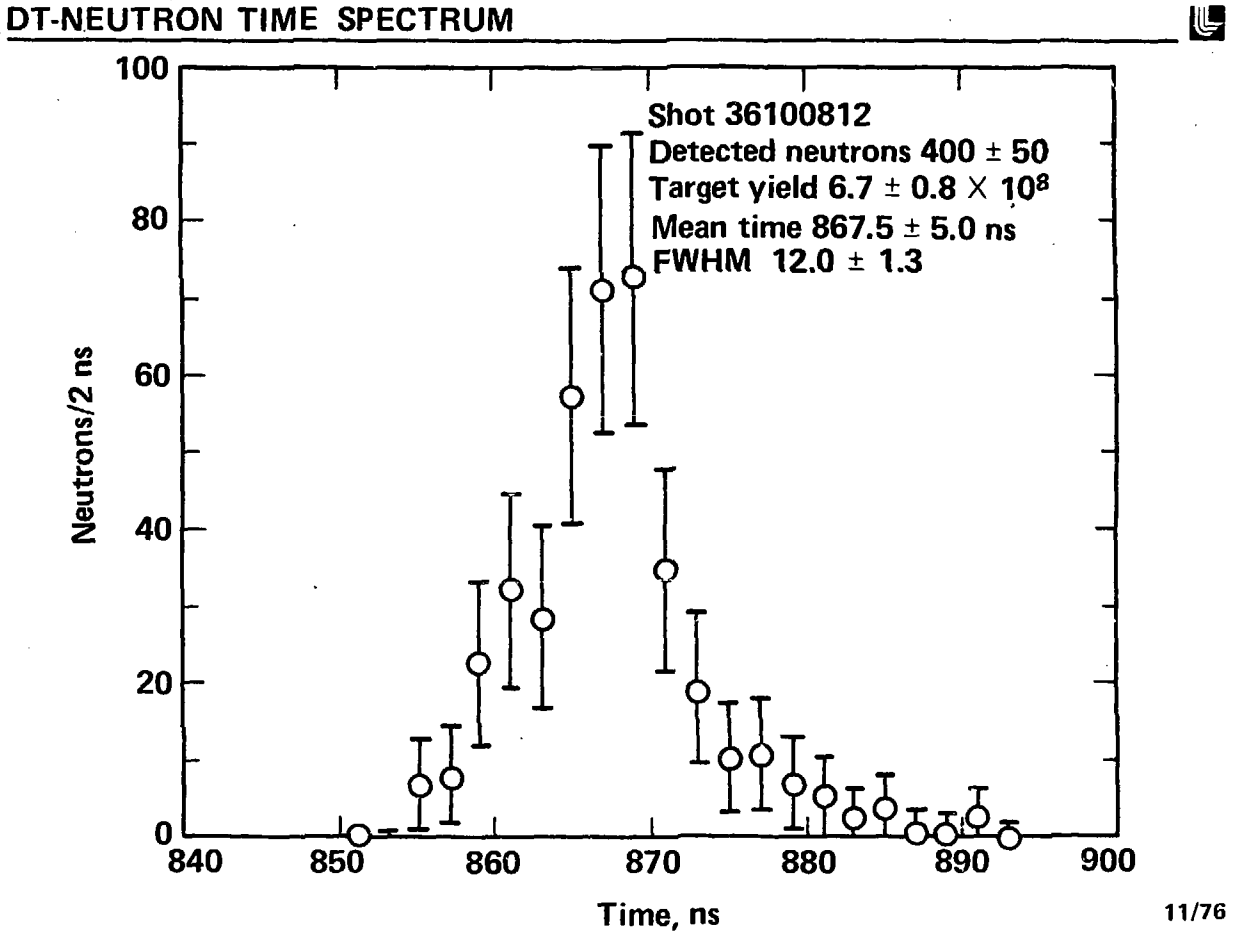
DT-NEUTRON TIME SPECTRUM
Shot 36100812
Detected neutrons 400 ± 50
Target yield 6.7 ± 0.8 X 10⁸
Mean time 867.5 ± 5.0 ns
FWHM 12.0 ± 1.3
Neutrons/2 ns
Time, ns
100
80
60
40
20
0
840
850
860
870
880
890
900
11/76

Figure 69

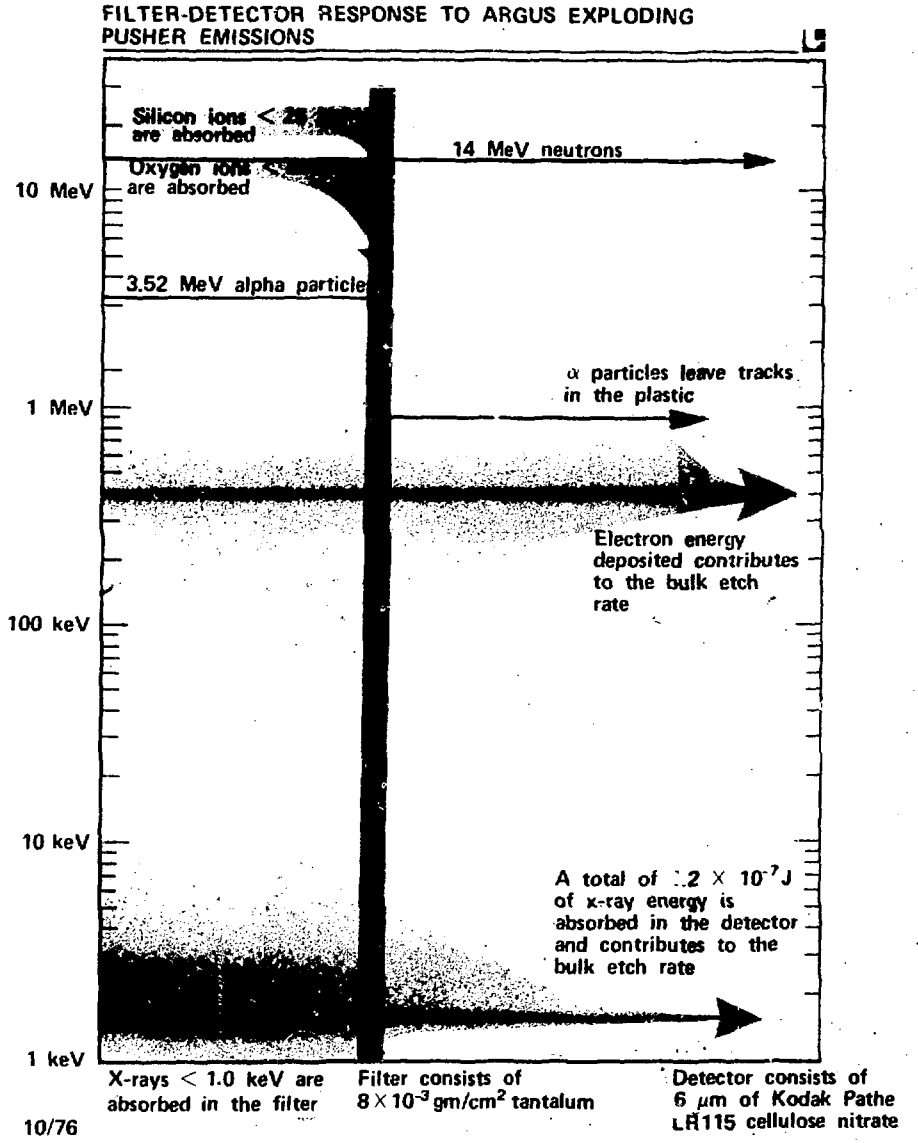
FILTER-DETECTOR RESPONSE TO ARGUS EXPLODING PUSHER EMISSIONS
Silicon ions < 2
are absorbed
14 MeV neutrons
Oxygen ions
are absorbed
10 MeV
3.52 MeV alpha particle
α particles leave tracks in the plastic
1 MeV
Electron energy deposited contributes to the bulk etch rate
100 keV
10 keV
A total of 1.2 × 10⁻⁷ J of x-ray energy is absorbed in the detector and contributes to the bulk etch rate
1 keV
X-rays < 1.0 keV are absorbed in the filter
Filter consists of 8 × 10⁻³ gm/cm² tantalum
Detector consists of 6 μm of Kodak Pathe LR115 cellulose nitrate
10/76

Figure 70

CODED IMAGE OF α EMISSION FROM COMPRESSED D-T MICROBALLOON

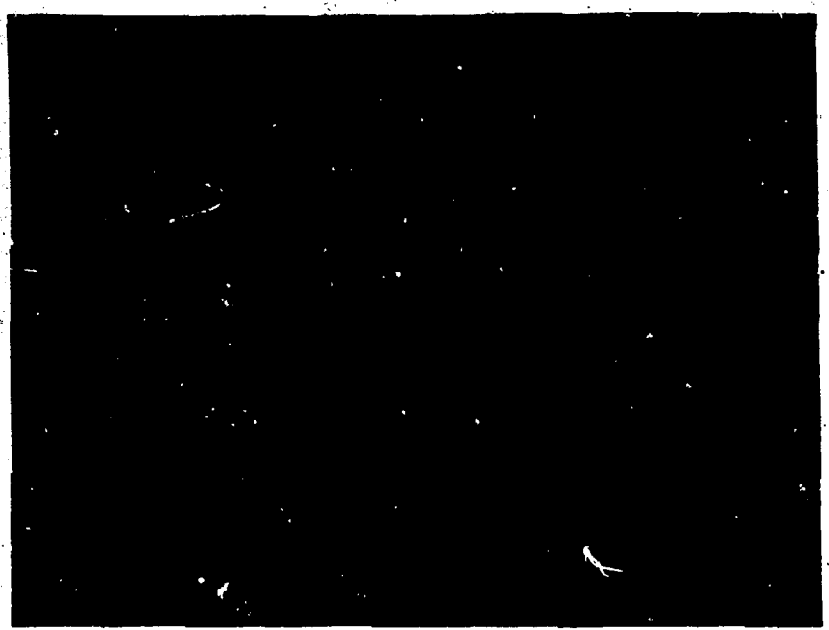

11/76

Figure 71

Figure 72

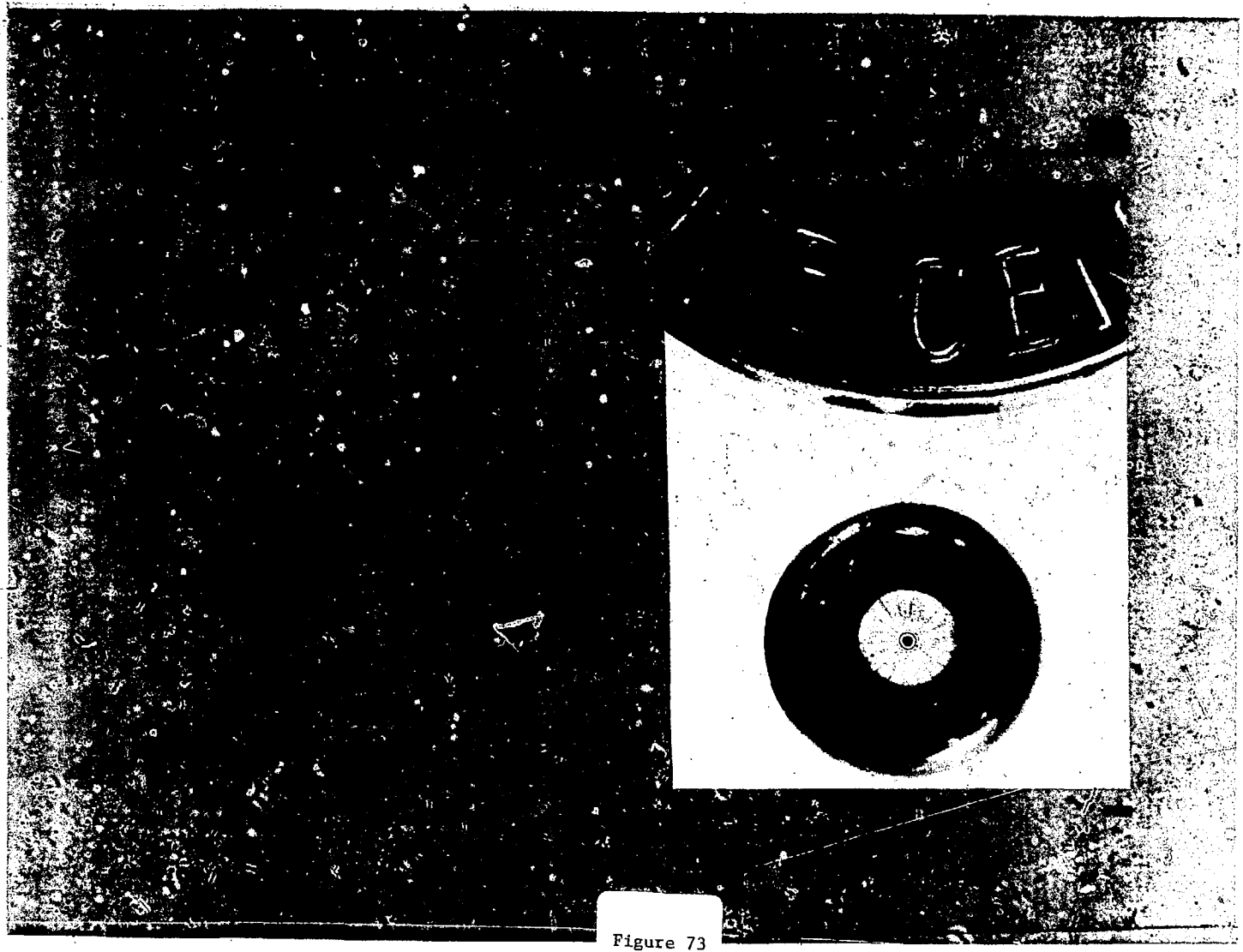

Figure 73

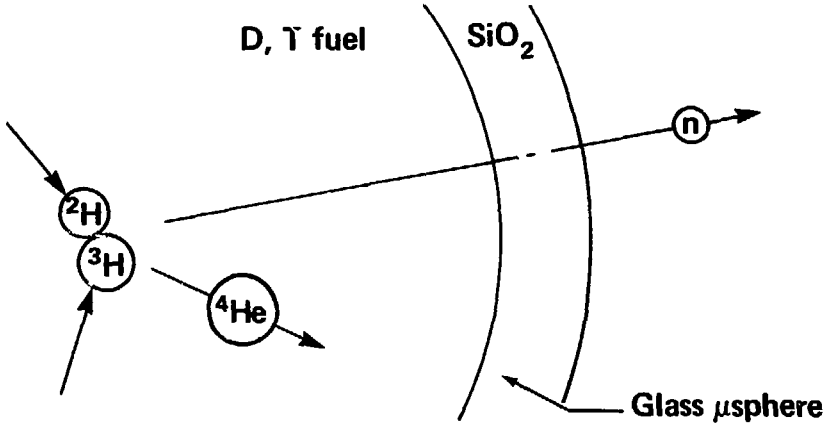

- (^2H, ^3H) neutrons pass through glass microsphere wall
- 14.1 MeV neutrons interact with ^{28}Si atoms in microsphere (24.8% atomic composition) and produce radioactive isotope, ^{28}Al by the reaction

$$^{28}Si(n,p)^{28}Al$$

- $^{28}Al \rightarrow \beta^- + {}^{28}Si^* \rightarrow {}^{28}Si + \gamma$
  - $t_{1/2} = 2.24$ min
  - $h\nu(\gamma) = 1.78$ MeV
  - E_{max} $(\beta^-) = 2.86$ MeV

20-90-0877-1524

Figure 74

RADIO CHEMISTRY

Total number of ^{28}Al atoms produced, N*, can supply information on target compression

$$N^* \simeq 2.1 \times 10^{-3} (N_{yield})(\rho R)_{pusher}$$

20-90-0877-1523

Figure 75

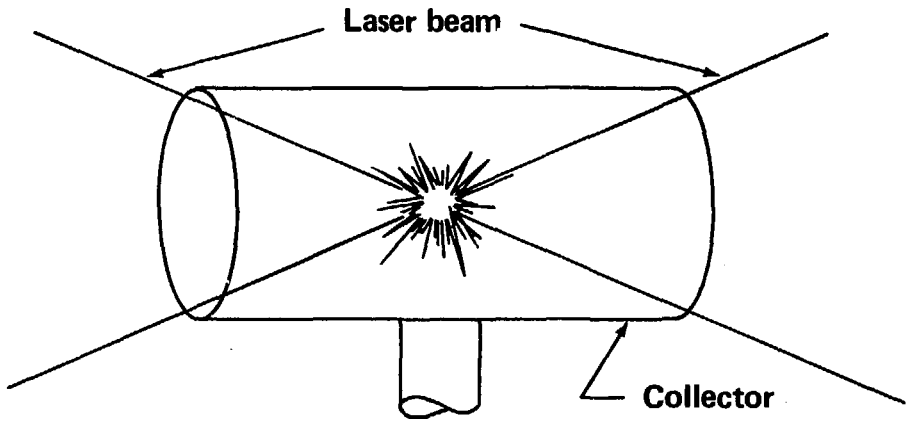

Experimental procedure

- Target debris deposited on plastic liner in cylindrical tube
- Collector removed and placed in nuclear detector and ^{28}Al decays are counted

Counting technique

- β^-, γ coincidence technique employed using a large NaI well detector and plastic fluor
- Measured counting efficiency will allow ~75–100 ^{28}Al atoms to be observed

20-90-0877-1525

Figure 76

SUMMARY OF LASER FUSION RESULTS

Fusion Parameter	Instrument	Accuracy Resolution	Measured	Lasnex
Neutron yield	Cu activation Scint. PMT	15% 20%	$1–2 \times 10^9$	2×10^9
Alpha energy	Alpha TOF	1%	3.3 MeV	3.3 MeV
Ion temperature	Alpha TOF Neutron TOF	20%	6–10 keV	8 keV
Implosion velocity	Streaked x-ray Pinhole camera	6 μm 15 ps	3×10^7 cm/sec	3×10^7 cm/sec
Density	X-ray microscope X-ray spectrometer	4 μm 1 eV	0.1 g/cm^3 0.5–1 g/cm^3	0.1–0.2 g/cm^2 0.5–1.5 g/cm^3
Absorbed energy	Calorimeter	10%	Up to 50%	Up to 50%

5/77

Table IV